HIGOR LUIS SILVA

STRUCTURAL AND AEROELASTIC DESIGN AND OPTIMIZATION OF TRUSS-BASED MODULAR WING STRUCTURES

UNIVERSIDADE FEDERAL DE UBERLÂNDIA
FACULDADE DE ENGENHARIA MECÂNICA
2022

HIGOR LUIS SILVA

STRUCTURAL AND AEROELASTIC DESIGN AND OPTIMIZATION OF TRUSS-BASED MODULAR WING STRUCTURES

Doctoral thesis submitted to the Department of Mechanical Engineering – FEMEC-UFU, in partial fulfillment of the requirements for the doctoral degree of the Doctorate Program in Mechanical Engineering. *FINAL VERSION*

Concentration Area: Solid Mechanics and Vibrations

Advisor: Prof. Dr. Thiago Augusto M. Guimarães

Co-advisor: Prof. Dr. Saullo Giovani Pereira Castro

Uberlândia - MG

2022

Ficha Catalográfica Online do Sistema de Bibliotecas da UFU
com dados informados pelo(a) próprio(a) autor(a).

S586 Silva, Higor Luís, 1993-
2022 Structural and Aeroelastic Design and Optimization of Truss-based Modular Wing Structures [recurso eletrônico] / Higor Luís Silva. - 2022.

Orientador: Thiago Augusto Machado Guimarães.
Coorientador: Saullo Giovani Pereira Castro.
Tese (Doutorado) - Universidade Federal de Uberlândia, Pós-graduação em Engenharia Mecânica.
Modo de acesso: Internet.
Disponível em: http://doi.org/10.14393/ufu.te.2022.345
Inclui bibliografia.

1. Engenharia mecânica. I. Guimarães, Thiago Augusto Machado,1985-, (Orient.). II. Castro, Saullo Giovani Pereira,1983-, (Coorient.). III. Universidade Federal de Uberlândia. Pós-graduação em Engenharia Mecânica. IV. Título.

CDU: 621

Bibliotecários responsáveis pela estrutura de acordo com o AACR2:
Gizele Cristine Nunes do Couto - CRB6/2091
Nelson Marcos Ferreira - CRB6/3074

UNIVERSIDADE FEDERAL DE UBERLÂNDIA
Coordenação do Programa de Pós-Graduação em Engenharia Mecânica
Av. João Naves de Ávila, nº 2121, Bloco 1M, Sala 212 - Bairro Santa Mônica, Uberlândia-MG, CEP 38400-902
Telefone: (34) 3239-4282 - www.posgrad.mecanica.ufu.br - secposmec@mecanica.ufu.br

ATA DE DEFESA - PÓS-GRADUAÇÃO

Programa de Pós-Graduação em:	Engenharia Mecânica				
Defesa de:	Tese de Doutorado Acadêmico, nº 327, COPEM				
Data:	15/07/2022	Hora de início:	08:10	Hora de encerramento:	11:32
Matrícula do Discente:	11913EMC020				
Nome do Discente:	Higor Luís Silva				
Título do Trabalho:	Structural and Aeroelastic Design and Optimization of Truss-based Modular Wing Structures				
Área de concentração:	Mecânica dos Sólidos e Vibrações				
Linha de pesquisa:	Dinâmica de Sistemas Mecânicos				
Projeto de Pesquisa de vinculação:					

Reuniu-se na via webconferência a Banca Examinadora, designada pelo Colegiado do Programa de Pós-graduação em Engenharia Mecânica, assim composta: Professores Doutores: Saullo Giovani Pereira Castro (coorientador) - Delft University of Technology ; Aldemir Aparecido Cavalini Júnior - FEMEC/UFU; Francisco José de Souza - FEMEC/UFU; Leonardo Sanches - ISAE/SUPAERO; Daniel de Almeida Pereira - IPT; Marcos Heinzelmann Junqueira Pedras - EMBRAER; e Thiago Augusto Machado Machado Guimarães - FEMEC/UFU, orientador do candidato.

Iniciando os trabalhos, o presidente da mesa, Dr. Thiago Augusto Machado Machado Guimarães, apresentou a Comissão Examinadora e o candidato, agradeceu a presença do público, e concedeu à Discente a palavra para a exposição do seu trabalho. A duração da apresentação do Discente e o tempo de arguição e resposta foram conforme as normas do Programa.

A seguir o senhor(a) presidente concedeu a palavra, pela ordem sucessivamente, aos(às) examinadores(as), que passaram a arguir o(a) candidato(a). Ultimada a arguição, que se desenvolveu dentro dos termos regimentais, a Banca, em sessão secreta, atribuiu o resultado final, considerando o(a) candidato(a):

Aprovado.

Esta defesa faz parte dos requisitos necessários à obtenção do título de Doutor.

O competente diploma será expedido após cumprimento dos demais requisitos, conforme as normas do Programa, a legislação pertinente e a regulamentação interna da UFU.

Nada mais havendo a tratar foram encerrados os trabalhos. Foi lavrada a presente ata que após lida e achada conforme foi assinada pela Banca Examinadora.

Documento assinado eletronicamente por **Thiago Augusto Machado Guimarães**, **Professor(a) do Magistério Superior**, em 15/07/2022, às 11:37, conforme horário oficial de Brasília, com fundamento no art. 6º, § 1º, do Decreto nº 8.539, de 8 de outubro de 2015.

Documento assinado eletronicamente por **Aldemir Aparecido Cavalini Junior**, **Professor(a) do Magistério Superior**, em 15/07/2022, às 11:37, conforme horário oficial de Brasília, com fundamento no art. 6º, § 1º, do Decreto nº 8.539, de 8 de outubro de 2015.

Documento assinado eletronicamente por **Daniel de Almeida Pereira**, **Usuário Externo**, em 15/07/2022, às 11:47,

conforme horário oficial de Brasília, com fundamento no art. 6º, § 1º, do Decreto nº 8.539, de 8 de outubro de 2015.

Documento assinado eletronicamente por **Francisco José de Souza**, **Professor(a) do Magistério Superior**, em 15/07/2022, às 11:47, conforme horário oficial de Brasília, com fundamento no art. 6º, § 1º, do Decreto nº 8.539, de 8 de outubro de 2015.

Documento assinado eletronicamente por **Leonardo Sanches**, **Usuário Externo**, em 15/07/2022, às 11:47, conforme horário oficial de Brasília, com fundamento no art. 6º, § 1º, do Decreto nº 8.539, de 8 de outubro de 2015.

Documento assinado eletronicamente por **Marcos Heinzelmann Junqueira Pedras**, **Usuário Externo**, em 15/07/2022, às 11:49, conforme horário oficial de Brasília, com fundamento no art. 6º, § 1º, do Decreto nº 8.539, de 8 de outubro de 2015.

Documento assinado eletronicamente por **Saullo Giovani Pereira Castro**, **Usuário Externo**, em 15/07/2022, às 11:49, conforme horário oficial de Brasília, com fundamento no art. 6º, § 1º, do Decreto nº 8.539, de 8 de outubro de 2015.

A autenticidade deste documento pode ser conferida no site https://www.sei.ufu.br/sei/controlador_externo.php?acao=documento_conferir&id_orgao_acesso_externo=0, informando o código verificador **3739812** e o código CRC **63B484C4**.

Referência: Processo nº 23117.047900/2022-22 SEI nº 3739812

HIGOR LUIS SILVA

PROJETO E OTIMIZAÇÃO ESTRUTURAL E AEROELÁSTICA DE ASAS TRELIÇADAS FORMADAS POR ESTRUTURAS MODULARES

Tese apresentada à Faculdade de Engenharia Mecânica – FEMEC-UFU, como parte dos requisitos para obtenção do título de Doutor em Engenharia Mecânica. *VERSÃO REVISADA*

Área de Concentração: Mecânica dos Sólidos e Vibrações

Orientador: Prof. Dr. Thiago Augusto M. Guimarães

Coorientador: Prof. Dr. Saullo Giovani Pereira Castro

Uberlândia - MG

2022

To my family for their unconditional love and support.

ACKNOWLEDGEMENTS

I would like to firstly thank my mom and dad, Dalmi and Gaspar, for being my first school, teaching me the essential values in life: humbleness and unconditional love. They always believed and inspired my goals, being directly responsible for everything I achieved and still intend to do. Especially to my brothers, Denes and Rubens, and my sisters-in-law, Lívia and Larissa, for the encouragement, examples, advices, and for being the backbone that kept me up and ready to face the challenges. To Benício, my godson, for your smile and true love. To all my family and friends, who have consistently been by my side all the way through, making the path smoother.

I would like to strongly thank the full support and advices given by Prof. Dr. Thiago A. M. Guimarães, my great advisor and personal friend. I am so grateful for our entire journey together. Even doing this work from different countries, you were by my side in all the difficulties and anxieties. Without your motivation and encouragement, I would not have carried out this work with confidence and I would not have gotten that far. You have been a great source of inspiration and knowledge to me, putting my happiness in first place and teaching how to think out of the box. Thank you, Thiago, for always believing in my potential and for our long time friendship.

I sincerely want to express my gratitude to Prof. Dr. Saullo G. P. Castro from TU Delft. Thank you for having me as your PhD mentee. Even in the difficulties of the pandemic and thousands of kilometers away, you were essential in the development of this work. Your dedication, character and brilliant mind have not only inspired me, but guided my career. Thank you, Saullo, for always questioning me, for guiding our research and for all your contributions to the academia.

I would like to acknowledge the Federal University of Uberlândia, where I have spent so many years of my life, the Faculty of Mechanical Engineering and all the professor who guided me from my bachelor's to this PhD. Also, I would like to thank the Graduate Program in Mechanical Engineering for the coordination of the course and the National Council for Scientific and Technological Development (CNPq) for the financial support.

I would also like to acknowledge the examination board for their patience reading this work and for their feedback, which strongly improved this work.

Thank you, God, for blessing me everyday and for comforting me throughout this journey.

“The higher we soar,
the smaller we appear to those who cannot fly.”
— Theodore von Karman

RESUMO

SILVA, H. L. **Projeto e otimização estrutural e aeroelástica de asas treliçadas formadas por estruturas modulares**. 2022. 179 p. Tese (Doutorado em Engenharia Mecânica) – Faculdade de Engenharia Mecânica, Universidade Federal de Uberlândia, Uberlândia – MG, 2022.

Este trabalho estuda uma nova abordagem de projeto e otimização estrutural e aeroelástica de asas utilizando estruturas modulares do tipo treliça. Em virtude das metas de redução de emissão de poluentes e da alta demanda por aeronaves cada mais mais leves e eficientes, este tema de pesquisa tem se tornado muito relevante atualmente, se tornando uma contribuição relevante nas novas abordagens de projeto aeronáutico. Neste contexto, a ideia de utilização de estruturas modulares vem com a promessa de fabricação eficiente e custos de manutenção reduzidos. Assim, o trabalho propõe uma nova abordagem de topologia estrutural, eliminando os elementos tradicionais, como longarinas e nervuras, e substituindo por estruturas modulares do tipo treliça, que são conectadas por juntas esféricas em suas extremidades. A malha topológica das estruturas são criadas a partir da triangulação e tesselagem de Delaunay. O modelo estrutural é baseado em dois tipos de elementos finitos: elementos de viga e quadriláteros. Os elementos de viga são definidos a partir dos elementos consistentes de Timoshenko e os quadriláteros são baseados na cinemática Mindlin-Reissner usando interpolação bilinear e integração reduzida para evitar shear locking. O Método Doublet-Lattice é usado para calcular a aerodinâmica subsônica não estacionária, e o método P-K é usado para calcular a solução do sistema aeroelástico. Para exemplos e estudos de caso, é utilizada a geometria da asa do FLEXOP como referência para as dimensões. São propostas três otimizações, onde em todas as funções objetivos são minimizar o peso estrutural da asa e maximizar a velocidade de flutter. A primeira otimização tem como variáveis de projeto o número de pontos de controles, ou nós, em cada aerofólio e o número de seções ao longo da envergadura. Na segunda otimização, são otimizados individualmente os diâmetros externos e espessuras de cada uma das estruturas modulares, podendo, inclusive, eliminar aquelas desnessárias. Os resultados mostram que é possível obter asas relativamente leves e que atendam aos requisitos estruturais e aeroelásticos; todavia, a definição dos parâmetros de otimização influenciam diretamente na geração da malha e custo computacional da otimização. Sobretudo, as estruturas modulares têm se mostrado uma boa estratégia no projeto estruturas de novos conceitos de asa.

Palavras-chave: Projeto de asa, Estruturas modulares, Triangulação de Delaunay, Método doublet lattice, Otimização.

ABSTRACT

SILVA, H. L. **Structural and Aeroelastic Design and Optimization of Truss-based Modular Wing Structures**. 2022. 179 p. Tese (Doutorado em Engenharia Mecânica) – Faculdade de Engenharia Mecânica, Universidade Federal de Uberlândia, Uberlândia – MG, 2022.

This work studies a new design approach and structural and aeroelastic optimization of wings using truss-based modular structures. Due to pollutant emission reduction targets and the high demand for increasingly lighter and more efficient aircraft, this research topic has become very relevant today, becoming a relevant contribution to new approaches to aeronautical design. In this context, the idea of using modular structures comes with the promise of efficient manufacturing and reduced maintenance costs. Thus, the work proposes a new approach to structural topology, eliminating traditional elements, such as spars and ribs, and replacing them with modular truss-based structures, which are connected by spherical joints at their ends. The topological mesh of the structures are created from the Delaunay triangulation and tessellation. The structural model is based on two types of finite elements: beam and quadrilateral elements. The beam elements are defined from consistent Timoshenko elements and the quadrilaterals are based on Mindlin-Reissner kinematics using bi-linear interpolation and reduced integration to prevent shear locking. The Doublet-Lattice Method is used to predict the unsteady subsonic aerodynamics, and the P-K method is used to compute the aeroelastic system solution. For the examples and case studies, a reference wing geometry from the FLEXOP project is used as a baseline. Two optimizations are proposed, where in all the objective functions are to minimize the structural weight of the wing and to maximize the flutter speed. The first optimization has as design variables the number of control points, or nodes, in each airfoil and the number of sections along the span. In the second optimization, the external diameters and thicknesses of each of the modular structures are individually optimized, even eliminating unnecessary ones. The results show that it is possible to obtain relatively light wings that meet the structural and aeroelastic requirements; however, the definition of the optimization parameters directly influence the mesh generation and computational cost of the optimization. Above all, modular structures have proved to be a good strategy in the design of structures for new wing concepts.

Keywords: Wing design, Modular structures, Delaunay Triangulation, Doublet lattice method, Optimization.

LIST OF FIGURES

LIST OF TABLES

LIST OF ABBREVIATIONS AND ACRONYMS

AIC	Aerodynamic Influence Coefficients
AM	Additive Manufacturing
CD	Crowding Distance
CFD	Computational Fluid Dynamics
CRM	Common Research Model
DLM	Doublet-Lattice Method
DOF	Degree of Freedom
EBM	Electron Beam Freeform Fabrication
FEM	Finite Element Method
FGM	Functionally Graded Materials
FLEXOP	Flutter Free FLight Envelope eXpansion for ecOnomical Performance improvement
FSDT	First-order Shear Deformation Theory
GAM	Generalized Aerodynamic Matrix
LSM	Level Set Method
MDO	Multidisciplinary Design Optimization
NACA	National Advisory Committee for Aeronautics
NASA	National Aeronautics and Space Administration
NSGA-II	Non-dominated Sorting Genetic Algorithm II
PDE	Partial Differential Equation
SBX	Simulated Binary Crossover
VLM	Vortex-Lattice Method

LIST OF SYMBOLS

$\mathcal{AR}$ — aspect ratio

A_Ψ — amplitude of sinusoidal harmonic solution

a — speed of sound

C_L — lift coefficient

c_p — pressure coefficient

D_i — diameter of each truss element

D_{rs} — downwash factor

E — Young modulus

G — transformation matrix

g — damping

h_m — mean surface

h_t — envelope of thickness

I — moment of inertia

J — Jacobian

K — Kernel function

k — reduced frequency

L — Lift

L_{ref} — reference length

M_∞ — Mach number

m — mass

p — pressure

Q_{hh} — generalized aerodynamic matrix

q_∞ — dynamic pressure

S — wing surface, wing area

T — temperature

t — time, thickness

u — velocity in x-direction

V — velocity

v — velocity in y-direction

w — velocity in z-direction

β — Prandtl-Glauert

Γ_s — angle between the surface and the xy-plane at the sending points s

Γ_r — angle between the surface and the xy-plane at the receiving points r

γ — ratio of specific heats, shear strain

ε — strain

ζ — local coordinate

η — local coordinate

θ — angle of the element at the joint

ξ — local coordinate

ρ — air density

σ — normal stress

τ — shear stress

Φ — velocity potential, modal matrix

ϕ — velocity potential

Ψ — acceleration potential

ψ — approximation function

Ω — domain of triangulation

ω — oscillation frequency

CONTENTS

CHAPTER

1

INTRODUCTION

"Scientists study the world as it is; engineers create the word that has never been."
— Theodore von Karman

In the last years, the aerospace industry has faced many challenges in the development of new projects and technological innovations (WHEELER; BOZHKO, 2014). With a global debate increasingly focused on environmental impacts and other climate changes, aviation as a whole could not be absent from the discussions, since it is one of the biggest contributors to the emission of greenhouse gases (BECKEN; MACKEY, 2017). In this context, engineers and researchers have been dedicating efforts to develop increasingly efficient aircraft, i.e., aircraft that are increasingly lighter and that consume less fossil fuels (NAAYAGI, 2013; BOWMAN *et al.*, 2007; VELICKI; JEGLEY, 2011; KANG; YE; GO, 2016); however, to achieve very aggressive goals (BONET *et al.*, 2011; ACARE, Advisory Council for Aviation Research Innovation in Europe, 2012), it is necessary to move forward and create new disruptive technologies (GRÖNSTEDT *et al.*, 2016; GHADGE *et al.*, 2018; MOORE, 2010).

Regarding fossil fuel consumption, in recent years many conceptual projects and experimental models have been presented to the market (BRELJE; MARTINS, 2019; LAPEÑA-REY *et al.*, 2010; NANDA, 2011; JUVE *et al.*, 2016; SIEMENS, 2016; BORER *et al.*, 2016; BARTELS *et al.*, 2015). Hybrid-electric and fully-electric aircraft designs seek to combine innovative propulsion systems, including electric motors and batteries, in order to reduce energy consumption during a certain mission, which can make somehow some operations more profitable, such

as the thin-haul operations (SILVA; GUIMARÃES, 2020). However, most operations are not yet benefited, since long-range missions require a lot of stored energy, which would imply tons of batteries (SILVA *et al.*, 2021). Thus, the technological advancement of specific energy of batteries is still crucial (TARIQ *et al.*, 2016). In this context, other alternatives have been recently presented, such as the new Airbus hydrogen-powered airplanes (AIRBUS. . . , 2020). These new concepts rely on hydrogen as a primary source, granting zero chemical emissions in all phases of flight (TRAINELLI *et al.*, 2019), which enables advances towards decarbonization of the entire aviation industry, likely being a solution for aerospace and many other industries to meet their climate-neutral targets.

On the other hand, when it comes to more efficient aircraft, the idea of better aerodynamic efficiencies and lighter structures easily comes to mind. For better aerodynamic efficiency of next-generation aircraft concepts, many studies propose wings with higher aspect ratios and different design shapes, examples being the D8.x jet transport configuration (DRELA, 2011) or the Truss-Braced Wing concept (BRADLEY; DRONEY, 2011). Moreover, Martins, Kennedy and Kenway (2014) evaluate the impact of new structural material technologies on the aerostructural trade-offs in the design of conventional and high aspect ratio wing design. Zhang, Li and Kou (2005) design and compare sandwich multi-spar structures and innovative mixed structure basing on the structural characteristics of high aspect ratio wings. Furthermore, Afonso *et al.* (2017) present a review on the state-of-the-art on nonlinear aeroelasticity of high aspect-ratio wing. At the same time, when designing aircraft wings with bigger spans and with lighter structures, these wings tend to become less stiff and consequently more prone to aeroelastic instabilities such as flutter, which can render much of the operation envelope unfeasible. In this sense, aeroelastic constraints become important issues to take care of and account for during the design process, mainly in early design stages (ÖSTERHELD; HEINZE; HORST, 2000), preventing costly design changes in later design phases or worse during flight testing.

Some works have been studying new models of structure for the wing, presenting novel manufacturing techniques and enabling unconventional internal wing layouts. Saleem, Yuqing and Yunqiao (2008) apply nonparametric topology optimization and manufacturing simulation on a commercial aircraft vertical stabilizer component. Sleesongsom, Bureerat and Tai (2013)

propose a novel design approach for synthesizing the internal structural layout of a morphing wing. Nevertheless, when the topic is manufacturing, assembling, and optimization with design constraints, it is important to ensure that the structures can be easily handled and used for large scale. Thus, a good strategy is to divide the structure into a set of similar parts so that the process becomes less costly and easier to be reused, which in turn represents the concept of modularity. Therefore, modular structures have also been studied in aerospace applications because they present benefits analogous to truss topology. Following that, Montemurro, Vincenti and Vannucci (2012) present a two-level procedure for the global optimum design of composite modular structures, applying to the design of an aircraft wing. Moses, Fuchs and Ryvkin (2002) suggest a numerical method for the topological design of modular structures under general and arbitrary loading.

1.1 Research Objective and Approach

The need to develop lighter aircraft with easy-to-manufacture structures has become a focus in aircraft design recently. Thus, this work deals with structural wing design studies and optimizations using modular structures, especially applying truss-based concept. Along those lines, the main objectives of this work include:

(i) To make a literature review of the most recent works performed on structural wing design and modular structures including topology optimization;

(ii) To present an aerodynamic and structural modeling, along with aeroelastic coupling, which are able to evaluate the dynamic behaviour of the truss-based wing;

(iii) To propose an optimized spatial structural arrangement, i.e., a topology optimization for the truss-based wing that accounts for structural and aeroelastic constraints;

(iv) To present an aeroelastic modeling, i.e., to couple the aerodynamic and structural tools developed in order to obtain the aeroelastic response of any wing model, and, consequently, the flutter solution;

(v) To discuss how the design parameters affect the trade-off between the weight of the wing structure and the flutter velocities. Overall, to discuss how the modular structures impacts the wing design.

In summary, the main contributions of this work are the use of modular structures in aircraft wings, which is not found in the literature. In addition, to make a study of topological optimization of the structural mesh considering structural and aeroelastic constraints.

1.2 Document Structure

This document is structured as follows:

- Chapter 2: a literature review is carried out on the use of modular structures in engineering, especially in aerospace applications. In addition, the main studies and contributions presented in the literature on the subject are listed;

- Chapter 3: the aerodynamic modeling and its formulation are presented, which is based on the Doublet-Lattice Method (DLM) for unsteady flow. A verification is presented at the end of the chapter in order to verify the accuracy of the code implementation compared to literature references;

- Chapter 4: the structural modeling is presented basing on two types of finite elements: beam and quadrilateral elements. The beam elements are defined from consistent Timoshenk elements and the quadrilaterals are based on Mindlin-Reissner kinematics using bi-linear interpolation and reduced integration to prevent shear locking. A verification is presented at the end of the chapter in order to verify the accuracy of the code implementation compared to Nastran;

- Chapter 5: the aeroelastic modeling is presented, i.e., how the aerostructural coupling is addressed. Also, the P-K method is used to compute the aeroelastic system solution. At the end of the chapter, a verification is presented in order to ensure the agreement of the results when compared to Nastran;

- Chapter 6: A truss-based wing design accounting for structural and aeroelastic constraints is presented. It is proposed a new approach to structural topology, eliminating traditional elements, such as spars and ribs, and replacing them with modular truss-based structures, which are connected by spherical joints at their ends. The topological mesh of the structures are created from the Delaunay triangulation and tessellation. For the examples and case studies, a reference wing geometry from the FLEXOP project is used as a baseline. Two optimizations are proposed, where in all the objective functions are to minimize the structural weight of the wing and to maximize the flutter speed. The first optimization has as design variables the number of control points, or nodes, in each airfoil and the number of sections along the span. In the second optimization, the external diameters and thicknesses of each of the modular structures are individually optimized, even eliminating unnecessary ones;

- Chapter 7: this chapter summarizes the main aspects covered by this work and discuss the main conclusions regarding the methods and approaches presented, and what are the next proposals for future works.

CHAPTER

2

LITERATURE SURVEY AND THEORY

"To most people, the sky is the limit. To those who love aviation, the sky is home."

— Jerry Crawford

THIS chapter presents some concepts and a literature survey and theory about the research that contributed to the development of this doctoral thesis. The first section addresses the structural wing design and how the wing airfoil and wing planform affects the structural design. Next, some alternatives in terms of structural weight reduction are presented, along with some concepts that improve flutter speed. Last but not least, it is presented the concepts and studies related to topology optimization for structural wing design.

2.1 Structural Wing Design

Flying has always been one of humanity's greatest desires and, since the beginning of the last century, several aircraft models and prototypes have been developed throughout history. In the beginning, in the days of the Wright Brothers and Santos Dumont, the role of the aircraft was simply to be able to stay in the air; then, during World War II, the role was already to produce faster and more maneuverable aircraft that performed better in aerial combat. In the post-war scenario, including the cold war, aviation as a mode of transport had an exponential growth, after all, globalization brought the need for people to move to different countries in the world (SVIK, 2020). At that time, the role of the aircraft was to transport more people at the lowest possible cost, which is directly related to lower fuel consumption. Therefore, in recent decades

the need to develop aircraft that consume less fuel has been the focus of engineers (GAO *et al.*, 2022); furthermore, in recent years, a special reason has driven the development of more efficient aircraft: the climate change (RYLEY; BAUMEISTER; COULTER, 2020).

Climate change, which has been debated for many years, is now a reality, that is, the planet is already showing symptoms of the effects of unsustainable human exploitation. Aviation, as one of the main contributors to the emission of greenhouse gases (HASAN *et al.*, 2021), has been working in recent years to be able to design more efficient aircraft, that is, that consume less fossil fuels or even do not use such energy sources, as is the case of fully-electric aircraft (BRELJE; MARTINS, 2019).

In this context, to make such projects viable, it is necessary to establish a very important trade-off between aerodynamics and weight. Aerodynamics need to be optimized in all respects to generate less drag and the structural weight of the entire aircraft needs to decrease in order to carry more payload for the same takeoff weight or in order to reduce the energy required to complete the mission, which directly impacts the sizing of the rest of the aircraft.

Thus, the design of a wing must follow the same reasoning, that is, be efficient and light at the same time. Consequently, when thinking about the design of an aircraft wing, it is necessary to associate it with the aerodynamic and structural aspects, generating a range of possibilities (see Fig. 1).

The aerodynamic aspect is due to the fact that this component is responsible for generating the lift force capable of keeping the aircraft in flight during the mission. The structural aspect is due to the fact that the wing needs to be resistant to forces and concentrated loads from components that are attached to it (control surfaces, hyper-lift devices and engine pylon-nacelle assembly), but mainly from aerodynamic loads of different magnitudes and conditions, such as gust winds, for example. Therefore, it is possible to observe that there is a notorious relationship between aerodynamics and structures in the design of a wing and, if there is a relationship, there are trade-offs.

A didactic way of coming up with the trade-offs present in the design of a wing is to separate its 3-D shape into two parts, where one of them involves the wing's planform (top view

Figure 1 – Wheel of non-planar wing configurations.

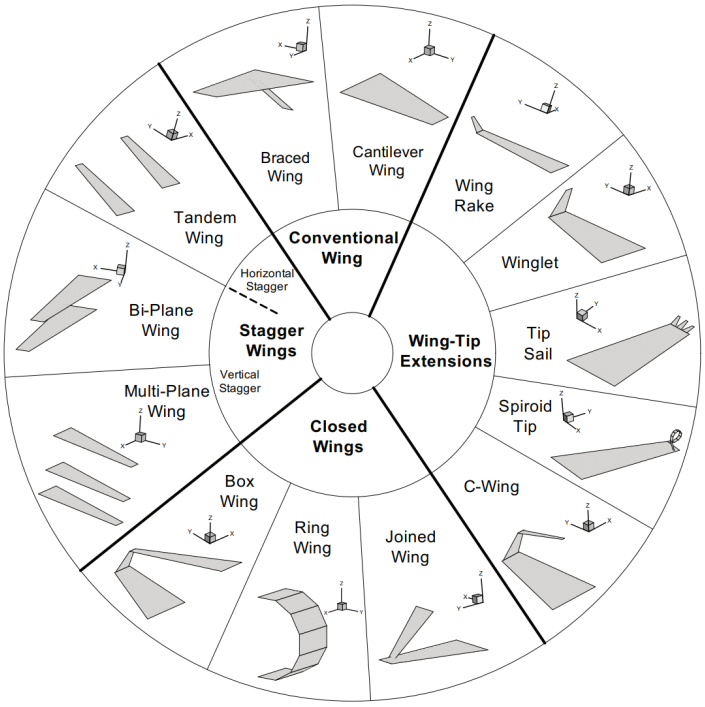

Source: Jansen and Perez (2010).

of a wing, that is, span and chord), as illustrated in Fig. 2a, and the other involving the shape of its thickness, that is, the aerodynamic profile, as depicted in Fig. 2b. Both parts are extremely important in aerodynamic design and each has different implications for the structural design of the wing. However, although these implications are different, they have the same design components in common and impact on the same design parameters.

Figure 2 – Wing 3-D shape into two parts.

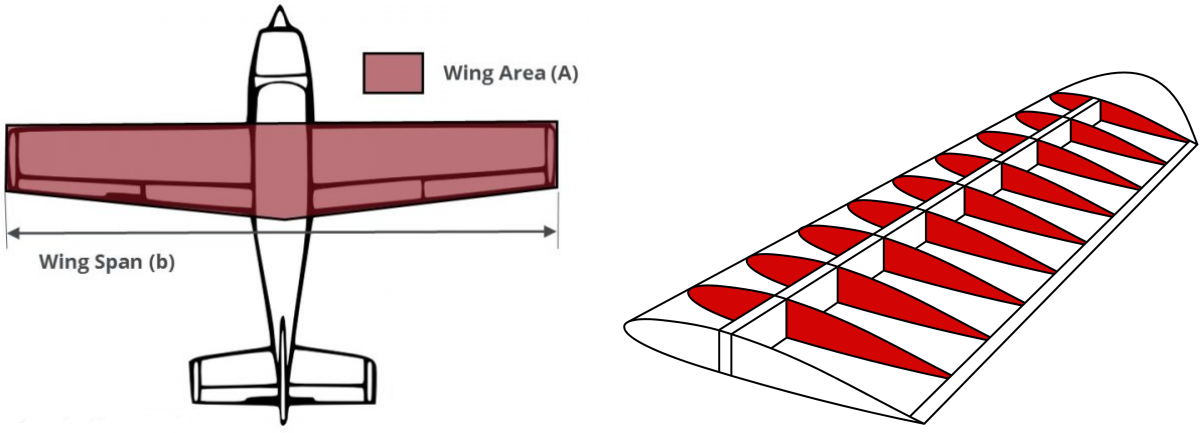

(a) Wing planform. (b) Aerodynamic profile.

Source: Elijah *et al.* (2021).

2.1.1 Impact of the wing airfoil on the structural design

It is easy to see that the main function of the aerodynamic profile in the design of a wing is to contribute to the generation of lift for the aircraft. Therefore, parameters such as lift coefficient, drag and moment are considered essential when choosing a profile. Considering the profile geometry, parameters such as the profile's leading edge radius and curvature are immediately remembered, as they are associated with the mentioned parameters. However, at this stage of the project, it is always very important to remember which proposal the aircraft project is intended to fulfill and which should be the product's main key point, as this reduces the chance of leaving any parameter or consideration goes unnoticed. In many cases, it is common for structural weight reduction to be an important bias in the design of an aircraft and the selection of the appropriate profile contributes greatly to this. This happens through the relative thickness of the airfoil.

An aerodynamic profile (also known as a rib) with greater relative height (thickness divided by the chord) allows a higher spar to be used in the wing design, which implies greater moments of inertia without increasing spar width. In other words, spars with higher cross sections are more resistant to bending moments and have less structural weight. Thus, aerodynamics, through the selection of aerodynamic profiles (or ribs), impacts the structural design, having consequences on the empty-weight of the aircraft.

2.1.2 Impact of the wing planform on the structural design

The definition of the wing's plan shape is extremely important in the aerodynamic design of an aircraft, as it has an important contribution to the product's in-flight performance. The correct dimensioning of design parameters such as aspect ratio, tapering, among others, is crucial for different phases of flight, such as take-off, landing and cruise flights. In addition, they directly affect the structural design of a wing.

Wings generate lift as is well known. Each airfoil (or rib) contributes to a certain amount of lift force and this depends on two factors: its shape and its chord (obviously associated with factors of the environment in which it is interacting such as the speed and viscosity of the air). Therefore, it is possible to notice that changing the shape of the wing in plan by changing the

measurement of some profile also changes the aerodynamic loading of the wing. The change usually made in wing designs is the application of taper, that is, the reduction of the chord size of the profiles starting from the root to the tip of the wing, as can be seen in several aircraft such as the Embraer E-Jets E2, Gulfstream G650 and several other aircraft. The rationale for designing a tapered wing is mainly aerodynamic, as this type of adjustment is intended to reduce the induced drag of the design and consequently improve the performance of the aircraft. Fig. 3 shows different types of wing planforms.

Figure 3 – Different types of wing planforms.

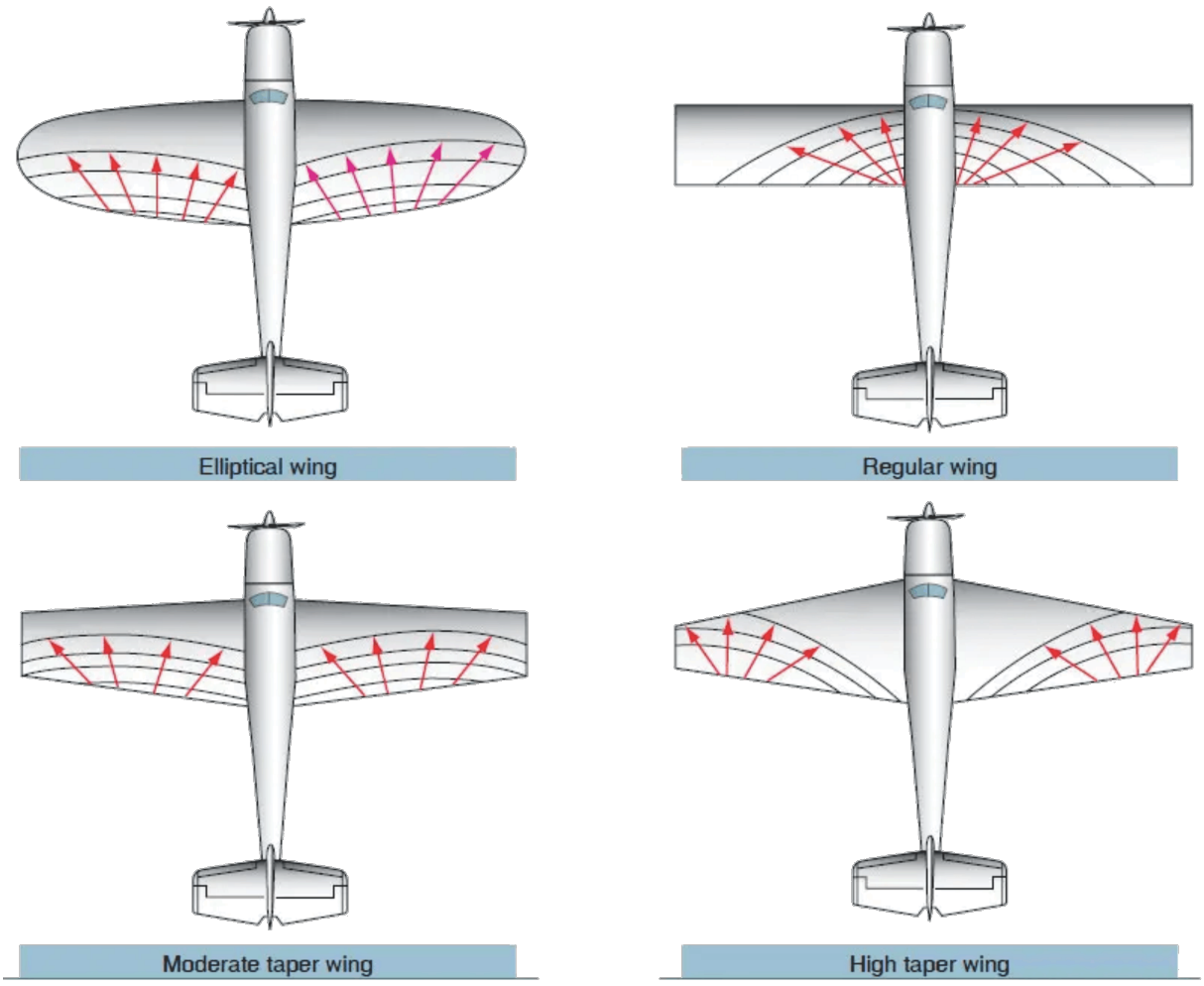

Source: Flight Literacy (2022).

On the other hand, observing the structural aspect, the more tapered the wing (smaller taper values), the greater the aerodynamic loading (lift force) in the wing tip regions. This leads to two problems: the first is that in the event of a stall, the loss of lift will occur first at the wingtip, the region where the ailerons are located, implying a loss of control of these

commands in an emergency situation. The second (this one associated with the structural design), implies an inefficient structural design since high aerodynamic loads in a given region of the wing unnecessarily lead to oversized structures, with high structural weight. Thus, there is the following trade-off: opt for a less accentuated taper and be penalized by the greater induced drag or keep this design solution being penalized by weight. Either of the two options can be used, but not only them. The truth is that there are other parameters that can help in this trade-off, in order to reduce the loss of efficiency, either in the drag or in the structural weight, such as the geometric and aerodynamic twists.

2.1.3 Structural Weight Reduction Alternatives

From Sections 2.1.1 and 2.1.2, a strong relationship between aerodynamic design and structural design can be seen. However, it is often not possible to modify the aerodynamic design to generate a lighter structure, then many studies and concepts have been developed over the years to modify at least the structural aspect.

First, the materials can be pointed out. Since the last century, most aircraft have been made of traditional metallic materials, such as aluminum, titanium, and steel (KENNEDY; MARTINS, 2012). In 2004, Boeing announced the 787 series, which use approximately 50% of composite materials, considerably reducing the structural weight of the aircraft (MRAZOVA, 2013). On the other hand, Airbus introduced the A350 to the market, which also follows the same trend of using composite materials (MARSH, 2007). However, although the modeling of these materials is currently well understood, manufacturing with these materials is still a great challenge, as it requires great quality control and the inclusion of uncertainties in the design of the project (**??**).

Moreover, other unconventional structural approaches have been presented in the literature, such as laminates of variable stiffness. The advent of machines that perform fiber deposition automatically made it possible to manufacture laminates with curved fibers (tow steering) easier, more controlled and more efficient. These laminates can be used in a variety of design applications, as fiber path optimization can, for example, increase the critical buckling load, decrease stress concentrations, change dynamic characteristics and also improve aeroelastic behavior

(GUIMARÃES *et al.*, 2016). Figure 4 shows examples of conventional and tow-steered layups of composite structures.

Figure 4 – Conventional and tow-steered layups.

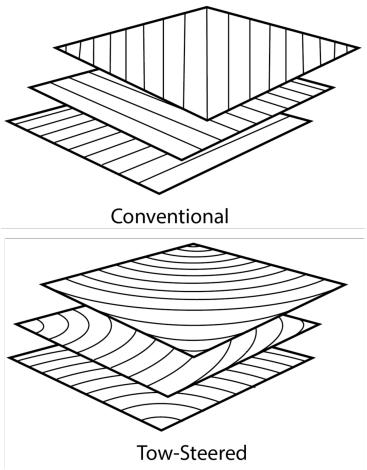

(a) Illustration of layups.

(b) NASA's tow-steered carbon wing.

Source: Brooks and Martins (2018).

In addition to the use of composite materials in the aeroelastic tailoring technique, recent advances in manufacturing methods, such as EBM (electron beam freeform fabrication), and additive manufacturing (AM), have led to the use of disruptive materials, including FGM (functionally graded materials). FGMs are materials that have a continuous variation of mechanical properties, spatially varying the distribution of two or more materials (see Fig. 5). According to Dunning *et al.* (2014), FGMs offer two major advantages in aircraft designs: first, they enable continuous changes in the mechanical properties of the structure (Young's modulus, density, fatigue resistance, etc), enabling local properties to be adjusted; second, they allow changes in structural stiffness without necessarily altering the shape and geometry of the structure, such as increasing thickness.

2.2 Topology Optimization

The internal structures of a conventional wing are generally composed of spars and stringers in the span-wise direction and ribs in the stream-wise direction. This has been traditional over the years because these structures are efficient and strong (i.e., able to withstand the load that are applied to them) and, at the same time, are easy to manufacture by conventional

Figure 5 – Cross sections of two stiffeners made from a 50/50 SS-Cu blend. Left: grading along the stiffener (axis coming out of the page): cut taken mid-length of the stiffener. Right: grading through the depth (axis is vertical).

Source: Dunning *et al.* (2014).

methods. However, the advancement of technology and manufacturing techniques has allowed the reinvention and design of new structures and internal struts in order to obtain lighter wings that have good dynamic and aeroelastic behavior.

Topology optimization has been used as tool for so many years to explore and to improve new wing structural configurations. The idea was first applied by Bendsøe and Kikuchi (1988) by optimizing the topology of a domain based on a material distribution method. A foam-like composite material was used to approximate the local properties for different void sizes using the homogenization method. The method provided optimal shape and topology even though the problem was formulated as an intuitive and simple sizing problem (see Fig. 6).

Figure 6 – Topology optimization for minimum compliance with volume constraint of 36%.

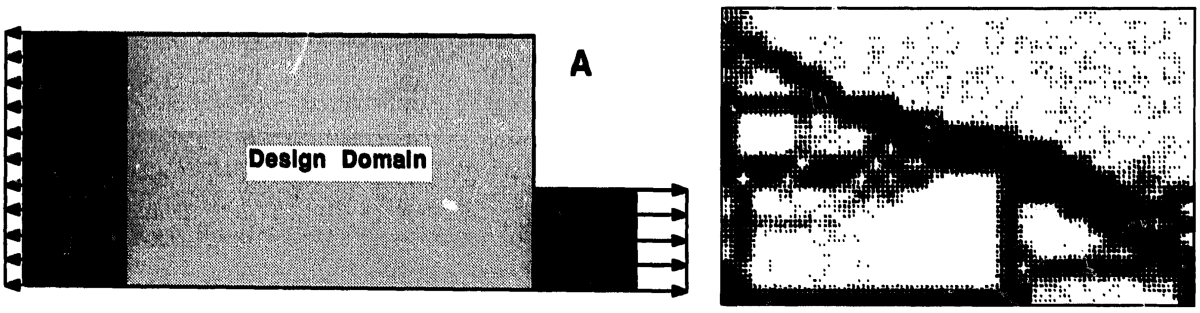

Source: Bendsøe and Kikuchi (1988).

Later on, Balabanov and Haftka (1996) modeled the internal structure of a wing as a truss and the cross-sectional areas of the truss were optimized. Also, the wing's compliance

was reduced under loads equivalent to a symmetric pullup maneuver. By minimizing mean compliance, the bubble method was employed by Eschenauer and Olhoff (2001) to optimize the topology of wing ribs for pullup and tank pressure loads. Krog *et al.* (2004) developed the solid isotropic material penalization (SIMP) method (BENDSØE; SIGMUND, 1999) to optimize the topology of aircraft wing ribs, which involved minimizing a weighted sum of total internal energy due to various load scenarios (see Fig. 7). Wang, Lu and Zhou (2011) optimized leading-edge ribs by minimizing compliance using the subset simulation-based topology optimization method. Choi *et al.* (2011) designed a flapping wing using a dynamic topology optimization method to improve the thrust and propulsive efficiencies of the wing.

Figure 7 – Topology optimization of rib profiles.

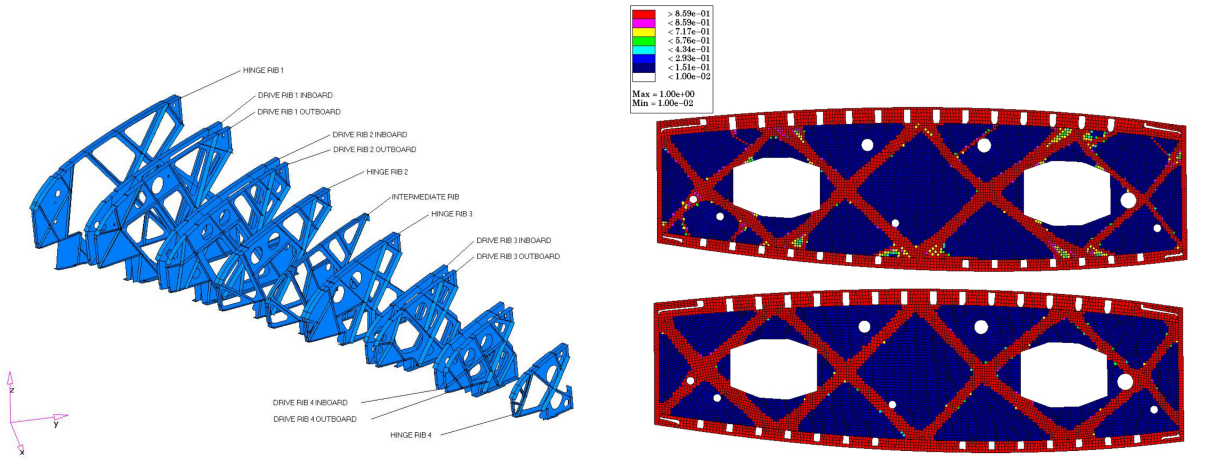

(a) Topology, sizing and shape optimized designs for A380 leading edge ribs.

(b) Topology optimized rib designs, obtained using a local analysis approach.

Source: Krog *et al.* (2004).

The aerostructural coupling (the connection between the aerodynamic and structural evaluations) is critical in determining the best wing topology (MAUTE; ALLEN, 2004). By adding aerostructural coupling, Maute and Allen (2004) used the SIMP approach to optimize the stiffness distribution of a platelike wing. Stanford and Beran (2011) provided a Pareto trade-off research between the aeroelastic instability speed and the wing weight. They discretized the plate into finite elements and the thickness of each element was defined as a design variable. They also concluded that placing a higher premium on light weight results in an array of batten and riblike members, which stiffened the structure. Stanford and Ifju (2009) employed topology optimization to plan the arrangement of a two-material membranelike skeletal structure, maximizing lift-to-

drag while also taking into account aerostructural coupling. Kolonay and Kobayashi (2015) used the cellular division approach to optimize the topology, size, and shape of an aircraft's lifting surfaces. The findings revealed that the best spars and ribs are curvilinear. Locatelli, Mulani and Kapania (2011) presented their research on the topology and sizing optimization of wing-box structures using curvilinear spars and ribs, which revealed that the optimized structure with curvilinear spars and ribs of a supersonic fighter aircraft is 19% lighter than the structure with straight spars and ribs.

The structural configurations of three-dimensional wings, such as NASA the Common Research Model (CRM) wing (VASSBERG *et al.*, 2008), have been addressed for coupled aerostructural interactions. Kenway, Kennedy and Martins (2014) optimized the planform geometry variables as well as the skin and spar panel dimensions. Despite the fact that the results are not topological optimization, they show that the fuel burn can be reduced by up to 8.8%. Stanford and Dunning (2015) performed a topology optimization using the SIMP approach and applied to the ribs and wing box of the NASA CRM. Wing compliance was minimized under trim loads, taxi loads, and crushing loads (see Fig. 8). The work of James, Kennedy and Martins (2014) showed concurrent aerodynamic and structural optimization of the NASA CRM wing box using SIMP, and they reported that the best designs had significant load-carrying intermediate density material, which is not viable. They also concluded that the intermediate density material serves as a secondary structure, transferring load to the primary structure.

Figure 8 – Compliance-optimal topology for aeroelastic trim loads (left), for taxi bump loads (right), and a compromise between the two (center).

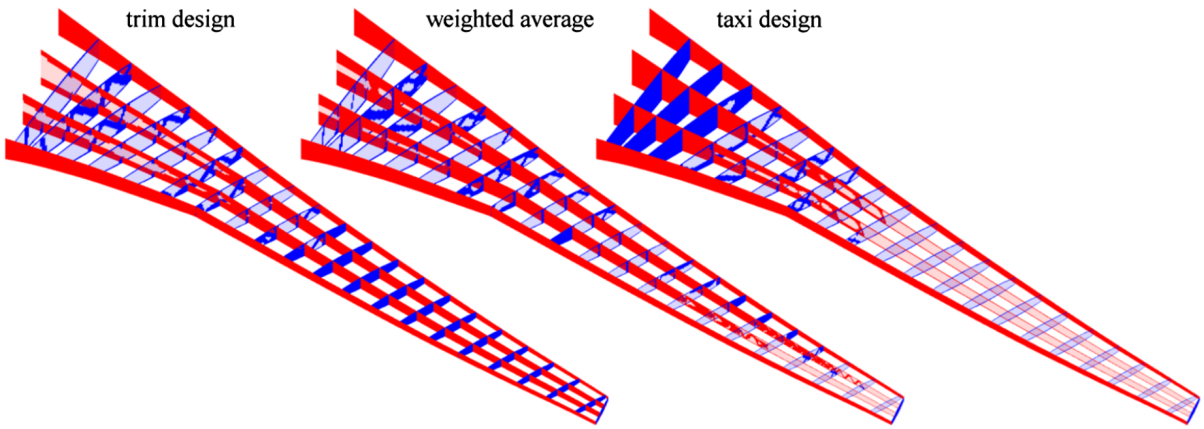

Source: Stanford and Dunning (2015).

The level set method (LSM) is a topology optimization method that does not employ intermediate density material, i.e., the method does not use a grid of the geometry to assess the material property distribution, instead it adopts an implicit description of boundaries to parametrize the geometry. Dunning, Stanford and Kim (2015) used LSM to optimize the internal structure of the NASA CRM wing box. The ideal structure that resulted was hollow and lacked rib–spar combinations. Due of the coarseness of the mesh, the authors employed a fictitious material with 10% of the elastic modulus and density of aluminum to produce appropriate topologies. Dijk *et al.* (2013) writes an overview of different level set methods for structural topology optimization.

Other works have been developed regarding topology optimization over the last decade. Oktay, Akay and Merttopcuoglu (2011) presented a set of structural optimization tools for topology optimization of aircraft wing structures coupled with Computational Fluid Dynamics (CFD) analyses. Dunning, Stanford and Kim (2015) develops a level set topology optimization method for an unstructured three-dimensional mesh and apply it to NASA CRM wing box design for coupled aerostructural considerations. Chedrik and Tuktarov (2015) combine the structural optimization based on the global-local approach with topology optimization to perform a complete design procedure of aircraft structures (see Fig. 9). Rinku and Ananthasuresh (2015) propose a modular design of wing-ribs with fewer components than conventional semi-monocoque design (web reinforced with stiffeners), which is likely to lower the cost of manufacturing and assembly.

Figure 9 – Initial solid FE model (left), topology result (right).

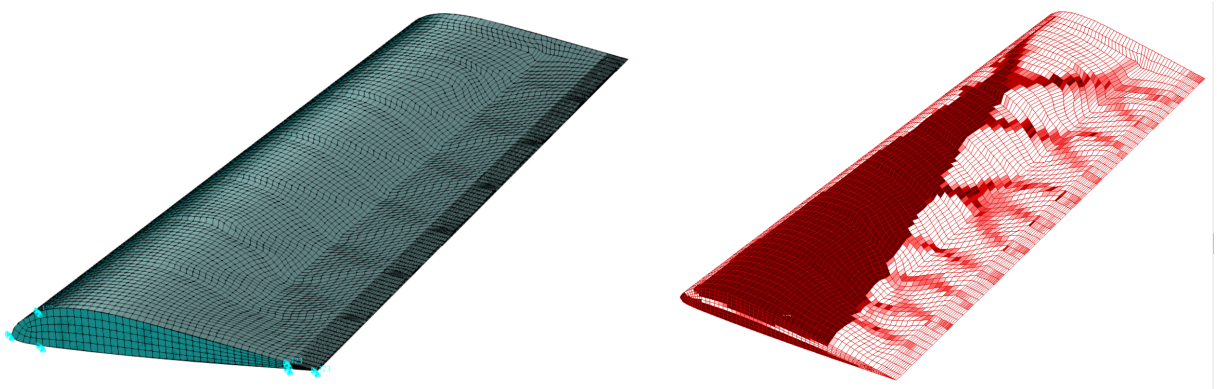

Source: Chedrik and Tuktarov (2015).

More recently, Aage *et al.* (2017) used a high-resolution mesh of the NASA CRM wing box for optimization with the SIMP method. The large-scale study addressed in this work used a 1.1-billion-element mesh, and the optimized design presented interesting similarity to naturally occurring bone structures such as bird beaks. However, the loads applied were not realistic because the aerostructural coupling was ignored. Large-scale topology optimization studies that take into account aerostructural coupling are much more challenging, since the complex nature of the problem and the loads depend on the design. Also, for these cases, the computational cost of simulating is much higher, but taking into accounts the aerostructural coupling properties yield more efficient designs. Later on, Kambampati, Townsend and Kim (2020) present a coupled aerostructural topology optimization study for a three-dimensional (3-D) aircraft wing box considering aerostructural coupling. A new level set method is developed, where two separate meshes are used: 1) a level set grid for design, and 2) a finite element (FE) mesh for analysis. Opgenoord and Willcox (2019) develop a methodology to design aeroelastically tailored wings using additively manufactured lattice structures (see Fig. 10). Adaptive meshing techniques are used to design the topology of the lattice to align with the load direction, and the lattice is optimized to minimize the structural weight and to improve the flutter margin.

Figure 10 – Original lattice that is optimized without considering aeroelastic instabilities.

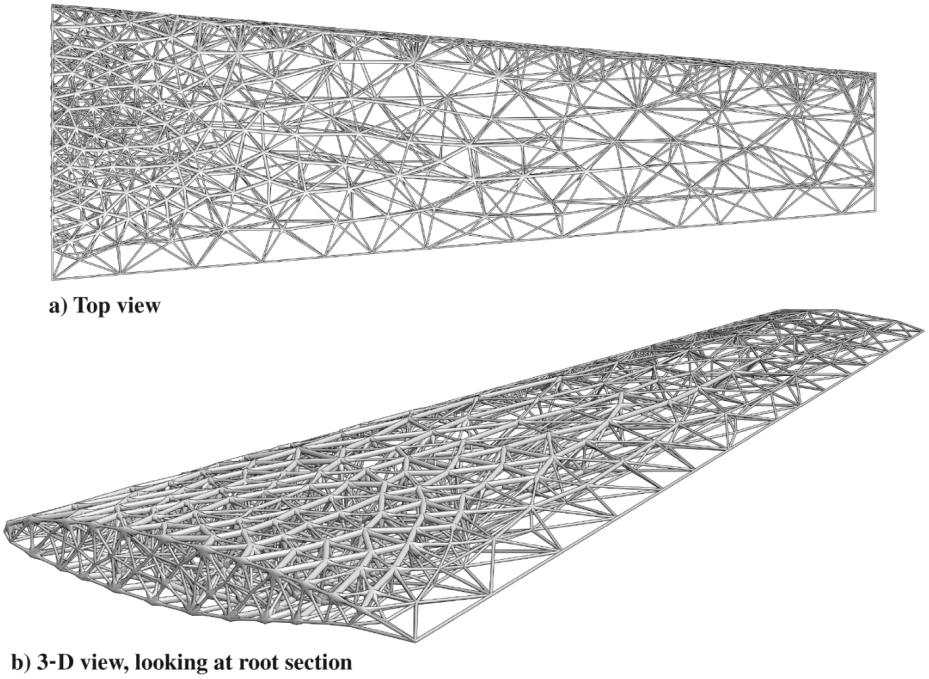

Source: Opgenoord and Willcox (2019).

2.3 Modularity

Most of the topology optimization and designs developed and studied by the works presented in Section 2.2 generate as a result a monolithic structure, that is, the structure is constructed all together (all in one piece). From a manufacturing point of view, this represents major challenges, as it would require high investment in tooling as well as very high quality control. In other words, producing a single structure represents high cost involved and low production volume. On the other hand, when talking about series production line for aircraft, or other products, it is important to guarantee scalability, that is, ease of production in large quantities and low costs.

Along those lines, it comes up with the idea of modularity. Definitions and concepts of modularity generally include many aspects. Among the most commonly referenced definitions of a module is Baldwin *et al.* (2000) definition: "A module is a unit whose structural elements are powerfully connected among themselves and relatively weakly connected to elements in other units" (ARNHEITER; HARREN, 2005; LAU; YAM; TANG, 2007; ERNST, 2005; SCHILLING; STEENSMA, 2001; FREDRIKSSON, 2006). Another definition by Baldwin and Clark (1997) of modularity is also used frequently: "Building a complex product or process from smaller subsystems that can be designed independtly yet function together as a whole" (ASAN; POLAT; SERDAR, 2004; JOSE; TOLLENAERE, 2005; DORAN, 2003; DORAN, 2004; DORAN, 2005; FREDRIKSSON, 2006). Other often referenced definitions are the ones by Ulrich (1994):

> Modularity is the relationship between a product's functional and physical structures such that there is a one-to-one or many-to-one correspondence between the functional and physical structures and unintended interactions between modules are minimized (LAU; YAM; TANG, 2007; JIAO; TSENG, 2000; JOSE; TOLLENAERE, 2005; FREDRIKSSON, 2006).

Several concepts have been associated with modularity. They include architectures and platforms, interchangeability or loose coupling of components, standardization of interfaces, and one-to-one matching of module and function (JACOBS; VICKERY; DROGE, 2007; ARNHEITER; HARREN, 2005; JOSE; TOLLENAERE, 2005). Commonly mentioned benefits of modularization include larger product variety, improved flexibility, simplification of complex

systems, cost savings, etc (JOSE; TOLLENAERE, 2005; VAN *et al.*, 2004; PEKKARINEN; ULKUNIEMI, 2008).

Therefore, regarding wing design, it would be very convenient to have a wing made of modular structures, which would simplify the construction of the wing along with it would make the maintenance, repair and replacement of some parts much easier and much cheaper. Thus, the basic modular structure that comes to mind for such application is truss-based structures, since they are easy to manufacture and assemble, which is the proposal of this thesis.

Searching for application of modular structures in aircraft wings, only a few works were developed. Montemurro, Vincenti and Vannucci (2012) address a two-level procedure for the global optimum design of composite modular structures. The case-study considered is the least weight design of a stiffened wing-box for an aircraft structure. The method is based on the use of the polar formalism and on a genetic algorithm. In the first level of the procedure, the optimal structure is designed as composed by a single equivalent layer, while a laminate realizing the optimal structure is found in the second level. Finistauri, Xi and Walsh (2012) present a discretization method for the development of a modular morphing wing. The proposed method determines the number of morphing wing modules and the respective spacing required to emulate a known wing shape and satisfy a corresponding flight requirement (see Fig. 11).

Figure 11 – Wing discretization.

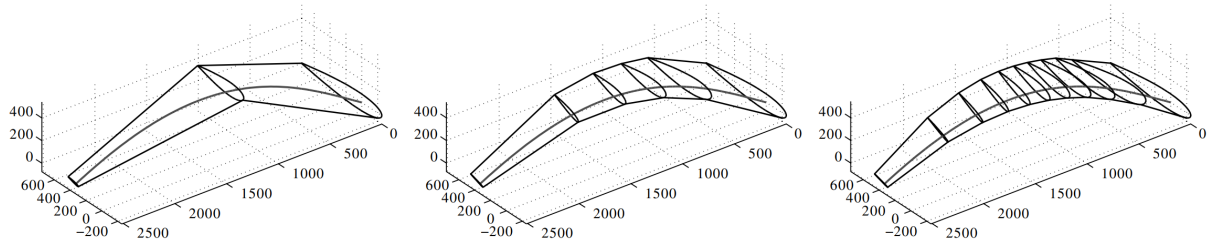

Source: Finistauri, Xi and Walsh (2012).

2.4 Final Considerations

From the concepts and works presented throughout this chapter, it is clear that studies involving the structural design of aircraft wing have always been in vogue. In addition, the need

to develop more efficient aircraft makes engineering seek alternative forms of increasingly light and unconventional structural designs. At the same time, the structural studies developed by the authors were often limited to topological optimization considering monolithic structures, which are difficult to manufacture. Therefore, this thesis seeks to fill this space, contributing with a wing design proposal considering truss-based modular structures. These structures will be optimized and the wing will be evaluated with aeroelastic (flutter and divergence) and buckling constraints.

CHAPTER

3

AERODYNAMIC MODELING

"If you examine a butterfly according to the laws of aerodynamics, it shouldn't be able to fly. But the butterfly doesn't know that, so it flies"

— Howard Schultz

THIS chapter comes up with the aerodynamic modeling used in the aeroelastic coupling for the wing design. Thus, it presents fundamentals of unsteady aerodynamics and the Doublet-Lattice Method, which is used in this work to generate the loads that will be used in the aeroelastic analysis. At the end of the chapter, a verification of the code implementation is presented.

3.1 Fundamentals of Unsteady Aerodynamics

Since the 1920s, unsteady aerodynamics has been studied in order to mathematically determine the pressure distribution on wings that oscillate due to elastic deformations. In this context, the forces necessary in the investigation of dynamic aeroelastic instability phenomena, also known as flutter, which occur above a certain critical speed, can be calculated. Over the decades, flutter considerations have always exerted considerable influence on wing design, as flight speeds increase and the stiffness of increasingly lighter structures decreases (GÜLÇAT, 2010).

Flutter is a destructive phenomenon that deserves special attention in aircraft design. The elements of this phenomenon are structural dynamics and unsteady aerodynamics, of which the

latter is undoubtedly the most complicated and least reliable to model (BLAIR, 1994).

In subsonic or supersonic flows, linearized theories of unsteady aerodynamics generally provide proper results, as long as the modeled aerodynamic surfaces are relatively thin. However, even with the use of these linearized theories, the calculation of forces on three-dimensional wings, considering the different modal shapes, is too time-consuming. This means that, in the initial phases of the aircraft design, the flutter calculations take place through the classical strip theory, in which the aerodynamic derivatives come from two-dimensional theories (GÜLÇAT, 2010).

However, in transonic flows, the physical nonlinearities that characterize aerodynamics lead to major inaccuracies in linearized theories. Another non-linear phenomenon that restricts the use of these theories is the occurrence of flow separation (GÜLÇAT, 2010). None of the cases is considered in this work.

The calculation of structural loads due to atmospheric disturbances is another field in which unsteady aerodynamics finds application (GREENWELL, 2004).

3.1.1 Fundamental Equations

The fundamental equations of fluid dynamics are the Navier-Stokes equations (TEMAM, 2001). It is a set of five equations: the continuity equation, three momentum equations (one in each direction of space) and the energy equation. These equations are developed, for example, by Anderson (2011), and are shown below, in their differential form, i.e., as derived for a fluid element of volume $dx \cdot dy \cdot dz$:

- Continuity Equation:

$$\frac{\partial \rho}{\partial t} + \nabla \cdot (\rho \mathbf{V}) = 0 \tag{3.1}$$

- X-Momentum Equation:

$$\frac{\rho Du}{Dt} = -\frac{\partial p}{\partial x} + \frac{\partial \tau_{xx}}{\partial x} + \frac{\partial \tau_{yx}}{\partial y} + \frac{\partial \tau_{zx}}{\partial z} + \rho f_x \tag{3.2}$$

- Y-Momentum Equation:

$$\frac{\rho Dv}{Dt} = -\frac{\partial p}{\partial y} + \frac{\partial \tau_{xy}}{\partial x} + \frac{\partial \tau_{yy}}{\partial y} + \frac{\partial \tau_{zy}}{\partial z} + \rho f_y \tag{3.3}$$

- Z-Momentum Equation:

$$\frac{\rho Dw}{Dt} = -\frac{\partial p}{\partial z} + \frac{\partial \tau_{xz}}{\partial x} + \frac{\partial \tau_{yz}}{\partial y} + \frac{\partial \tau_{zz}}{\partial z} + \rho f_z \tag{3.4}$$

- Energy Equation:

$$\begin{aligned} \rho \frac{D\left(e+V^2/2\right)}{Dt} = \rho\dot{q} + \frac{\partial}{\partial x}\left(k\frac{\partial T}{\partial x}\right) + \frac{\partial}{\partial y}\left(k\frac{\partial T}{\partial y}\right) + \frac{\partial}{\partial z}\left(k\frac{\partial T}{\partial z}\right) - \nabla\cdot(p\mathbf{V}) + \\ \frac{\partial\left(u\tau_{xx}\right)}{\partial x} + \frac{\partial\left(u\tau_{yx}\right)}{\partial y} + \frac{\partial\left(u\tau_{zx}\right)}{\partial z} + \frac{\partial\left(v\tau_{xy}\right)}{\partial x} + \frac{\partial\left(v\tau_{yy}\right)}{\partial y} + \frac{\partial\left(v\tau_{zy}\right)}{\partial z} + \\ + \frac{\partial\left(w\tau_{xz}\right)}{\partial x} + \frac{\partial\left(w\tau_{yz}\right)}{\partial y} + \frac{\partial\left(w\tau_{zz}\right)}{\partial z} + \rho\mathbf{f}\cdot\mathbf{V} \end{aligned} \tag{3.5}$$

In Equations (3.1) to (3.5), $\mathbf{V}$ is the velocity vector, and its components are u, v and w; $\mathbf{f}$ is the vector of body forces (forces that act remotely on the volumetric mass of the fluid element, such as gravitational forces or electromagnetic forces) per unit mass, and its components are f_x, f_y and f_z; ρ is the local density of the fluid; p is the pressure; τ_{ij} represents a normal stress (in which case $i = j$) or shear stress ($i \neq j$) in j direction acting on the perpendicular plane to axis i; the variable e corresponds to the internal energy of the fluid per unit of mass; q is the volumetric heating rate per unit mass; k is the thermal conductivity of the fluid; and finally T is the local temperature.

The substantial derivative is an operator defined by Anderson (2011) as:

$$\frac{D}{Dt}(\cdot) \equiv \frac{\partial}{\partial t}(\cdot) + \mathbf{V}\cdot\nabla(\cdot) \tag{3.6}$$

In so-called Newtonian fluids, the normal and shear stresses are proportional to the velocity gradients in the fluid. In most studies of aerodynamics, the fluid can be considered Newtonian. The proportionality constants are directly related to the fluid viscosity.

According to the aforementioned assumptions, the fluid dynamics equations can belong to different levels. Usually, body forces are neglected. The so-called Euler equations are obtained from the general Navier-Stokes equations, disregarding the terms associated with viscosity and also with heat transfer in the fluid. Thus, Euler's equations are given by:

- Continuity Equation:

$$\frac{\partial \rho}{\partial t} + \nabla\cdot(\rho\mathbf{V}) = 0 \tag{3.7}$$

- Momentum Equation:

$$\frac{\rho D\mathbf{V}}{Dt} = -\frac{1}{\rho}\nabla p \tag{3.8}$$

- Energy Equation:

$$\rho\frac{D\left(e+V^2/2\right)}{Dt} = -\nabla\cdot(p\mathbf{V}) \tag{3.9}$$

Considering the case of determining the values of p, ρ, u, v and w in the flow, one can see that there are only four equations involving these quantities (the continuity equation and the momentum equations). A fifth equation is needed, which is achieved by adopting an equation of state for the fluid. For example, the following isentropic relationship can be adopted as an equation of state (BLAIR, 1994):

$$\frac{p}{\rho^\gamma} = \frac{p_0}{\rho_0^\gamma} \tag{3.10}$$

The constant γ is the ratio of specific heats at constant pressure and volume: $\gamma = c_p/c_v$. The variables p_0 and ρ_0 are constant reference values of pressure and density, respectively. The ratio defined in Equation (3.10) is constant for any fluid element.

The speed of sound in the fluid can also be calculated by the expression (ANDERSON, 2011; BLAIR, 1994):

$$a^2 = \frac{\mathrm{d}p}{\mathrm{d}\rho} \tag{3.11}$$

At a lower level, the flow is irrotational, such that the fluid velocity meets the following relations (BLAIR, 1994):

$$\nabla\times\mathbf{V} = \mathbf{0} \Longleftrightarrow \mathbf{V} = \nabla\Phi \qquad \text{(Irrotational flow)} \tag{3.12}$$

The function $\Phi = \Phi(x,y,z,t)$, which corresponds to a new state variable, is a scalar function that denotes the velocity potential.

Combining Equations (3.8), (3.12), (3.11) and (3.12), the following equation is obtained:

$$\nabla\left(\frac{\partial\Phi}{\partial t} + \frac{V^2}{2} + \int\frac{\mathrm{d}p}{\mathrm{d}\rho}\right) = 0 \tag{3.13}$$

Thus, the constant of integration of equation (3.13) should only be a function of time:

$$\frac{\partial\Phi}{\partial t} + \frac{V^2}{2} + \int\frac{\mathrm{d}p}{\mathrm{d}\rho} = F(t) \tag{3.14}$$

Equation (3.14) is called Kelvin's equation and corresponds to a unsteady version of Bernoulli's equation (BLAIR, 1994).

The function $F(t)$ has no physical meaning, i.e., it is only a mathematical solution so far. A physical meaning for it can be obtained with the condition that the flow, remotely, in a region free of disturbances, is stationary and has parallel and straight streamlines (BISPLINGHOFF; ASHLEY; HALFMAN, 1996). Therefore, in this region, the velocity potential Φ is independent of time, the pressure is constant, and the velocity is a constant V_∞. Mathematically, $\frac{\partial \Phi}{\partial t} = 0$, $V^2 = V_\infty^2$ and $\mathrm{d}p = 0$, so that it becomes:

$$F(t) = \frac{V_\infty^2}{2} \tag{3.15}$$

The velocity potential can be redefined so that:

$$\phi = \Phi - \int_0^t F(\tau) d\tau = \Phi - \frac{V_\infty^2 t}{2} \tag{3.16}$$

Thus, the final momentum equation becomes:

$$\frac{\partial \phi}{\partial t} + \frac{V^2}{2} + \int \frac{\mathrm{d}p}{\mathrm{d}\rho} = 0 \tag{3.17}$$

The continuity equation in (3.7) can also be manipulated using Equations (3.10), (3.11), (3.12), (3.16) and (3.17) in order to obtain the following equation, the so-called full potential equation (BLAIR, 1994):

$$\nabla^2 \phi - \frac{1}{a^2}\left[\frac{\partial^2 \phi}{\partial t^2} + \frac{\partial}{\partial t} V^2 + \nabla\phi \cdot \nabla\left(\frac{V^2}{2}\right)\right] = 0 \tag{3.18}$$

Since the speed of sound a can also be expressed as a function of the velocity potential (ϕ), Equation (3.18) has only this velocity potential as unknown (BISPLINGHOFF; ASHLEY; HALFMAN, 1996). Thus, the system that initially had five unknown variables and five equations was reduced based on the previously mentioned simplifications to a system with only one equation and one unknown.

3.1.2 Linearization of the Full Potential Equation

The doublet-lattice method is a linear method. The full potential equation, in the form presented in Equation (3.18), is clearly non-linear. Thus, in order to proceed to the formulation of the doublet-lattice method, it is necessary to linearize it. The linearization can be done considering that the unknown $\phi = \phi(x,y,z,t)$ splits into two components: a stationary component, $\bar{\phi}(x,y,z)$, and a component of small perturbations and time-dependent, $\tilde{\phi}(x,y,z,t)$; consequently, the same assumption is applied to the pressure and density in the fluid. The speed of sound, on the contrary, can be admitted as invariant in time, since a contrary hypothesis does not influence the result of linearization (BLAIR, 1994).

Linearization also assumes that a steady-state solution to the full potential equation exists, and, furthermore, assumes that the steady-state flow is simply a flow with velocity V_∞ in the x-direction and with a constant speed of sound equals to a_0. The hypotheses adopted are summarized below:

$$\begin{aligned} \phi(x,y,z,t) &= \bar{\phi}(x,y,z) + \tilde{\phi}(x,y,z,t) \\ a(x,y,z,t) &= \bar{a}(x,y,z) = a_\infty \\ \bar{\phi}(x,y,z) &= V_\infty x \end{aligned} \tag{3.19}$$

Having the Mach number defined as $M_\infty = V_\infty / a_\infty$, the linearized equation becomes:

$$\left(1 - M_\infty^2\right)\tilde{\phi}_{xx} + \tilde{\phi}_{yy} + \tilde{\phi}_{zz} - \left(\frac{2V_\infty}{a_\infty^2}\right)\tilde{\phi}_{xt} - \left(\frac{1}{a_\infty^2}\right)\tilde{\phi}_{tt} = 0 \tag{3.20}$$

The linear partial differential equation given by (3.20) is the fundamental equation in the description of aerodynamic behavior, which is used in the linear methods such as the Doublet-Lattice Method (DLM).

However, since the aerodynamic behavior is much better analyzed through the knowledge of the pressure distributions, and not the velocity potential, it is necessary to develop an expression that relates the pressure with the velocity potential obtained as a solution to Equation (3.20). According to Blair (1994), such expression is given by:

$$p - p_0 = -\rho_0\left(\tilde{\phi}_t + V_\infty \tilde{\phi}_x\right) \tag{3.21}$$

3.1.3 Linearized Boundary Conditions

The boundary conditions of the problem given by the linear partial differential equation (3.20) must specify the value of the velocity potential or a directional derivative of such potential (which is equivalent to a component of the velocity vector) on all surfaces that define the problem domain. Regarding the flow around a body, the domain is defined internally by its surface and by the wake generated by itself and, externally, by the conditions of the undisturbed remote flow.

It is usual to define the reference fixed to the body. Its surface can be expressed by the equation:

$$S(x,y,z,t) = 0 \tag{3.22}$$

If the body is an aircraft, it is evidently difficult to determine an analytic expression for $S(x,y,z,t)$ valid for the entire aircraft, but it is always possible to determine valid expressions in smaller domains.

The boundary condition in the body is that the flow is tangent to its surface, that is, at any point on the body-fluid interface, at any instant, the relative velocity component normal to the surface must be zero (BECKER, 1967), i.e:

$$\frac{DS}{Dt} = \frac{\partial S}{\partial t} + \mathbf{V}\cdot\nabla S = 0, \quad \text{em } S(x,y,z,t) = 0 \tag{3.23}$$

Regarding the DLM, it is appropriate to have Equation (3.23) linearized, considering if for the case of a thin wing (or any lifting surface). Any wing can be well characterized by its mean surface $h_m(x,y,t)$ and by its envelope of thickness $h_t(x,y,z)$, so that Equation (3.22) becomes:

$$S_{wing}(x,y,z,t) = z - [h_m(x,y,t) \pm h_t(x,y,t)] = 0 \tag{3.24}$$

For linearized flow around a free flow condition with velocity $U\mathbf{i}$, adopting the perturbation velocities $u\mathbf{i}$, $v\mathbf{j}$ and $w\mathbf{k}$, the velocity vector is given by:

$$\mathbf{V} = (U+u)\mathbf{i} + (v)\mathbf{j} + (w)\mathbf{k} \tag{3.25}$$

Substituting Equations (3.24) and (3.25) into (3.23), considering $h = h_m \pm h_t$, it follows:

$$-\frac{\partial h}{\partial t} - (U+u)\frac{\partial h}{\partial x} - (v)\frac{\partial h}{\partial y} + w = 0 \tag{3.26}$$

What is desired is a linear relationship between the velocity components on the surface of the wing and the function $h(x,y,t)$. Ignoring the nonlinear terms in Equation (3.26),

$$w = \frac{\partial h}{\partial t} + U\frac{\partial h}{\partial x} \tag{3.27}$$

Thus, it is clear that the components of $h = h_m \pm h_t$ can be treated independently in the boundary condition (3.27). Normally, it is assumed that only the mean surface is a function of time, not the thickness envelope. So the dynamic response due to $h_m(x,y,t)$ can be superimposed on a time-independent solution that contemplates $h_t(x,y)$(BLAIR, 1994).

The boundary condition of the remote flow, that it is undisturbed, in turn, can be automatically satisfied with the choice of a superposition of sources or dipoles to solve the flow over the body, since their influence decays to zero at infinite distances (BLAIR, 1994).

Finally, there is also the boundary condition in the wake of the flow downstream the body. The typical boundary condition for ideal flow (incompressible and inviscid) around an airfoil is the Kutta condition, according to which the flow at the trailing edge of the airfoil must be smooth and with finite velocity (BECKER, 1967). For stationary and linearized compressible flow, the Prandtl-Glauert transformation can be used so that the Kutta condition is applicable as it would be in incompressible flow (BLAIR, 1994). The problem is really the unsteady flow.

Some experiments have show that the trailing edge flow may not be tangent in unsteady flows, as presented by Blair (1994). For linearized unsteady flow, the only boundary condition associated with the wake is the property that no pressure difference across the wake exists.

3.1.4 Elementary Solutions of the Linearized Aerodynamic Potential Equation

The starting point for the elaboration of the DLM is based on the partial differential equation (PDE) in Equation (3.20) for the behavior of small perturbations of the velocity potential ϕ in inviscid, irrotational and compressible flow, linearized around a uniform, parallel flow with the parallel and uniform flow, with velocity V_∞ along from the x-axis.

The DLM employs the linearity of Equation (3.20) to solve complex problems by superposition of elementary aerodynamic solutions (source, sink and vortex flows). For small

perturbations around the uniform mean flow V_∞ along the x-direction, the Prandtl's acceleration potential (Ψ) only differs from the pressure by a constant:

$$\Psi = \frac{p - p_\infty}{\rho_\infty} \tag{3.28}$$

It is related to the velocity potential by the material derivative:

$$\Psi(x,y,z,t) = \left[\frac{\partial}{\partial t} + V_\infty \frac{\partial}{\partial x}\right] \phi(x,y,z,t) \tag{3.29}$$

which gives the inverse relation:

$$\phi(x,y,z,t) = \frac{1}{V_\infty} \int_{-\infty}^{x} \Psi\left(\lambda, y, z, t - \frac{x-\lambda}{V_\infty}\right) \mathrm{d}\lambda \tag{3.30}$$

where λ is the integration variable. The acceleration potential satisfies the solution for Equation (3.20). Thus, the acceleration potential induced at a receiving point (x,y,z) by a source in (ξ,η,ζ) can be defined as:

$$\Psi_{\text{source}}\,(x,y,z,\xi,\eta,\zeta,t) = \frac{1}{R} f_\Psi(t-\tau) \tag{3.31}$$

where f_Ψ is the perceived strength of the source, a function of time and the delay required for a disturbance to travel from the emitting source point to the receiving point:

$$\tau = \frac{-M_\infty(x-\xi) + R}{a_\infty \beta_\infty^2} \tag{3.32}$$

where R is the hyperbolic radius, given by:

$$R \equiv \left[(x-\xi)^2 + \beta_\infty^2 (y-\eta)^2 + \beta_\infty^2 (z-\zeta)^2\right]^{1/2} \tag{3.33}$$

and the Prandtl-Glauert factor is given by:

$$\beta_\infty^2 \equiv 1 - M_\infty^2 \tag{3.34}$$

The analysis is restricted to sinusoidal harmonic solutions in the form $\Psi_{\text{source}} = A_\Psi e^{(i\omega t)}$, where A_Ψ is the amplitude, ω the oscillation frequency and $i \equiv \sqrt{-1}$ the imaginary unit. The acceleration potential acceleration source function can be written as:

$$\Psi_{\text{source}} = \frac{A_\Psi}{R} e^{[i\omega(t-\tau)]} = \frac{A_\Psi}{R} e^{(-i\omega\tau)} e^{(i\omega t)} = \bar{\Psi}_{\text{source}}\, e^{(i\omega t)} \tag{3.35}$$

where $\bar{\Psi}_{\text{source}}(x,y,z,\xi,\eta,\zeta)$ is the modulus. Therefore, using Equation (3.32), the following relation is obtained:

$$\bar{\Psi}_{\text{source}} = \frac{A_\Psi}{R}\exp\left[\frac{i\omega}{a_\infty\beta_\infty^2}\left[M_\infty(x-\xi)-R\right]\right] \tag{3.36}$$

Equation (3.36) is the solution for an oscillating source in harmonic motion in terms of pressure. Following the development, it is necessary to formulate an elementary solution to Equation (3.20) that can generate a pressure differential. To do so, the concept of elementary aerodynamic flow of doublet is introduced, constructed by a superimposition of two infinitesimally adjacent source flows of equal but opposite strengths (see Fig. 12).

Figure 12 – Construction of a doublet from two infinitesimally adjacent source flows of equal but opposite strengths.

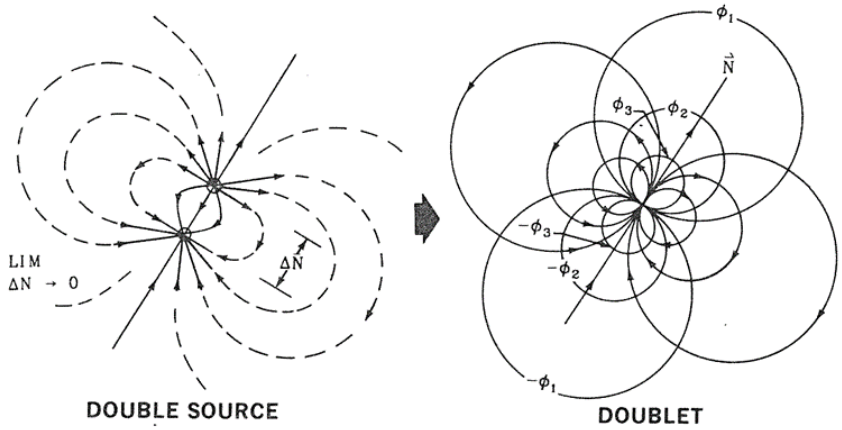

Source: Giesing (1985).

Mathematically, this is equivalent to taking the directional derivative of the expression for the source solution Ψ_{source} along the vector $\vec{N}_s$ separating the source and the sink; in practice, $\vec{N}_s$ is the normal vector of the lifting surface at (ξ,η,ζ). Thus,

$$\Psi_{\text{doublet}} \equiv \bar{\Psi}_{\text{doublet}}\exp(i\omega t) = \frac{\partial\Psi_{\text{source}}}{\partial N_s} \tag{3.37}$$

with modulus

$$\bar{\Psi}_{\text{doublet}} = \frac{\partial}{\partial N_s}\left\{\frac{A_\Psi}{R}\exp\left[\frac{i\omega}{a_\infty\beta_\infty^2}\left[M_\infty(x-\xi)-R\right]\right]\right\} \tag{3.38}$$

3.1.5 Equation for Pressure Doublet Sheet and its Kernel Function

The desired elementary solution is represented by Equation (3.38). Thus, to model the pressure difference generated by a thin wing, it is necessary to formulate an integral formula for the downwash (or normalwash) induced by a continuous sheet of acceleration potential doublets. Additional information is presented by Vivian and Andrew (1965).

When substituting Equation (3.30) into (3.38), the magnitude of the velocity potential induced by an acceleration potential doublet can be expressed by:

$$\begin{aligned}&\bar{\phi}(x,y,z,\xi,\eta,\zeta) = \\ &-\frac{A_\Psi}{V_\infty}\frac{\partial}{\partial N_s}\exp\left[\frac{i\omega}{V_\infty}(x-\xi)\right]\int_{-\infty}^{x-\xi}\frac{1}{R'}\exp\left\{i\omega\left[\frac{\lambda}{V_\infty}+\frac{M_\infty\lambda}{a_\infty\beta_\infty^2}-\frac{R'}{a_\infty\beta_\infty^2}\right]\right\}\mathrm{d}\lambda\end{aligned} \tag{3.39}$$

where the radial measure R' in the integrand is a function of the integration variable λ,

$$R' \equiv \left[\lambda^2+\beta_\infty^2(y-\eta)^2+\beta_\infty^2(z-\zeta)^2\right]^{1/2} \tag{3.40}$$

The normal velocity component $\bar{w}_N$ induced at some receiving point (x,y,z) is obtained from the velocity potential by differentiation along the local surface normal $\vec{N}_r$:

$$\begin{aligned}&\bar{w}_N(x,y,z,\xi,\eta,\zeta) = \\ &-\frac{A_\Psi}{V_\infty}\frac{\partial}{\partial N_r}\frac{\partial}{\partial N_s}\exp\left[\frac{i\omega}{V_\infty}(x-\xi)\right]\int_{-\infty}^{x-\xi}\frac{1}{R'}\exp\left\{i\omega\left[\frac{\lambda}{V_\infty}+\frac{M_\infty\lambda}{a_\infty\beta_\infty^2}-\frac{R'}{a_\infty\beta_\infty^2}\right]\right\}\mathrm{d}\lambda\end{aligned} \tag{3.41}$$

The directional derivatives can be decomposed as:

$$\begin{aligned}\frac{\partial}{\partial N_s} &= \cos\Gamma_s\frac{\partial}{\partial z}-\operatorname{sen}\Gamma_s\frac{\partial}{\partial y} \\ \frac{\partial}{\partial N_r} &= \cos\Gamma_r\frac{\partial}{\partial z}-\operatorname{sen}\Gamma_r\frac{\partial}{\partial y}\end{aligned} \tag{3.42}$$

where Γ_s and Γ_r denotes, respectively, the angle between the surface and the xy-plane at the sending point s and receiving point r. Notice that $\exp[i\omega(x-\xi)/V_\infty]$ has been taken out of the integral, as it is independent of the normal direction $\vec{N}_s$ and $\vec{N}_r$.

The pressure differential induced by an infinitesimal element of the acceleration potential doublets sheet is related to its strength A_Ψ as

$$\Delta\bar{p} = 4\pi\rho_\infty A_\Psi \mathrm{d}\xi\,\mathrm{d}\sigma \tag{3.43}$$

with ξ and σ the tangential coordinates. Substituting Equation (3.43) into the expression for the normal velocity magnitude (3.41), integrating over a sheet S of pressure doublets and dividing

by V_∞, the following integral equation in non-dimensional form is obtained:

$$\frac{\bar{w}_N}{V_\infty} = \frac{-1}{4\pi\rho_\infty V_\infty^2} \iint_S \Delta\bar{p}(\xi,\eta,\zeta) K(x-\xi, y-\eta, z-\zeta) \mathrm{d}\xi \mathrm{d}\sigma \tag{3.44}$$

Simplifying Equation (3.44), the so-called *Kernel function K* is obtained:

$$K(x_0,y_0,z_0) \equiv \exp\left[\frac{i\omega x_0}{V_\infty}\right] \frac{\partial}{\partial N_r}\frac{\partial}{\partial N_s} \int_{-\infty}^{x_0} \frac{1}{R'} \exp\left[i\omega \frac{\lambda - M_\infty R'}{V_\infty \beta_\infty^2}\right] \mathrm{d}\lambda \tag{3.45}$$

where the relative coordinate system (x_0, y_0, z_0) is defined as:

$$\begin{aligned} x_0 &\equiv x - \xi \\ y_0 &\equiv y - \eta \\ z_0 &\equiv z - \zeta \end{aligned} \tag{3.46}$$

The integral equation (3.44) relates the unknown pressure differential $\Delta\bar{p}$ generated by a thin lifting surface, modeled as a sheet of acceleration potential doublets, to the velocity normal to the surface $\bar{w}_N$ (known as downwash or normalwash) in a receiving point.

Evaluating the Kernel function (3.45) is not trivial, since it shows a singular behavior when the receiving point approaches the doublet sheet. Vivian and Andrew (1965) show that the Kernel function may be rewritten as:

$$K(x_0,y_0,z_0) = \exp\left[\frac{-i\omega x_0}{U_\infty}\right] \frac{K_1 T_1 + K_2 T_2}{r^2} \tag{3.47}$$

where $r \equiv \left(y_0^2 + z_0^2\right)^{1/2}$ and

$$T_1 = \cos(\Gamma_r - \Gamma_s) \tag{3.48}$$

$$T_2 = \left[\frac{z_0}{r}\cos\Gamma_r - \frac{y_0}{r}\sin\Gamma_r\right]\left[\frac{z_0}{r}\cos\Gamma_s - \frac{y_0}{r}\sin\Gamma_s\right] \tag{3.49}$$

Landahl (1967) proposes a simplified expression for the terms K_1 and K_2, given by:

$$K_1 = I_1 + \frac{M_\infty r}{R} \frac{\exp(-ik_1 u_1)}{\left(1+u_1^2\right)^{1/2}} \tag{3.50}$$

$$K_2 = -3I_2 - \frac{ik_1 M_\infty^2 r^2}{R^2} \frac{\exp(-ik_1 u_1)}{\left(1+u_1^2\right)^{1/2}} - \frac{M_\infty r}{R}\left[\left(1+u_1^2\right)\frac{\beta_\infty^2 r^2}{R^2} + \frac{M_\infty r u_1}{R} + 2\right] \frac{\exp(-ik_1 u_1)}{\left(1+u_1^2\right)^{3/2}} \tag{3.51}$$

with

$$k_1 \equiv \frac{\omega r}{U_\infty} \tag{3.52}$$

$$u_1 \equiv \frac{M_\infty R - x_0}{\beta_\infty^2 r} \tag{3.53}$$

and the integrals

$$I_1(u_1,k_1) \equiv \int_{u_1}^{\infty} \frac{\exp(-ik_1u_1)}{(1+u^2)^{3/2}}\,\mathrm{d}u \tag{3.54}$$

$$I_2(u_1,k_1) \equiv \int_{u_1}^{\infty} \frac{\exp(-ik_1u_1)}{(1+u^2)^{5/2}}\,\mathrm{d}u \tag{3.55}$$

The hyperbolic radius is redefined in terms of the new coordinates:

$$R = \left(x_0^2 + \beta_\infty^2 r^2\right)^{1/2} \tag{3.56}$$

The integral I_1 and I_2 are to be evaluated numerically. Integration by parts yields:

$$I_1(u_1,k_1) = \exp(-ik_1u_1)\left\{1 - \frac{u_1}{\left(1+u_1^2\right)^{1/2}} - ik_1 I_0(u_1,k_1)\right\} \tag{3.57}$$

$$\begin{aligned} 3I_2(u_1,k_1) = \exp(-ik_1u_1)\Bigg\{&(2+ik_1u_1)\left[1 - \frac{u_1}{\left(1+u_1^2\right)^{1/2}}\right] \\ &- \frac{u_1}{\left(1+u_1^2\right)^{3/2}} - ik_1 I_0(u_1,k_1) + k_1^2 J_0(u_1,k_1)\Bigg\} \end{aligned} \tag{3.58}$$

with I_0 and J_0 the integrals:

$$I_0(u_1,k_1) \equiv \exp(ik_1u_1)\int_{u_1}^{\infty}\left[1 - \frac{u}{(1+u^2)^{1/2}}\right]\exp(-ik_1u)\,\mathrm{d}u \tag{3.59}$$

$$J_0(u_1,k_1) \equiv \exp(ik_1u_1)\int_{u_1}^{\infty}\left[1 - \frac{u}{(1+u^2)^{1/2}}\right]u\exp(-ik_1u)\,\mathrm{d}u \tag{3.60}$$

Laschka (1963) proposes an accurate approximation of I_0 and J_0 for $u_1 \geq 0$:

$$I_0(u_1,k_1) \approx \sum_{n=1}^{11} \frac{a_n \exp(-ncu_1)}{n^2c^2 + k_1^2}(nc - ik_1) \tag{3.61}$$

$$\begin{aligned} J_0(u_1,k_1) \approx \sum_{n=1}^{11} \frac{a_n \exp(-ncu_1)}{\left(n^2c^2+k_1^2\right)^2}\Big\{&n^2c^2 - k_1^2 + ncu_1\left(n^2c^2+k_1^2\right) \\ &- ik_1\left[2nc + u_1\left(n^2c^2+k_1^2\right)\right]\Big\} \end{aligned} \tag{3.62}$$

Table 1 – Coefficients for Laschka's L11 approximation.

n	coefficients a_n(L11)
1	0.24186198
2	-2.7918027
3	24.991079
4	-111.59196
5	271.43549
6	-305.75288
7	-41.183630
8	545.98537
9	-644.78155
10	328.72755
11	-64.279511

Source: Laschka (1963).

with the constant $c = 0.372$ and the coefficients a_n as given in Table 1. The error induced by this approximation has been shown not to exceed 0.135%.

In order to evaluate I_1 and I_2 for $U_1 < 0$, symmetry of the formulation is applied, where the overbar denotes the complex conjugate:

$$I_1(u_1,k_1) = 2\,\mathrm{Re}\,I_1(0,k_1) - \bar{I}_1(-u_1,k_1) \tag{3.63}$$

$$I_2(u_1,k_1) = 2\,\mathrm{Re}\,I_2(0,k_1) - \bar{I}_2(-u_1,k_1) \tag{3.64}$$

3.1.6 DLM Implementation

In general, the DLM consists of a numerical-computational procedure for solving the integral equation (3.44). The normal component of the velocity (normalwash) is a known parameter from the boundary conditions discussed in Section 3.1.3. The unknown parameter is the pressure difference δp over the lifting surface. The pressure function is inside the integrand, which is not trivial to solve it. Therefore, the DLM formulation is extended to the discretization of the surface in trapezoidal elements, called boxes or panels. In each panel, the unknown pressure function is idealized by an approximation, initially proposed as parabolic (ALBANO; RODDEN, 1969) and later refined to quartic (RODDEN; TAYLOR; JR, 1998) using doublets line with unknown coefficients to be determined.

Albano and Rodden (1969) proposed an extension to the VLM, subdividing the wing area into panels aligned in the chord direction with respect to the relative wind (see Fig. 13), where the resulting total pressure on each panel is considered constant.

Figure 13 – Discretization of the lifting surface geometry.

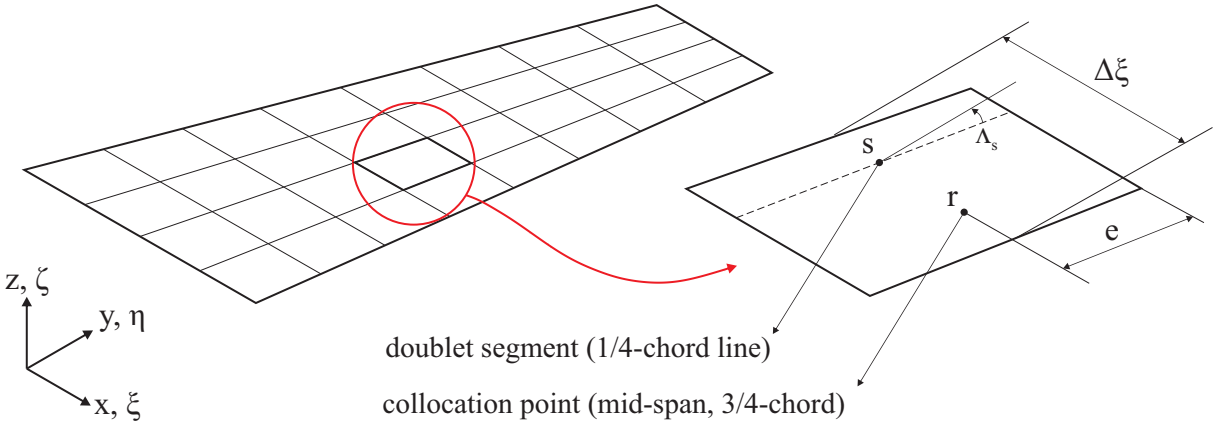

Source: Elaborated by the author.

Along those lines, Equation (3.44) for the induced normalwash at a receiving panel r becomes a sum of the contributions from each emitting panel s:

$$\begin{aligned}\frac{\bar{w}_{N,r}}{V_\infty} &= \sum_s \frac{-\Delta\bar{p}_s \Delta x_s}{4\pi\rho_\infty V_\infty^2} \iint_s K(x-\xi, y-\eta, z-\zeta)\mathrm{d}\xi\mathrm{d}\sigma \\ &= \sum_s -\Delta\bar{c}_{p,s}\frac{\Delta x_s}{8\pi} \iint_s K(x-\xi, y-\eta, z-\zeta)\mathrm{d}\xi\mathrm{d}\sigma\end{aligned} \tag{3.65}$$

where δx_s is the chord of the emitting panel and $\Delta\bar{c}_{p,s}$ is the non-dimensional pressure coefficient given by:

$$\Delta\bar{c}_{p,s} = \frac{\Delta\bar{p}_s}{\frac{1}{2}\rho_\infty V_\infty^2} \tag{3.66}$$

The normalwash is evaluated at the control point or collocation point, which are place at three-quarters of the panel chord ($^3/_4-$chord line) and at half span. The choice for the placement is based on empirical analysis and is sometimes defined as a rule ($^1/_4 - {}^3/_4$ rule) that leads to optimal results and satisfies the Kutta condition on the trailing edge, as demonstrated by Pistolesi's theorem.

Equation (3.65) for DLM can be defined as a linear system, with the number of equations equal to the number of panels used in the discretization:

$$\{\bar{w}_N\} = [D]\{\Delta\bar{c}_p\} \tag{3.67}$$

where $n_{\text{tot}} \times n_{\text{tot}}$ matrix $[D]$ is the complex square matrix relating the pressure difference, or lift pressure, due to normalwash influence from one panel to another. In addition, Eq. (3.67) can be rewritten accounting for the influence of the receiving panel (r) and emitting panel (s) as:

$$\bar{w}_{N,r} = \sum_{s=1}^{n_{\text{tot}}} D_{rs} \Delta \bar{c}_{p,s} \tag{3.68}$$

where D_{rs} is the so-called matrix of *total downwash factors* and is a square matrix of size $n_{\text{tot}} \times n_{\text{tot}}$ equal to the total number of panels:

$$D_{rs} \equiv \frac{\Delta x_s}{8\pi} \int_s K\left(x - \xi_{1/4}, y - \eta, z - \zeta\right) \mathrm{d}\sigma \tag{3.69}$$

and its inverse matrix is used to determine the distribution of oscillatory pressure over the surface:

$$[AIC] = [D_{rs}]^{-1} \tag{3.70}$$

where $[AIC]$ is known as the *aerodynamics influence coefficients matrix*.

The steady component of the downwash factors can be computed by the derived kernel function. Once Eq. (3.65) is dependent on the reduced frequency k and the Mach number, it can be shown that for steady flows, that is, with zero reduced frequency, the DLM converges to the VLM (HEDMAN, 1966).

Albano and Rodden (1969) and Rodden, Taylor and Jr (1998) state that the steady component of the downwash factor D_{rs} may be computed exactly, whereas then integral in Eq. (3.69) is only approximated. Thus, the results may be improved by restricting the approximation to the *incremental* downwash factor D'_{rs}, obtained by subtracting the limiting value $K^{(0)} \equiv \lim_{\omega \to 0} K$ from the integrand. The steady contribution $D^{(0)}_{rs}$ of a horseshow vortex is determined exactly and added a posteriori:

$$D_{rs} = D^{(0)}_{rs} + D'_{rs} \tag{3.71}$$

The low-frequency limit $K^{(0)}$ of the Kernel function K is given by (VIVIAN; ANDREW, 1965; ALBANO; RODDEN, 1969):

$$K^{(0)}_1 \equiv \lim_{\omega \to 0} K_1 = 1 + \frac{x_0}{R} \tag{3.72}$$

$$K^{(0)}_2 \equiv \lim_{\omega \to 0} K_2 = -2 - \frac{x_0}{R}\left(2 + \frac{\beta^2_\infty r^2}{R^2}\right) \tag{3.73}$$

At this point, the original version of the method proposed by Albano and Rodden (1969) admits that the shape of the pressure distributed along the doublets line assumes a parabolic distribution to fit the numerator of the integrand in the Kernel function of Eq. (3.47). Later on, Rodden, Taylor and Jr (1998) developed an improved version that allows a quartic approximation of the doublet line, which guarantees greater stability and improvements for the method, mainly in specific configurations of swept wing geometries with high aspect ratio ($\mathcal{AR}$) and conditions of high reduced frequencies.

In this work, both methods were implemented and the differences in the results are briefly pointed out. Although there is a computational gain through the use of the quartic approximation method in some cases (where greater refinement is needed if a parabolic approximation is used), the use of a parabolic approximation does not compromise the effectiveness of the DLM for simpler geometries, with low $\mathcal{AR}$, and lower values of reduced frequency.

3.1.6.1 Parabolic Approximation of the Integrand

In the parabolic approximation the fit is performed along the doublet line in each element coordinate $\bar{\eta}$ over the spanwise element (e). Thus, the oscillatory incremental os defined as:

$$D'_{rs} = \frac{\Delta x_s}{8\pi} \int_{-e}^{+e} \frac{P(\bar{\eta})}{r^2} \, \mathrm{d}\bar{\eta} \tag{3.74}$$

where $P(\bar{\eta})$ is defined as the parabolic approximation:

$$P(\bar{\eta}) = A\bar{\eta}^2 + B\bar{\eta} + C \approx (K_1 T_1 + K_2 T_2) \exp\left[\frac{-i\omega}{V_\infty}(\bar{x} - \bar{\eta}\tan\Lambda_s)\right] - \left(K_1^{(0)} T_1 + K_2^{(0)} T_2\right) \tag{3.75}$$

where the overbar denotes that the coordinates are defined in the plane of the sending element, relative to the center (ξ_c, η_c, ζ_c) of the doublet segment:

$$\bar{x} \equiv x - \xi_c \qquad \bar{\xi} \equiv \xi - \xi_c$$

$$\bar{y} \equiv (y - \eta_c)\cos\Gamma_s + (z - \zeta_c)\sin\Gamma_s \qquad \bar{\eta} \equiv (\eta - \eta_c)\cos\Gamma_s + (\zeta - \zeta_c)\sin\Gamma_s$$

$$\bar{z} \equiv (z - \zeta_c)\cos\Gamma_s - (y - \eta_c)\sin\Gamma_s \qquad \bar{\zeta} \equiv (\zeta - \zeta_c)\cos\Gamma_s - (\eta - \eta_c)\sin\Gamma_s$$

where Γ_s and Λ_s are the dihedral and sweep angles of the emitting panel.

Rodden, Giesing and Kalman (1972) improved this approximation distinguishing the planar and non-planar terms in the expression for the incremental downwash factor D'_{rs}:

$$D_{rs} = D_{rs}^{(0)} + D_{rs}^{(1)} + D_{rs}^{(2)} \tag{3.76}$$

where the superscripts $^{(0)}$, $^{(1)}$ and $^{(2)}$ denote, respectively, the steady, planar unsteady and non-planar unsteady contributions. Skipping the derivation process here, those terms are given by:

$$D_{rs}^{(1)} = \frac{\Delta x_s}{8\pi} \int_{-e}^{+e} \frac{P_1(\bar{\eta})}{r^2} \, \mathrm{d}\bar{\eta} \tag{3.77}$$

$$D_{rs}^{(2)} = \frac{\Delta x_s}{8\pi} \int_{-e}^{+e} \frac{P_2(\bar{\eta})}{r^4} \, \mathrm{d}\bar{\eta} \tag{3.78}$$

with

$$P_1(\bar{\eta}) \equiv A_1\bar{\eta}^2 + B_1\bar{\eta} + C_1 \approx \left\{ K_1 \exp\left[\frac{-i\omega\left(\bar{x} - \bar{\eta}\tan\Lambda_s\right)}{U_\infty} \right] - K_1^{(0)} \right\} T_1 \tag{3.79}$$

$$P_2(\bar{\eta}) \equiv A_2\bar{\eta}^2 + B_2\bar{\eta} + C_2 \approx \left\{ K_2 \exp\left[\frac{-i\omega\left(\bar{x} - \bar{\eta}\tan\Lambda_s\right)}{U_\infty} \right] - K_2^{(0)} \right\} T_2^* \tag{3.80}$$

where $T_2^* \equiv r^2 T_2$.

The coefficients A_1, B_1, C_1 and A_2, B_2, C_2 of the parabolic approximation are obtained from the value of the Kernel numerator at three points along the doublet line: $\bar{\eta} = -e$ (inboard), $\bar{\eta} = 0$ (midspan) and $\bar{\eta} = +e$ (outboard). Thus, those coefficients are given by:

$$A_1 = \left[P_1(+e) - 2P_1(0) + P_1(-e)\right]/2e^2 \qquad A_2 = \left[P_2(+e) - 2P_2(0) + P_2(-e)\right]/2e^2$$

$$B_1 = \left[P_1(+e) - P_1(-e)\right]/2e \qquad B_2 = \left[P_2(+e) - P_2(-e)\right]/2e$$

$$C_1 = P_1(0) \qquad C_2 = P_2(0)$$

Substituting those coefficients in Eqs. (3.77) and (3.78), and integrating by parts, the following parabolic approximations are obtained:

$$D_{rs}^{(1)} = \frac{\Delta x_s}{8\pi} \left\{ \left[\left(\bar{y}^2 - \bar{z}^2\right) A_1 + \bar{y}B_1 + C_1\right] H + \left(\frac{1}{2}B_1 + \bar{y}A_1\right) \log\left[\frac{(\bar{y}-e)^2 + \bar{z}^2}{(\bar{y}+e)^2 + \bar{z}^2} \right] + 2eA_1 \right\} \tag{3.81}$$

$$\begin{aligned} D_{rs}^{(2)} = \frac{\Delta x_s}{16\pi\bar{z}^2} \Big\{ & \left[\left(\bar{y}^2 - \bar{z}^2\right) A_2 + \bar{y}B_2 + C_2\right] H \\ & + \frac{1}{(\bar{y}+e)^2 + \bar{z}^2} \left[\left[\left(\bar{y}^2 + \bar{z}^2\right)\bar{y} + \left(\bar{y}^2 - \bar{z}^2\right)e\right] A_2 + \left(\bar{y}^2 + \bar{z}^2 + \bar{y}e\right) B_2 + (\bar{y}+e)C_2 \right] \\ & - \frac{1}{(\bar{y}-e)^2 + \bar{z}^2} \left[\left[\left(\bar{y}^2 + \bar{z}^2\right)\bar{y} - \left(\bar{y}^2 - \bar{z}^2\right)e\right] A_2 + \left(\bar{y}^2 + \bar{z}^2 - \bar{y}e\right) B_2 + (\bar{y}-e)C_2 \right] \Big\} \end{aligned} \tag{3.82}$$

in which it remains to evaluate the integral:

$$H \equiv \int_{-e}^{+e} \frac{\mathrm{d}\bar{\eta}}{(\bar{y}-\bar{\eta})^2+\bar{z}^2} = \frac{1}{|\bar{z}|}\tan^{-1}\left[\frac{2e|\bar{z}|}{\bar{y}^2+\bar{z}^2-e^2}\right] \tag{3.83}$$

where the arctangent is taken in the intervale $[0,\pi]$.

3.1.6.2 Quartic Approximation of the Kernel Function

In the quartic approximation proposed by Rodden, Taylor and Jr (1998), a fourth degree polynomial is used for the interpolation of the doublets line at a quarter of the chord of each panel, changing the form of the integrands P1 and P2 of Eqs. (3.77) and (3.78).

This type of interpolation allows greater flexibility in the analysis for specific surfaces such as wings with high aspect ratio and swept wings, since the configuration of the mesh in this type of geometry tends to increase the aspect ratio of the panels, especially those located at the ends of the lifting surfaces. Rodden *et al.* (1999) report that in this situation the loss of accuracy of the method can be overcome by keeping the $\mathcal{AR}$ of the panels around three, which leads to a greater refinement in the aerodynamic mesh, making the method computationally expensive. It is also reported that the analysis for high values of reduced frequency requires that more divisions along the chord are needed in the discretization, also affecting the $\mathcal{AR}$ of the panels.

Along those lines, the mathematics involved in the derivation of the quartic approximation of the Kernel function is beyond the scope developed in this work. However, the reader can check more details in the work of Rodden, Taylor and Jr (1998). Nevertheless, in brief, the new integrands P_1 and P_2 in Eqs. (3.77) and (3.78) becomes:

$$P_1(\bar{\eta}) \equiv A_1\bar{\eta}^2 + B_1\bar{\eta} + C_1 + D_1\bar{\eta}^3 + E_1\bar{\eta}^4 \approx \left\{K_1 \exp\left[\frac{-i\omega\,(\bar{x}-\bar{\eta}\tan\Lambda_s)}{U_\infty}\right] - K_1^{(0)}\right\} T_1 \tag{3.84}$$

$$P_2(\bar{\eta}) \equiv A_2\bar{\eta}^2 + B_2\bar{\eta} + C_2 + D_2\bar{\eta}^3 + E_2\bar{\eta}^4 \approx \left\{K_2 \exp\left[\frac{-i\omega\,(\bar{x}-\bar{\eta}\tan\Lambda_s)}{U_\infty}\right] - K_2^{(0)}\right\} T_2^* \tag{3.85}$$

with

$$
\begin{aligned}
A_1 &= -\left[P_1(-e) - 16P_1(-e/2) + 30P_1(0) \; -16P_1(+e/2) + P_1(+e)\right]/6e^2 \\
B_1 &= \left[P_1(-e) - 8P_1(-e/2) \; +8P_1(+e/2) - P_1(+e)\right]/6e \\
C_1 &= P_1(0) \\
D_1 &= -\left[P_1(-e) - 2P_1(-e/2) \; +2P_1(+e/2) - P_1(+e)\right] / \left(3e^3/2\right) \\
E_1 &= \left[P_1(-e) - 4P_1(-e/2) + 6P_1(0) \; -4P_1(+e/2) + P_1(+e)\right] / \left(3e^4/2\right) \\
A_2 &= -\left[P_2(-e) - 16P_2(-e/2) + 30P_2(0) \; -16P_2(+e/2) + P_2(+e)\right]/6e^2 \\
B_2 &= P_2(-e) - 8P_2(-e/2) \; +8P_2(+e/2) - P_2(+e)\right]/6e \\
C_2 &= P_2(0) \\
D_2 &= -\left[P_2(-e) - 2P_2(-e/2) \; +2P_2(+e/2) - P_2(+e)\right] / \left(3e^3/2\right) \\
E_2 &= P_2(-e) - 4P_2(-e/2) + 6P_2(0) \; -4P_2(+e/2) + P_2(+e)\right] / \left(3e^4/2\right)
\end{aligned}
$$

Substituting the refined approximation into for $D_{rs}^{(1)}$ and $D_{rs}^{(2)}$ and integrating by parts:

$$
\begin{aligned}
D_{rs}^{(1)} = \frac{\Delta\xi_s}{8\pi} \Big\{ & \left[\left(\bar{y}^2 - \bar{z}^2\right) A_1 + \bar{y}B_1 + C_1 + \bar{y}\left(\bar{y}^2 - 3\bar{z}^2\right) D_1 + \left(\bar{y}^4 - 6\bar{y}^2\bar{z}^2 + \bar{z}^4\right) E_1\right] H \\
& + \left[\bar{y}A_1 + \frac{1}{2}B_1 + \frac{1}{2}\left(3\bar{y}^2 - \bar{z}^2\right) D_1 + 2\bar{y}\left(\bar{y}^2 - \bar{z}^2\right) E_1\right] \log\left[\frac{(\bar{y}-e)^2 + \bar{z}^2}{(\bar{y}+e)^2 + \bar{z}^2}\right] \\
& + 2e\left[A_1 + 2\bar{y}D_1 + \left(3\bar{y}^2 - \bar{z}^2 + \frac{1}{3}e^2\right) E_1\right]\Big\}
\end{aligned}
\tag{3.86}
$$

$$
\begin{aligned}
D_{rs}^{(2)} = & \frac{\Delta\xi_s}{16\pi\bar{z}^2} \Big\{ \left[\left(\bar{y}^2 + \bar{z}^2\right) A_2 + \bar{y}B_2 + C_2 + \bar{y}\left(\bar{y}^2 - 3\bar{z}^2\right) D_2 + \left(\bar{y}^4 + 6\bar{y}^2\bar{z}^2 - 3\bar{z}^4\right) E_2\right] H \\
& + \frac{1}{(\bar{y}+e)^2 + \bar{z}^2} \Big[\left[\left(\bar{y}^2 + \bar{z}^2\right)\bar{y} + \left(\bar{y}^2 - \bar{z}^2\right) e\right] A_2 + \left(\bar{y}^2 + \bar{z}^2 + \bar{y}e\right) B_2 + (\bar{y}+e) C_2 \\
& \quad + \left[\bar{y}^4 - \bar{z}^4 + \left(\bar{y}^2 - 3\bar{z}^2\right)\bar{y}e\right] D_2 + \left[\left(\bar{y}^4 - 2\bar{y}^2\bar{z}^2 - 3\bar{z}^4\right)\bar{y} + \left(\bar{y}^4 - 6\bar{y}^2\bar{z}^2 + \bar{z}^4\right) e\right] E_2\Big] \\
& - \frac{1}{(\bar{y}-e)^2 + \bar{z}^2} \Big[\left[\left(\bar{y}^2 + \bar{z}^2\right)\bar{y} - \left(\bar{y}^2 - \bar{z}^2\right) e\right] A_2 + \left(\bar{y}^2 + \bar{z}^2 - \bar{y}e\right) B_2 + (\bar{y}-e) C_2 \\
& \quad + \left[\bar{y}^4 - \bar{z}^4 - \left(\bar{y}^2 - 3\bar{z}^2\right)\bar{y}e\right] D_2 + \left[\left(\bar{y}^4 - 2\bar{y}^2\bar{z}^2 - 3\bar{z}^4\right)\bar{y} - \left(\bar{y}^4 - 6\bar{y}^2\bar{z}^2 + \bar{z}^4\right) e\right] E_2\Big] \\
& + \bar{z}^2 \log\left[\frac{(\bar{y}-e)^2 + \bar{z}^2}{(\bar{y}+e)^2 + \bar{z}^2}\right] D_2 + 4\bar{z}^2\left[e + \bar{y}\log\left[\frac{(\bar{y}-e)^2 + \bar{z}^2}{(\bar{y}+e)^2 + \bar{z}^2}\right]\right] E_2\Big\}
\end{aligned}
\tag{3.87}
$$

3.1.7 Aerodynamic Coefficients

The non-dimensional lift coefficient may be calculated for an individual strip of panel using the following:

$$c_L(y) = \frac{\int_{x_{LE}(y)}^{x_{\mathrm{TE}}(y)} \Delta\bar{c}_p \, \mathrm{d}x}{\pi c(y)} \approx \frac{\sum_j \Delta\bar{c}_{p,j} \Delta x_j}{\pi c(y)} \tag{3.88}$$

where $\Delta\bar{c}_{p,j}$ the pressure coefficient at panel $j, \Delta x_j$ is the mid-span chord of panel j, and $c(y) = x_{\mathrm{TE}}(y) - x_{\mathrm{LE}}(y)$ is the mid-span chord of the strip. Here, $x_{\mathrm{LE}}(y)$ and $x_{\mathrm{TE}}(y)$ are the x-coordinates of the leading and trailing edges at mid-span of the strip, respectively.

By extending the integration to the entire wing, the expression for the lit coefficient of the wing is given by:

$$C_L = \frac{\iint_A \Delta\bar{c}_p \, \mathrm{d}A}{\pi A_{\mathrm{ref}}} \approx \frac{\sum_j \Delta\bar{c}_{p,j} A_j}{\pi A_{\mathrm{ref}}} \tag{3.89}$$

where A_j is the panel surface area, and A_{ref} is the reference area, typically the surface area of the wing.

In addition, Eq. (3.67) can be rewritten in terms of $\Delta\bar{c}_p$:

$$\left\{\Delta\bar{c}_p\right\} = \underbrace{[{D_{rs}}^{-1}]}_{[AIC]}\{\bar{w}\} \tag{3.90}$$

Thus, the vector containing the lift forces over each panel can be calculated as:

$$\{\bar{L}\} = q_d[S_L]\left\{\Delta\bar{c}_p\right\} = q_d[S_L][AIC]\{\bar{w}\} \tag{3.91}$$

where $[S_L]$ is a diagonal matrix with the areas of each panel in which the surfaces were discretized.

3.2 DLM Verification

The Doublet-Lattice Method (DLM) has been applied by academic researchers and industry to certificate aircraft (VALENTE *et al.*, 2017). Therefore, to make sure the implementation in this work is working properly, some verification cases have been addressed.

3.2.1 Verification of the Kernel Function

Before performing any other complete wing configuration, it is important to certify that the computation of the Kernel function is right. Thus, it is convenient to evaluate the function

along only one panel, i.e., considering receiving panel r and emitting panel s as one and the same panel. Rodden, Taylor and McIntosh (1996) have calculated the variation of the planar component of the Kernel numerator along the quarter-chord line of the emitting panel, for multiple values of the panel aspect ratio ($\mathcal{AR}$), in order to determine its influence on the accuracy of the method. It has been shown that a quartic approximation allows the relaxation of the aspect ratio of the panels, without increasing the number of panels needed in the discretization.

In this verification, the panel chord is fixed at $c = 1.0$ units, and the panel span is increased to vary the panel aspect ratio from $\mathcal{AR} = 1$ to 5. The problem is made non-dimensional using the panel half-chord as reference length, $L_{\text{ref}} = 0.5$ units. Operating conditions used for this test case are summarized in Table 2.

Table 2 – Operating conditions for the test case.

Property	Value
Mach number, M_∞	0.8
Reduced frequency, k	1.0
Reference length, L_{ref}	0.5 units

Source: Rodden, Taylor and McIntosh (1996).

The results obtained for $\mathcal{AR} = 1$, 2 and 5 are depicted in Fig. 14. When compared to the values reported in the original paper, an exact correspondence is observed. Even though the imaginary component is not presented in the work of Rodden, Taylor and McIntosh (1996), this work brings it up in order to illustrate the differences between the parabolic and quartic approximation.

3.2.2 Planar Wings

The comparisons will be made with results from different methods presented by Blair (1994), for two different wing geometries: rectangular and swept.

In the first case, i.e., for the rectangular wing, the basic geometry has a aspect ratio of 2 and a wingspan of 24 units of length. Different discretizations will be evaluated. The discretization of 50 panel, 5 in chord-direction and 10 along the wingspan, is depicted in Fig. 15.

The Mach number is 0.5 and the reference length b for the dimensionless frequency is the

Figure 14 – Variation of the incremental planar kernel numerator along the doublet line of the panel. The results in (a), (d) and (g) are from Rodden, Taylor and McIntosh (1996).

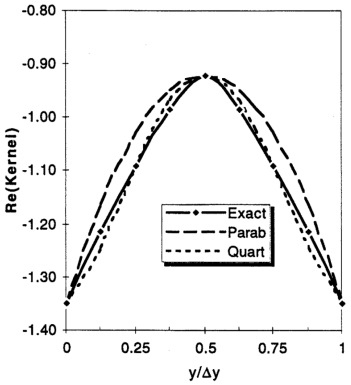

(a) Real part for $\mathcal{AR} = 1$.

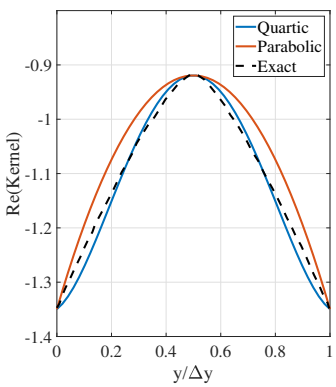

(b) Real part for $\mathcal{AR} = 1$.

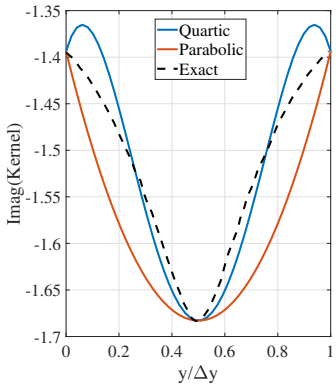

(c) Imaginary part for $\mathcal{AR} = 1$.

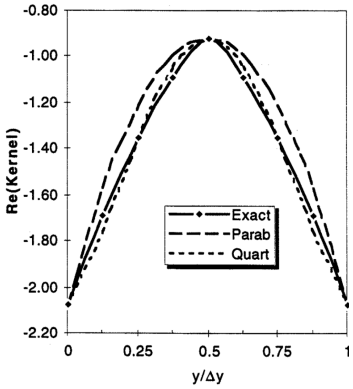

(d) Real part for $\mathcal{AR} = 2$.

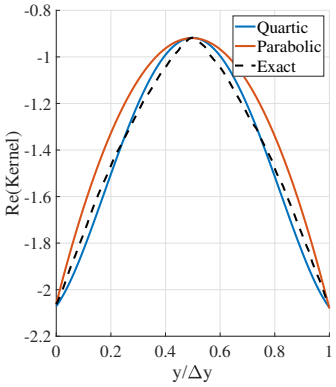

(e) Real part for $\mathcal{AR} = 2$.

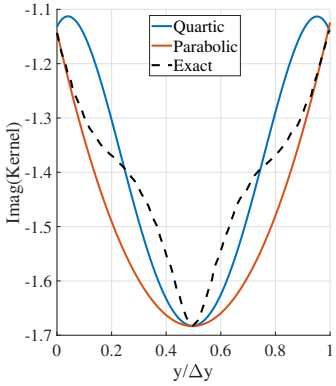

(f) Imaginary part for $\mathcal{AR} = 2$.

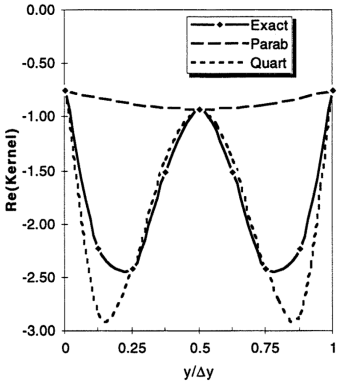

(g) Real part for $\mathcal{AR} = 5$.

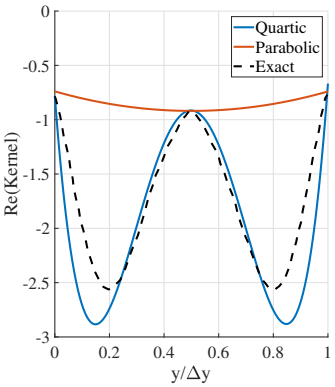

(h) Real part for $\mathcal{AR} = 5$.

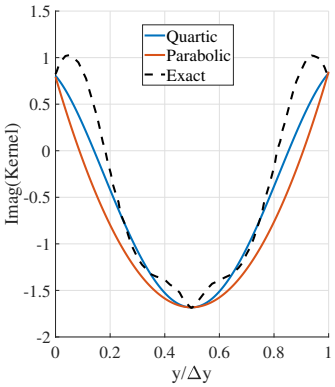

(i) Imaginary part for $\mathcal{AR} = 5$.

Source: Elaborated by the author.

semi-chord. Two cases of reduced frequency are evaluated: 0 and 1.4. The boundary condition is given by:

$$\hat{\bar{w}}_j = ik\frac{\hat{h}_j}{b} + \frac{\partial \hat{h}_j}{\partial x} \tag{3.92}$$

Figure 15 – Wing discretization with 50 panels.

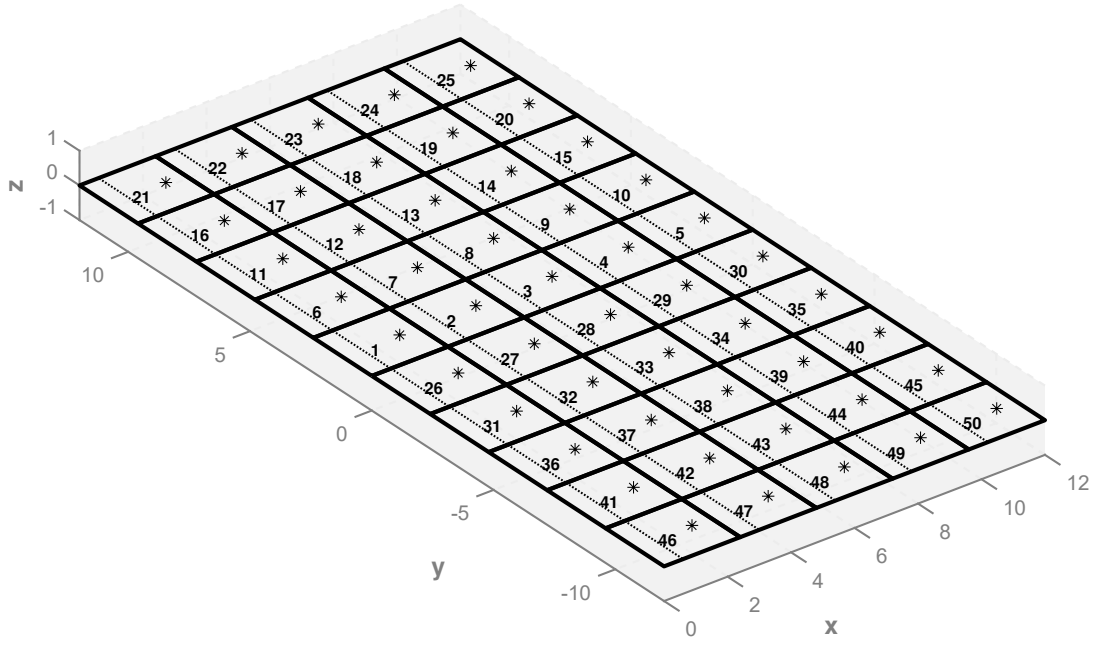

Source: Elaborated by the author.

with $h = h(x,y,t)$ given by the following harmonic motion in time:

$$h = (-x)e^{i\omega t}$$
$$\hat{h} = -x \tag{3.93}$$

In the steady case ($k = 0$), the boundary condition corresponds to the calculation of the slope of the lift coefficient curve per radian of angle of attack. In the unsteady case, the wing will be pitching around the leading edge ($x = 0$) at a frequency $k = 1.4$. The lift coefficient results obtained by the this work are compared with those provided by Blair (1994) in Table 3.

The results in Table 3 show coherence when compared to the other results presented by Blair (1994). In addition, they match the scripts H7WC (mainly for reduced frequency of 1.4) and LATIS (mainly for zero frequency), which have steady-state correction, likewise this work, a correction that the others do not use.

The second case of verification is applied for a swept wing. The implementation of this work will also be compared to the same previous scripts, but with a different plan shape wing, with sweep and taper ratio. The wing selected here is the AGARD wing model. The discretization have 50 panels, 5 along the chord and 10 along the wingspan, as illustrated in Fig. 16. The

Table 3 – Results for rectangular wing obtained in this work compared to other results presented by Blair (1994).

Discretization	Script	k=0	k = 1.4	
		C_L (real)	C_L: Magnitude	Phase angle (^{o})
5×5	WL-TR-95-3022	2.8322	10.337	93.5661
	WL-TR-92-3028	2.8322	10.337	93.5661
	H7WC	2.803	9.96	93.83
	LATIS	2.8040	9.956	93.8338
	This work	**2.804**	**9.953**	**93.87**
10×10	WL-TR-95-3022	2.7147	10.654	91.0658
	WL-TR-92-3028	2.7147	10.654	91.0658
	H7WC	2.698	10.39	91.27
	LATIS	2.6994	10.258	91.4137
	This work	**2.699**	**10.38**	**91.26**
15×15	WL-TR-95-3022	2.6475	10.753	90.4543
	WL-TR-92-3028	2.6475	10.753	90.4543
	H7WC	-	10.55	90.57
	LATIS	2.6637	10.307	91.9003
	This work	**2.664**	**10.55**	**90.59**
20×20	WL-TR-95-3022	2.6542	10.795	90.2333
	WL-TR-92-3028	-	-	-
	H7WC	2.642	10.62	90.27
	LATIS	-	-	-
	This work	**2.646**	**10.63**	**90.33**

positions of the control points are also shown.

A Mach number of 0.8 is considered. Also, the boundary conditions applied are the same ones to the previous case, i.e., they are presented in Eqs. (3.92) and (3.93). The results obtained for zero reduced frequency are displayed in Table 4.

The results obtained by the presented implementation of the DLM code are in very good agreement with those reported by Blair (1994).

Figure 16 – AGARD wing discretization with 50 panels.

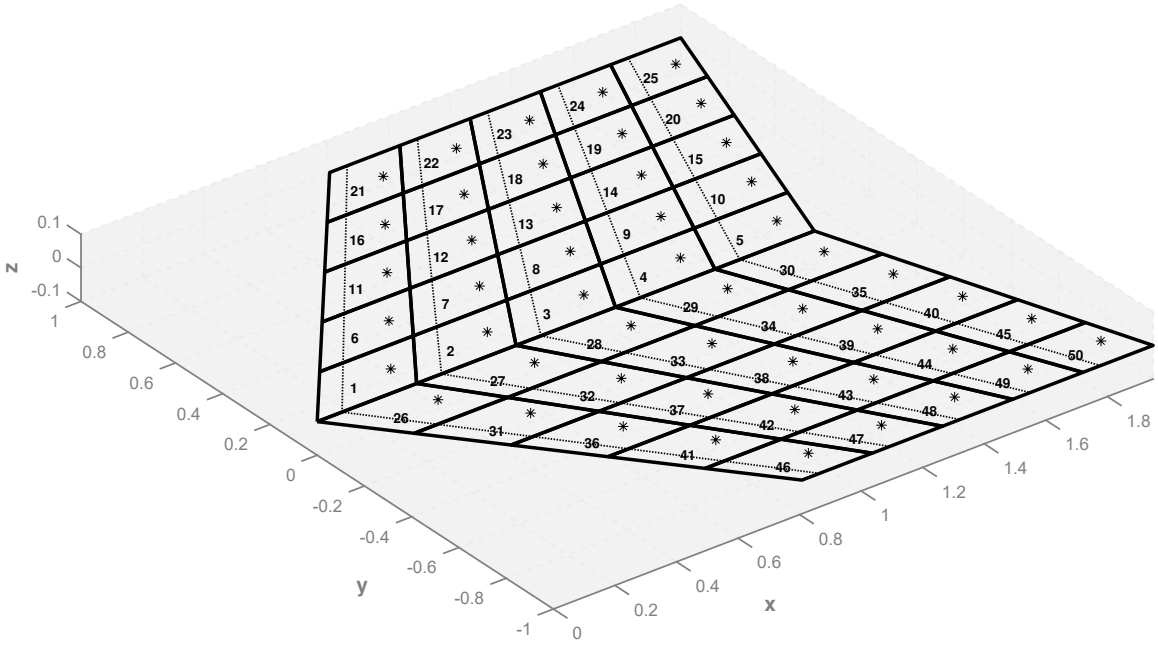

Source: Elaborated by the author.

Table 4 – Results for AGARD wing obtained in this work compared to other results presented by Blair (1994).

Discretization	Script	k=0 C_L (real)
5×5	WL-TR-95-3022	2.3192
	WL-TR-92-3028	2.3149
	H7WC	2.32
	LATIS	2.3259
	This work	**2.326**
10×10	WL-TR-95-3022	2.2296
	WL-TR-92-3028	2.2277
	H7WC	2.23
	LATIS	2.2330
	This work	**2.233**
15×15	WL-TR-95-3022	2.1995
	WL-TR-92-3028	2.1982
	H7WC	2.20
	LATIS	2.2017
	This work	**2.202**
20×20	WL-TR-95-3022	2.1843
	WL-TR-92-3028	-
	H7WC	2.18
	LATIS	-
	This work	**2.187**

CHAPTER

4

STRUCTURAL MODELING

In the following chapter, it is presented the structural modeling used to describe the wing structure under analysis in this work. Next, a verification of the implementation is performed, comparing the results with Nastran analysis.

The formulation presented in this chapter is already implemented in Python and available as a library named `pyfe3d`, which has been developed by Castro (2022a). Therefore, the mass and stiffness matrix of the wing structure under analysis are obtained by using that library package.

The wing design proposed in Chapter 6 shows that the structure is basically made of truss-based elements and plate elements, and they are connected by ball joints at nodes. Therefore, the structural model is based on two finite element types to correctly represent the different wing structural designs: quadrilateral and beam elements, whose formulations are presented in the following sections.

4.1 Homogeneous Euler-Lagrangian equations governing 3D Timoshenko beam

The truss-based elements are represented using an efficient three-dimensional (3D) Timoshenko beam element, with the formulation proposed by Luo (LUO, 2008) and adapted by Castro (2022b).

Consider a three-dimensional 2-node beam element as illustrated in Fig. 17. The element has two nodes, and each node has six degrees of freedom (DOF): three translation and three rotations. In this case, there is no external force acting on the beam in between the two nodes.

Figure 17 – A 3D 2-node beam element with local coordinate system centered on the neutral line.

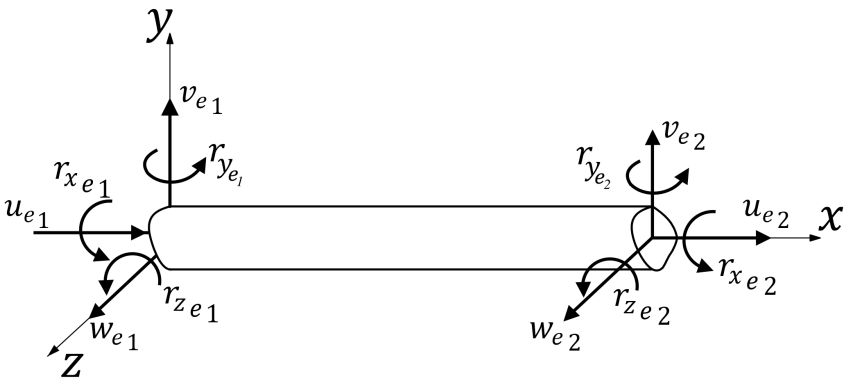

Source: Castro (2022b).

The motion of a typical particle p in the beam ban be split into two parts as depicted in Fig. 18. The translation of point c at the beam axis and the rotation of vector $\boldsymbol{t}$ defined by p and c. Vectors $\boldsymbol{t}$ and $\boldsymbol{r_c}$ are orthogonal to each other in the underformed configuration. The motion of point c is described by three translations u_c, v_c, and w_c along the three axis, respectively.

Figure 18 – Kinematics of a typical particle in a 3D beam.

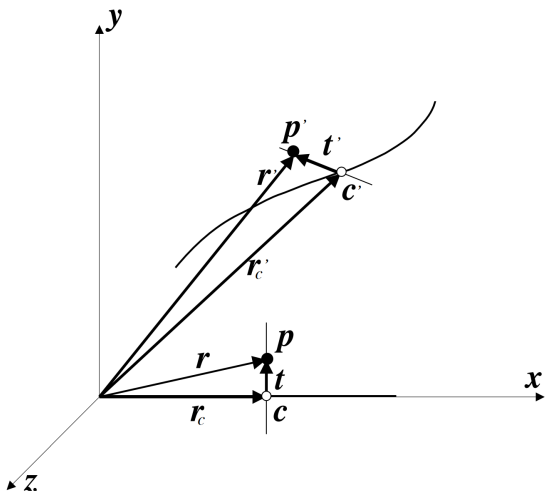

Source: Luo (2008).

According to Euler-Chasles' theorem, the rotation of vector t can be realized by a rotational operator $\boldsymbol{R}$ (NOUR-OMID; RANKIN, 1991; PACOSTE; ERIKSSON, 1997):

$$\boldsymbol{t}' = \boldsymbol{R}\boldsymbol{t} \tag{4.1}$$

where

$$\boldsymbol{R} = \exp\left(\tilde{\boldsymbol{\Psi}}\right) = \boldsymbol{I}_3 + \tilde{\boldsymbol{\Psi}} + \frac{1}{2}\tilde{\boldsymbol{\Psi}}^2 + \cdots \tag{4.2}$$

$$\tilde{\boldsymbol{\Psi}} = \begin{bmatrix} 0 & -r_{z_c} & r_{y_c} \\ r_{z_c} & 0 & -r_{x_c} \\ -r_{y_c} & r_{x_c} & 0 \end{bmatrix} \tag{4.3}$$

and r_{x_c}, r_{y_c} and r_{z_c} are the rotational angles of vector $\boldsymbol{t}$ around the three axes x, y and z, respectively.

The position vectors of particle p before and after deformation are, respectively,

$$\begin{aligned} \boldsymbol{r} &= \boldsymbol{r}_c + \boldsymbol{t} \\ \boldsymbol{r}' &= \boldsymbol{r}'_c + \boldsymbol{t}' = \boldsymbol{r}'_c + \boldsymbol{R}\boldsymbol{t} \end{aligned} \tag{4.4}$$

So the displacement vector of p is

$$\boldsymbol{u} = \boldsymbol{r}' - \boldsymbol{r} = \boldsymbol{u}_c + (\boldsymbol{R} - \boldsymbol{I}_3)\boldsymbol{t} \tag{4.5}$$

where $\boldsymbol{I}_3$ is a 3×3 unit matrix; $\boldsymbol{u} = \begin{bmatrix} u_e & v_e & w_e \end{bmatrix}^T$ and $\boldsymbol{u}_c = \begin{bmatrix} u_c & v_c & w_c \end{bmatrix}^T$

Considering that the rotation angles r_{x_c}, r_{y_c} and r_{z_c} are small and only the first two terms are retained in Taylor series in Eq. (4.2), the displacements of particle p in Eq. (4.5) can be written as:

$$\begin{cases} u_e = u_c - r_{z_c} y + r_{y_c} z \\ v_e = v_c - r_{x_c} z \\ w_e = w_c + r_{x_c} y \end{cases} \tag{4.6}$$

Furthermore, assuming that the strains are smalls so that a linear strain-displacement relation can be adopted, the three strains for a 3D beam may be expressed as:

$$\begin{cases} \varepsilon_{xx} = \dfrac{\partial u_e}{\partial x} = u'_c - r'_{z_c} y + r'_{y_c} z \\ \gamma_{xy} = \dfrac{\partial v_e}{\partial x} + \dfrac{\partial u_e}{\partial y} = v'_c - r'_{x_c} z - r_{z_c} \\ \gamma_{xz} = \dfrac{\partial w_e}{\partial x} + \dfrac{\partial u_e}{\partial z} = w'_c + r'_{x_c} y + r_{y_c} \end{cases} \tag{4.7}$$

where $(\quad)' = \dfrac{d}{dx}$.

4.2 3D Truss Element

Having Eqs. (4.6) and (4.7), they can be rewritten considering only the the displacements and rotations along the x-direction, which is what matters the most for truss elements:

$$\begin{cases} u_e(x,y,z) = u_c(x) \\ v_e(x,y,z) = -r_{x_c}(x)z \\ w_e(x,y,z) = +r_{x_c}(x)y \end{cases} \tag{4.8}$$

$$\begin{cases} \varepsilon_{xx} = \dfrac{\partial u_e}{\partial x} = \dfrac{\partial u_c}{\partial x} \\ \gamma_{xy} = \dfrac{\partial v_e}{\partial x} + \dfrac{\partial u_e}{\partial y} = -z\dfrac{\partial r_{x_c}}{\partial x} \\ \gamma_{xz} = \dfrac{\partial w_e}{\partial x} + \dfrac{\partial u_e}{\partial z} = y\dfrac{\partial r_{x_c}}{\partial x} \end{cases} \tag{4.9}$$

The normal stress and shear stress are then described as:

$$\begin{cases} \sigma_{xx} = E\varepsilon_{xx} \\ \tau_{xy} = kG\gamma_{xy} \\ \tau_{xz} = kG\gamma_{xz} \end{cases} \tag{4.10}$$

where E is the Young's modulus, G is the shear modulus, and k is the shear correction factor.

4.2.1 Interpolation Function

Of all the quadrature formulae, the Gauss-Legendre one is the most commonly used. The details of the method is shortly discussed here. The formula requires the integral to be cast as one to be evaluated over the interval $[-1,1]$. This requires the transformation of the problem coordinate x to a natural coordinate ξ, as depicted in Fig. 19).

Figure 19 – Global coordinate x, local coordinate $\bar{x}$, and normalized coordinate ξ.

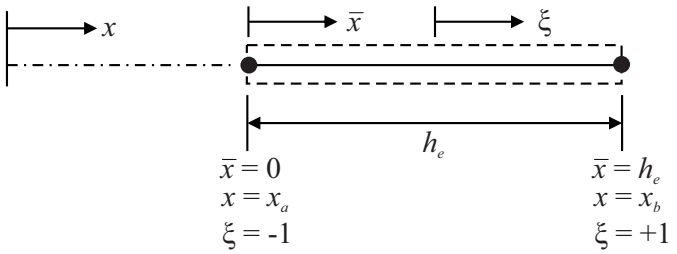

Source: Elaborated by the author.

Thus,

$$\text{when} \quad x = x_a, \quad \xi = -1; \quad \text{when} \quad x = x_b, \quad \xi = 1$$

The transformation between x and ξ can be represented by the linear transformation:

$$x(\xi) = x_a + \frac{1}{2} h_e (1+\xi) \tag{4.11}$$

where x_a denotes the global coordinate of the left-end node of the element Ω_e and h_e is the element length (see Fig.19).

The local coordinate ξ is called the *normal coordinate* or *natural coordinate*, and its values always lie between -1 and 1 , with its origin at the center of the element. The local coordinate ξ is useful in two ways: it is (a) convenient in constructing the interpolation functions and (b) required in numerical integration using Gauss-Legendre quadrature.

The derivation of the Lagrange family of interpolation functions in terms of the natural coordinate ξ is made easy by the following interpolation property of the approximation functions:

$$\psi_i\left(\xi_j\right) = \begin{cases} 1 & \text{if } i = j \\ 0 & \text{if } i \neq j \end{cases} \tag{4.12}$$

where ξ_j is the ξ coordinate of the j-th node in the element. For an element with n nodes, $\psi_i (i = 1,2,\ldots,n)$ are polynomials of degree $n-1$. To construct ψ_i satisfying Eq. (4.12), the procedure is as follows: for each ψ_i, we form the product of $n-1$ linear functions $\xi - \xi_j (j = 1,2,\ldots,i-1,i+1,\ldots,n; j \neq i)$:

$$\psi_i = c_i (\xi - \xi_1)(\xi - \xi_2)\cdots(\xi - \xi_{i-1})(\xi - \xi_{i+1})\cdots(\xi - \xi_n) \tag{4.13}$$

Note that ψ_i is zero at all nodes except the i-th. Next, we determine the constant c_i such that $\psi_i = 1$ at $\xi = \xi_i$:

$$c_i = [(\xi_i - \xi_1)(\xi_i - \xi_2)\cdots(\xi_i - \xi_{i-1})(\xi_i - \xi_{i+1})\cdots(\xi_i - \xi_n)]^{-1} \tag{4.14}$$

Thus, the interpolation function associated with node i is

$$\psi_i(\xi) = \frac{(\xi - \xi_1)(\xi - \xi_2)\cdots(\xi - \xi_{i-1})(\xi - \xi_{i+1})\cdots(\xi - \xi_n)}{(\xi_i - \xi_1)(\xi_i - \xi_2)\cdots(\xi_i - \xi_{i-1})(\xi_i - \xi_{i+1})\cdots(\xi_i - \xi_n)} \tag{4.15}$$

The linear, quadratic, and cubic Lagrange interpolation functions in terms of the natural coordinate (for equally spaced nodes) are defined as:

- Linear:

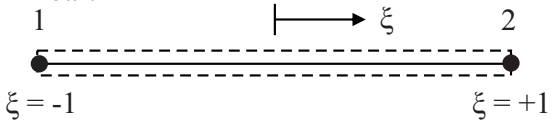

$$\psi_1(\xi) = \frac{1}{2}(1-\xi), \quad \psi_2(\xi) = \frac{1}{2}(1+\xi)$$

- Quadratic:

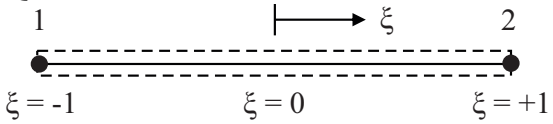

$$\psi_1(\xi) = -\frac{1}{2}\xi(1-\xi), \quad \psi_2(\xi) = \left(1-\xi^2\right)$$
$$\psi_3(\xi) = \frac{1}{2}\xi(1+\xi)$$

- Cubic:

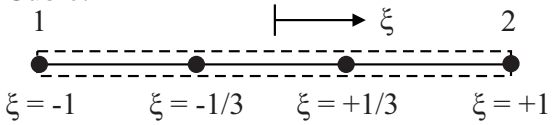

$$\psi_1(\xi) = -\frac{9}{16}(1-\xi)\left(\frac{1}{9}-\xi^2\right), \psi_2(\xi) = \frac{27}{16}\left(1-\xi^2\right)\left(\frac{1}{3}-\xi\right)$$
$$\psi_3(\xi) = \frac{27}{16}\left(1-\xi^2\right)\left(\frac{1}{3}+\xi\right), \psi_4(\xi) = -\frac{9}{16}(1+\xi)\left(\frac{1}{9}-\xi^2\right)$$

For this work, it is assumed a linear interpolation function. From now on, for convenience, the shape function symbol ψ is replaced by N:

$$\begin{cases} N_1 = \dfrac{(1-\xi)}{2} \\ N_2 = \dfrac{(1+\xi)}{2} \end{cases} \tag{4.16}$$

Having those interpolation function, the displacements and rotations can be rewritten as:

$$\begin{cases} u_c(\xi) = N_1 u_{e_1} + N_2 u_{e_2} \\ r_{x_c}(\xi) = N_1 r_{x_{e_1}} + N_2 r_{x_{e_2}} \end{cases} \tag{4.17}$$

Consequently, the strains ε_{xx}, γ_{xy} and γ_{xz} can also be rewritten in terms of the interpolation functions:

$$\begin{cases} \varepsilon_{xx} = \dfrac{\partial u_c}{\partial x} = \dfrac{\partial N_1}{\partial x} u_{e_1} + \dfrac{\partial N_2}{\partial x} u_{e_2} = N_{1,x} u_{e_1} + N_{2,x} u_{e_2} \\ \gamma_{xy} = -z\dfrac{\partial r_{x_c}}{\partial x} = -z\left(\dfrac{\partial N_1}{\partial x} r_{x_{e_1}} + \dfrac{\partial N_2}{\partial x} r_{x_{e_2}}\right) = -z\left(N_{1,x} r_{x_{e_1}} + N_{2,x} r_{x_{e_2}}\right) \\ \gamma_{xz} = y\dfrac{\partial r_{x_C}}{\partial x} = y\left(\dfrac{\partial N_1}{\partial x} r_{x_1} + \dfrac{\partial N_2}{\partial x} r_{x_{e_2}}\right) = y\left(N_{1,x} r_{x_{e_1}} + N_{2,x} r_{x_{e_2}}\right) \end{cases} \tag{4.18}$$

Applying the chain rule, the derivation in x can be replaced by:

$$\frac{\partial}{\partial x} = \frac{\partial}{\partial \xi}\frac{\partial \xi}{\partial x} = \frac{2}{\ell_e}\frac{\partial}{\partial \xi}$$

Therefore, strains ε_{xx}, γ_{xy} and γ_{xz} become:

$$\begin{cases} \varepsilon_{xx} = \dfrac{2}{\ell_e}\dfrac{\partial N_1}{\partial \xi}u_{e_1} + \dfrac{2}{\ell_e}\dfrac{\partial N_2}{\partial \xi}u_{e_2} \\ \gamma_{xy} = -z\left(\dfrac{2}{\ell_e}\dfrac{\partial N_1}{\partial \xi}r_{x_{e_1}} + \dfrac{2}{\ell_e}\dfrac{\partial N_2}{\partial \xi}r_{x_2}\right) \\ \gamma_{xz} = y\left(\dfrac{2}{\ell_e}\dfrac{\partial N_1}{\partial \xi}r_{x_{e_1}} + \dfrac{2}{\ell_e}\dfrac{\partial N_2}{\partial \xi}r_{x_{e_2}}\right) \end{cases} \tag{4.19}$$

The displacements of the nodes may be expressed in the matrix form:

$$u_e(x,y,z) = u_c(x) = N_1 u_{e_1} + N_2 u_{e_2} \tag{4.20}$$

$$\begin{Bmatrix} u_e \\ v_e \\ w_e \\ r_{x_e} \\ r_{y_e} \\ r_{z_e} \end{Bmatrix} = \begin{bmatrix} N_1 & 0 & 0 & 0 & 0 & 0 & N_2 & 0 & 0 & 0 & 0 & 0 \\ 0 & 0 & 0 & 0 & 0 & 0 & 0 & 0 & 0 & 0 & 0 & 0 \\ 0 & 0 & 0 & 0 & 0 & 0 & 0 & 0 & 0 & 0 & 0 & 0 \\ 0 & 0 & 0 & 0 & 0 & 0 & 0 & 0 & 0 & 0 & 0 & 0 \\ 0 & 0 & 0 & 0 & 0 & 0 & 0 & 0 & 0 & 0 & 0 & 0 \\ 0 & 0 & 0 & 0 & 0 & 0 & 0 & 0 & 0 & 0 & 0 & 0 \end{bmatrix} \begin{Bmatrix} u_{e_1} \\ v_{e_1} \\ w_{e_1} \\ r_{x_{e_1}} \\ r_{y_{e_1}} \\ r_{z_{e_1}} \\ u_{e_2} \\ v_{e_2} \\ w_{e_2} \\ r_{x_{e_2}} \\ r_{y_{e_2}} \\ r_{z_e} \end{Bmatrix} \tag{4.21}$$

$$\boldsymbol{u_e} = \boldsymbol{N}\bar{\boldsymbol{u}}_{\boldsymbol{e}} \tag{4.22}$$

The strains can also be put together in the matrix form, which is convenient to separate in axial and rotational terms, such as:

$$\begin{Bmatrix} \varepsilon_{xx} \\ \gamma_{xy} \\ \gamma_{xz} \end{Bmatrix} = \begin{bmatrix} N_{1,x} & 0 & 0 & 0 & 0 & 0 & N_{2,x} & 0 & 0 & 0 & 0 & 0 \\ 0 & 0 & 0 & -zN_{1,x} & 0 & 0 & 0 & 0 & 0 & -zN_{2,x} & 0 & 0 \\ 0 & 0 & 0 & yN_{1,x} & 0 & 0 & 0 & 0 & 0 & yN_{2,x} & 0 & 0 \end{bmatrix} \bar{\boldsymbol{u}}_e \tag{4.23}$$

$$\boldsymbol{\varepsilon} = \boldsymbol{B}\bar{\boldsymbol{u}}_{\boldsymbol{e}} \tag{4.24}$$

Evaluating the strains in x, y and z directions, the following relations are obtained:

$$\begin{Bmatrix} \varepsilon_{xx} \\ \gamma_{xy} \\ \gamma_{xz} \end{Bmatrix} = \begin{Bmatrix} \varepsilon_{xx_0} \\ \gamma_{xy_0} \\ \gamma_{xz_0} \end{Bmatrix} + y \begin{Bmatrix} \varepsilon_{xx_y} \\ \gamma_{xy_y} \\ \gamma_{xz_y} \end{Bmatrix} + z \begin{Bmatrix} \varepsilon_{xx_z} \\ \gamma_{xy_z} \\ \gamma_{xz_z} \end{Bmatrix} \tag{4.25}$$

$$\boldsymbol{\varepsilon} = \boldsymbol{\varepsilon_0} + y\boldsymbol{\varepsilon_y} + z\boldsymbol{\varepsilon_z} \tag{4.26}$$

$$\begin{Bmatrix} \varepsilon_{xx_0} \\ \gamma_{xy_0} \\ \gamma_{xz_0} \end{Bmatrix} = \begin{bmatrix} N_{1,x} & 0 & 0 & 0 & 0 & 0 & N_{2,x} & 0 & 0 & 0 & 0 & 0 \\ 0 & 0 & 0 & 0 & 0 & 0 & 0 & 0 & 0 & 0 & 0 & 0 \\ 0 & 0 & 0 & 0 & 0 & 0 & 0 & 0 & 0 & 0 & 0 & 0 \end{bmatrix} \bar{\boldsymbol{u}}_{\boldsymbol{e}} \tag{4.27}$$

$$\boldsymbol{\varepsilon_0} = \boldsymbol{B_0}\bar{\boldsymbol{u}}_{\boldsymbol{e}} \tag{4.28}$$

$$\begin{Bmatrix} \varepsilon_{xxy} \\ \gamma_{xy_y} \\ \gamma_{xzy} \end{Bmatrix} = \begin{bmatrix} 0 & 0 & 0 & 0 & 0 & 0 & 0 & 0 & 0 & 0 & 0 & 0 \\ 0 & 0 & 0 & 0 & 0 & 0 & 0 & 0 & 0 & 0 & 0 & 0 \\ 0 & 0 & 0 & N_{1,x} & 0 & 0 & 0 & 0 & 0 & N_{2,x} & 0 & 0 \end{bmatrix} \bar{\boldsymbol{u}}_{\boldsymbol{e}} \tag{4.29}$$

$$\boldsymbol{\varepsilon_y} = \boldsymbol{B_y}\bar{\boldsymbol{u}}_{\boldsymbol{e}} \tag{4.30}$$

$$\begin{Bmatrix} \varepsilon_{xx_Z} \\ \gamma_{xy_z} \\ \gamma_{xz_z} \end{Bmatrix} = \begin{bmatrix} 0 & 0 & 0 & 0 & 0 & 0 & 0 & 0 & 0 & 0 & 0 & 0 \\ 0 & 0 & 0 & -N_{1,x} & 0 & 0 & 0 & 0 & 0 & -N_{2,x} & 0 & 0 \\ 0 & 0 & 0 & 0 & 0 & 0 & 0 & 0 & 0 & 0 & 0 & 0 \end{bmatrix} \bar{\boldsymbol{u}}_{\boldsymbol{e}} \tag{4.31}$$

$$\boldsymbol{\varepsilon_z} = \boldsymbol{B_z}\bar{\boldsymbol{u}}_{\boldsymbol{e}} \tag{4.32}$$

Following, in general form, it becomes:

$$\boldsymbol{B} = \boldsymbol{B_0} + y\boldsymbol{B_y} + z\boldsymbol{B}_z \tag{4.33}$$

The normal and shear stress can also be rewritten in the matrix form, such as:

$$\boldsymbol{\sigma} = \begin{Bmatrix} \sigma_{xx} \\ \tau_{xy} \\ \tau_{xz} \end{Bmatrix} = \begin{bmatrix} E & 0 & 0 \\ 0 & kG & 0 \\ 0 & 0 & kG \end{bmatrix} \begin{Bmatrix} \varepsilon_{xx} \\ \gamma_{xy} \\ \gamma_{xz} \end{Bmatrix} \tag{4.34}$$

$$\boldsymbol{\sigma} = \boldsymbol{C\varepsilon} \tag{4.35}$$

4.2.2 Stiffness and Mass Matrices

The virtual strain energy for a body is calculated by

$$\delta V = \underbrace{\int_{\Omega} \boldsymbol{\sigma}^{\boldsymbol{T}} \delta \boldsymbol{\varepsilon} d\Omega}_{\text{strain energy}} \underbrace{- \int_{\Omega} \left(\boldsymbol{b}^{\boldsymbol{T}} \delta \boldsymbol{u} \right) d\Omega - \int_{\delta\Omega} \left(\overline{\boldsymbol{\sigma}}^{\boldsymbol{T}} \delta \boldsymbol{u} \right) d(\delta\Omega)}_{\text{work by external forces}} = 0 \tag{4.36}$$

The strain energy component for the truss element becomes:

$$\delta U = \int_{\Omega} \boldsymbol{\sigma}^{\boldsymbol{T}} \delta \boldsymbol{\varepsilon} d\Omega = \delta \sum_{e} U_e = \int_{\Omega_e} \boldsymbol{\sigma}^{\boldsymbol{T}} \delta \boldsymbol{\varepsilon} d\Omega_{\mathrm{e}} \tag{4.37}$$

Applying Eqs. (4.35), (4.24) and (4.33), Eq. (4.37) turns into:

$$\delta U_e = \overline{\boldsymbol{u}}_{\boldsymbol{e}}^{\top} \int_{\Omega_{\mathrm{e}}} \left(\boldsymbol{B_0} + y\boldsymbol{B_y} + z\boldsymbol{B}_z \right)^{\top} \boldsymbol{C} \left(\boldsymbol{B_0} + y\boldsymbol{B_y} + z\boldsymbol{B}_z \right) d\Omega_e \delta \overline{\boldsymbol{u}}_{\boldsymbol{e}} \tag{4.38}$$

Therefore, the constitutive stiffness matrix can be calculated and expressed by:

$$\boldsymbol{K_e} = \int_{\Omega} \left(\boldsymbol{B_0} + y\boldsymbol{B_y} + z\boldsymbol{B}_z \right)^{\top} \boldsymbol{C} \left(\boldsymbol{B_0} + y\boldsymbol{B_y} + z\boldsymbol{B}_z \right) d\Omega \tag{4.39}$$

$$\boldsymbol{K_e} = \iiint_{x,y,z} \left(\boldsymbol{B_0} + y\boldsymbol{B_y} + z\boldsymbol{B}_z \right)^{\top} \boldsymbol{C} \left(\boldsymbol{B_0} + y\boldsymbol{B_y} + z\boldsymbol{B}_z \right) dxdydz \tag{4.40}$$

$$\begin{aligned} \boldsymbol{K_e} = \iiint_{x,y,z} \Big(& \boldsymbol{B_0}^{\top} \boldsymbol{C} \boldsymbol{B_0} + y\boldsymbol{B_0}^{\top} \boldsymbol{C} \boldsymbol{B_y} + z\boldsymbol{B_0}^{\top} \boldsymbol{C} \boldsymbol{B}_z \\ & y\boldsymbol{B}_y^{\top} \boldsymbol{C} \boldsymbol{B_0} + y^2 \boldsymbol{B}_y^{\top} \boldsymbol{C} \boldsymbol{B_y} + yz\boldsymbol{B}_y^{\top} \boldsymbol{C} \boldsymbol{B}_z \\ & z\boldsymbol{B}_z^{\top} \boldsymbol{C} \boldsymbol{B_0} + yz\boldsymbol{B}_z^{\top} \boldsymbol{C} \boldsymbol{B_y} + z^2 \boldsymbol{B}_z^{\top} \boldsymbol{C} \boldsymbol{B}_z \Big) dxdydz \end{aligned} \tag{4.41}$$

Integrating first on y and z:

$$\begin{aligned} \boldsymbol{K_e} = \int_x \Bigg(& \boldsymbol{B_0}^{\top} \boldsymbol{C} \boldsymbol{B_0} \iint_{y,z} dydz + \boldsymbol{B_0}^{\top} \boldsymbol{C} \boldsymbol{B_y} \iint_{y,z} ydydz + \boldsymbol{B_0}^{\top} \boldsymbol{C} \boldsymbol{B}_z \iint_{y,z} zdydz \\ & \boldsymbol{B}_y^{\top} \boldsymbol{C} \boldsymbol{B_0} \iint_{y,z} ydydz + \boldsymbol{B}_y^{\top} \boldsymbol{C} \boldsymbol{B_y} \iint_{y,z} y^2 dydz + \boldsymbol{B}_y^{\top} \boldsymbol{C} \boldsymbol{B}_z \iint_{y,z} yzdydz \\ & \boldsymbol{B}_z^{\top} \boldsymbol{C} \boldsymbol{B_0} \iint_{y,z} zdydz + \boldsymbol{B}_z^{\top} \boldsymbol{C} \boldsymbol{B_y} \iint_{y,z} yzdydz + \boldsymbol{B}_z^{\top} \boldsymbol{C} \boldsymbol{B}_z \iint_{y,z} z^2 dydz \Bigg) dxdydz \end{aligned} \tag{4.42}$$

Therefore, it is possible to integrate directly using matrix $\boldsymbol{B}$:

$$\boldsymbol{K_e} = \int_{\Omega} \boldsymbol{B}^{\top} \boldsymbol{C} \boldsymbol{B} d\Omega = \iiint_{x,y,z} \boldsymbol{B}^{\top} \boldsymbol{C} \boldsymbol{B} dxdydz \tag{4.43}$$

This matrix is taken from the element's local coordinate system (x,y,z). Thus, to visualize the matrix in the global coordinate system (X,Y,Z), it is necessary to identify the degrees of freedom in both coordinate systems (see Fig. 20):

Figure 20 – Local and global coordinate systems.

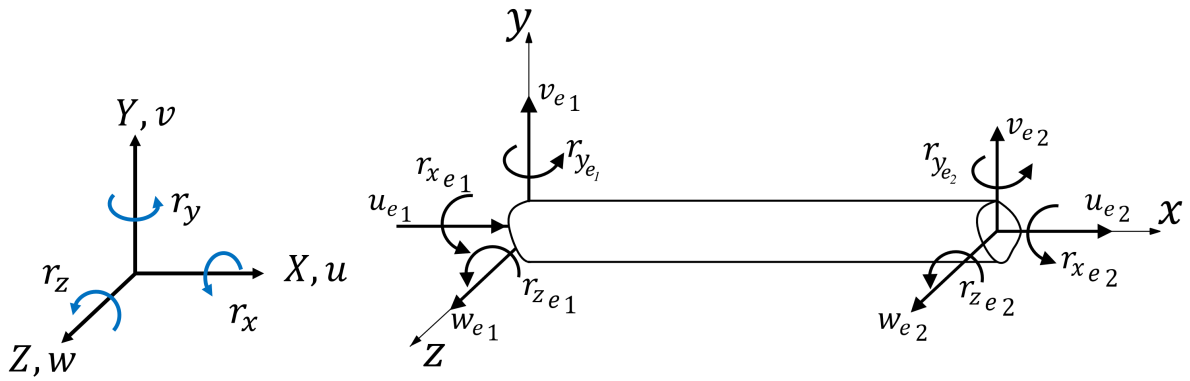

Source: Castro (2022b).

- Degrees of freedom of nodes 1 and 2 in the element's local system:

$$u_{e_1}, v_{e_1}, w_{e_1}, r_{x_{e_1}}, r_{y_{e_1}}, r_{z_{e_1}}, u_{e_2}, v_{e_2}, w_{e_2}, r_{x_{e_2}}, r_{y_{e_2}}, r_{z_{e_2}}$$

- Degrees of freedom of nodes 1 and 2 in the element's global system:

$$u_1, v_1, w_1, r_{x_1}, r_{y_1}, r_{z_1}, u_2, v_2, w_2, r_{x_2}, r_{y_2}, r_{z_2}$$

where $\boldsymbol{x}$ is defined by the spatial position of nodes 1 and 2:

$$\boldsymbol{x} = \boldsymbol{r_2} - \boldsymbol{r_1} \tag{4.44}$$

$\boldsymbol{z}$ requires definition of a vector v_{xy} the xy-plane (local coordinate):

$$\boldsymbol{z} = \boldsymbol{x} \times \boldsymbol{v_{xy}} \tag{4.45}$$

and y is defined from x and z:

$$\boldsymbol{y} = \boldsymbol{z} \times \boldsymbol{x} \tag{4.46}$$

Assuming that both coordinate systems have the same origin, the transformation between them can be written in matrix form:

$$\begin{Bmatrix} x_i \\ x_j \\ x_k \end{Bmatrix} = [R] \begin{Bmatrix} X \\ 0 \\ 0 \end{Bmatrix} = [R] \begin{Bmatrix} 1 \\ 0 \\ 0 \end{Bmatrix} \tag{4.47}$$

$$\begin{Bmatrix} y_i \\ y_j \\ y_k \end{Bmatrix} = [R] \begin{Bmatrix} 0 \\ Y \\ 0 \end{Bmatrix} = [R] \begin{Bmatrix} 0 \\ 1 \\ 0 \end{Bmatrix} \tag{4.48}$$

$$\begin{Bmatrix} Z_i \\ Z_j \\ Z_k \end{Bmatrix} = [R] \begin{Bmatrix} 0 \\ 0 \\ Z \end{Bmatrix} = [R] \begin{Bmatrix} 0 \\ 0 \\ 1 \end{Bmatrix} \tag{4.49}$$

where matrix $[R]$ is defined as:

$$[R] = \begin{bmatrix} r_{11} & r_{12} & r_{13} \\ r_{21} & r_{22} & r_{23} \\ r_{31} & r_{32} & r_{33} \end{bmatrix} \tag{4.50}$$

$$\begin{array}{lll} x_i = r_{11} & y_i = r_{12} & z_i = r_{13} \\ x_j = r_{21} & y_j = r_{22} & z_j = r_{23} \\ x_k = r_{31} & y_k = r_{32} & z_k = r_{33} \end{array}$$

For the degrees of freedom of displacements and rotations, the transformation for nodes 1 and 2 of the truss becomes:

$$\begin{Bmatrix} u_{e_1} \\ v_{e_1} \\ w_{e_1} \\ r_{x_{e_1}} \\ r_{y_{e_1}} \\ r_{z_{e_1}} \end{Bmatrix} = [R_1] \begin{Bmatrix} u_1 \\ v_1 \\ w_1 \\ r_{x_1} \\ r_{y_1} \\ r_{z_1} \end{Bmatrix} \tag{4.51}$$

$$\begin{Bmatrix} u_{e_2} \\ v_{e_2} \\ w_{e_2} \\ r_{x_e} \\ r_{y_e} \\ r_{z_{e_2}} \end{Bmatrix} = [R_2] \begin{Bmatrix} u_2 \\ v_2 \\ w_2 \\ r_{x_2} \\ r_{y_2} \\ r_{z_2} \end{Bmatrix} \tag{4.52}$$

where

$$[R_1] = [R_2] = \begin{bmatrix} r_{11} & r_{12} & r_{13} & 0 & 0 & 0 \\ r_{21} & r_{22} & r_{23} & 0 & 0 & 0 \\ r_{31} & r_{32} & r_{33} & 0 & 0 & 0 \\ 0 & 0 & 0 & r_{11} & r_{12} & r_{13} \\ 0 & 0 & 0 & r_{21} & r_{22} & r_{23} \\ 0 & 0 & 0 & r_{31} & r_{32} & r_{33} \end{bmatrix} \tag{4.53}$$

or reorganizing together:

$$\begin{Bmatrix} u_{e_1} \\ v_{e_1} \\ w_{e_1} \\ r_{x_{e_1}} \\ r_{y_{e_1}} \\ r_{z_{e_1}} \\ u_{e_2} \\ v_{e_2} \\ w_{e_2} \\ r_{x_2} \\ r_{y_{e_2}} \\ r_{z_2} \end{Bmatrix} = [R] \begin{Bmatrix} u_1 \\ v_1 \\ w_1 \\ r_{x_1} \\ r_{y_1} \\ r_{z_1} \\ u_2 \\ v_2 \\ w_2 \\ r_{x_2} \\ r_{y_2} \\ r_{z_2} \end{Bmatrix} \tag{4.54}$$

where

$$[R] = \begin{bmatrix} r_{11} & r_{12} & r_{13} & 0 & 0 & 0 & & & & & & \\ r_{21} & r_{22} & r_{23} & 0 & 0 & 0 & & & & & & \\ r_{31} & r_{32} & r_{33} & 0 & 0 & 0 & & & & & & \\ 0 & 0 & 0 & r_{11} & r_{12} & r_{13} & & & 0 & & & \\ 0 & 0 & 0 & r_{21} & r_{22} & r_{23} & & & & & & \\ 0 & 0 & 0 & r_{31} & r_{32} & r_{33} & & & & & & \\ & & & & & & r_{11} & r_{12} & r_{13} & 0 & 0 & 0 \\ & & & & & & r_{21} & r_{22} & r_{23} & 0 & 0 & 0 \\ & & & 0 & & & r_{31} & r_{32} & r_{33} & 0 & 0 & 0 \\ & & & & & & 0 & 0 & 0 & r_{11} & r_{12} & r_{13} \\ & & & & & & 0 & 0 & 0 & r_{21} & r_{22} & r_{23} \\ & & & & & & 0 & 0 & 0 & r_{31} & r_{32} & r_{33} \end{bmatrix} \tag{4.55}$$

Finally,

$$\begin{aligned} \{\bar{u}_e\} &= [R]\{\bar{u}\} \\ \overline{\boldsymbol{u}}_{\boldsymbol{e}} &= \boldsymbol{R}\overline{\boldsymbol{u}} \end{aligned} \tag{4.56}$$

Back to constitutive stiffness matrix, from Eqs. (4.38) and (4.43), it follows:

$$\delta U_e = \overline{\boldsymbol{u}}_{\boldsymbol{e}}^{\top} \boldsymbol{K}_{\boldsymbol{e}} \delta \overline{\boldsymbol{u}}_{\boldsymbol{e}} \tag{4.57}$$

In terms of global displacements:

$$\overline{\boldsymbol{u}}_e = \boldsymbol{R}\overline{\boldsymbol{u}} \tag{4.58}$$

$$\overline{\boldsymbol{u}}_{\boldsymbol{e}}^{\top} = \overline{\boldsymbol{u}}^{\top} \boldsymbol{R}^{\top} \tag{4.59}$$

$$\delta U_e = \overline{\boldsymbol{u}}^\top \boldsymbol{R}^\top \boldsymbol{K_e} \boldsymbol{R} \delta \overline{\boldsymbol{u}} \tag{4.60}$$

Therefore, the stiffness matrix in the global coordinate systems becomes:

$$\boldsymbol{K} = \boldsymbol{R}^\top \boldsymbol{K_e} \boldsymbol{R} \tag{4.61}$$

Analogously, the consistent mass matrix in the global coordinate system can be obtained:

$$\boldsymbol{M} = \boldsymbol{R}^\top \boldsymbol{M}_e \boldsymbol{R} \tag{4.62}$$

where

$$\begin{aligned} \boldsymbol{M_e} = \int_{x_e} \iint_{y_e,z_e} \rho \Big[& \left(\boldsymbol{N^u}^\top - \boldsymbol{N^{r_z}}^\top y_e + \boldsymbol{N^{r_y}}^\top z_e \right) \left(\boldsymbol{N^u} - \boldsymbol{N^{r_z}} y_e + \boldsymbol{N^{r_y}} z_e \right) \\ & + \left(\boldsymbol{N^v}^\top - \boldsymbol{N^{r_x}}^\top z_e \right) \left(\boldsymbol{N^v} - \boldsymbol{N^{r_x}} z_e \right) \\ & + \left(\boldsymbol{N^w}^\top + \boldsymbol{N^{r_x}}^\top y_e \right) \left(\boldsymbol{N^w} + \boldsymbol{N^{r_x}} y_e \right) \Big] \, dy_e dz_e dx_e \end{aligned} \tag{4.63}$$

4.3 Plate Formulation using the First-Order Shear Deformation Theory (FSDT)

Plates are two-dimensional structures with one dimension that is at least one order of magnitude smaller than the in-plane dimensions a and b, in general the thickness h (see Fig. 21). This fact allows the 3D problem to be reduced to a 2D problem. The problem defined at each point $Q_V(x,y,z)$ of the 3D continuum plate is transformed into a problem defined at each point $Q_\Omega(x,y)$ of the plate surface Ω.

Figure 21 – Plate geometry and reference system.

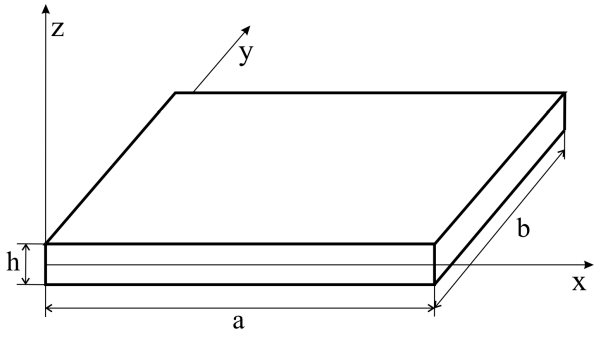

Source: Elaborated by the author.

Plate modeling in two dimensions is a classic problem in structural theory. The z-coordinate can be eliminated using a variety of methodologies, resulting in a large number of approaches and procedures. For example, the unknown variables can be assumed axiomatically along z. This means that a polynomial expansion in z will give the distribution of the unknowns along the thickness at a given point $Q_\Omega(x,y)$ in the plane. For this work, it is applied the Reissner-Mindlin theory, also called First-order Shear Deformation Theory (FSDT).

Reissner-Mindlin theory modifies Kirchhoff's hypothesis regarding the orthogonality of the transverse lines in relation to the plate plane. In this case, the lines normal to the plane of the plate do not remain orthogonal after its deformation, as the influence of transverse shear deformations is now considered. According to Oñate (2013), the Reissner-Mindlin theory has advantages over the Kirchhoff theory in the application of the finite element method. While according to Kirchhoff's theory there is great difficulty in finding functions that satisfy the continuity conditions required by the strains and rotations of the elements; by Reissner-Mindlin theory, constraints are reduced, allowing the use of shape functions of class C^0, which eliminates the effects of non-conformity.

However, according to Filho (1997), the Reissner-Mindlin theory can cause numerical difficulties in the analysis of very thin plates, generating very rigid solutions due to the excessive influence of the shear force terms. In the literature, this effect is known as *shear locking*. To solve this problem, reduced integration techniques are applied or interpolation functions of orders greater than three are used.

Figure 22 depicts the distribution of displacements in FSDT for the plate.

Figure 22 – Distribution of displacements in FSDT.

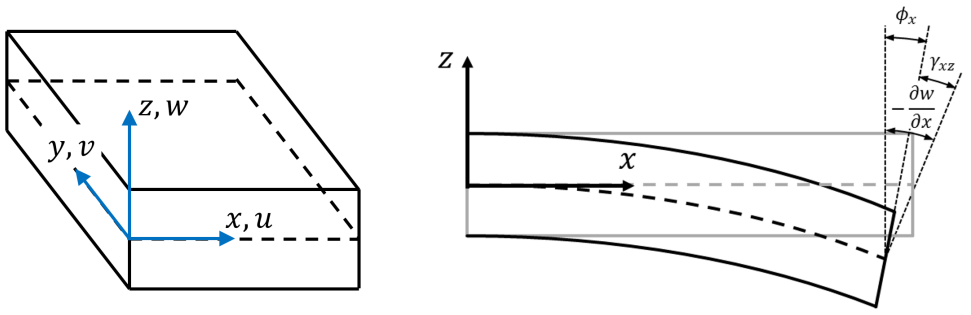

Source: Castro (2022b).

The displacement field in the case of FSDT is given by:

$$\begin{aligned} u(x,y,z) &= u_0(x,y) + z\phi_x(x,y) \\ v(x,y,z) &= v_0(x,y) + z\phi_y(x,y) \\ w(x,y,z) &= w_0(x,y) \end{aligned} \tag{4.64}$$

The strain components are obtained by substituting the displacement field from Eqs. (4.64) in the geometrical relations. Only strain ε_{zz} is zero, so the not-null strains are given by:

$$\boldsymbol{\varepsilon} = \left\{ \begin{array}{c} \varepsilon_{xx} \\ \varepsilon_{yy} \\ 2\varepsilon_{xy} \\ 2\varepsilon_{yz} \\ 2\varepsilon_{xz} \end{array} \right\} = \left\{ \begin{array}{c} \dfrac{\partial u}{\partial x} \\ \dfrac{\partial v}{\partial y} \\ \dfrac{\partial u}{\partial y} + \dfrac{\partial v}{\partial x} \\ \dfrac{\partial w}{\partial y} + \phi_y \\ \dfrac{\partial w}{\partial x} + \phi_x \end{array} \right\} \tag{4.65}$$

$$\boldsymbol{\varepsilon} = \left\{ \begin{array}{c} \varepsilon_{xx} \\ \varepsilon_{yy} \\ 2\varepsilon_{xy} \\ 2\varepsilon_{yz} \\ 2\varepsilon_{xz} \end{array} \right\} = \left\{ \begin{array}{c} u_{0,x} \\ v_{0,y} \\ u_{0,y} + v_{0,x} \\ w_{,y} + \phi_y \\ w_{,x} + \phi_x \end{array} \right\} + z \left\{ \begin{array}{c} \phi_{x,x} \\ \phi_{y,y} \\ \phi_{x,y} + \phi_{y,x} \\ 0 \\ 0 \end{array} \right\} \tag{4.66}$$

$$\boldsymbol{\varepsilon} = \boldsymbol{\varepsilon_0} + z\boldsymbol{\varepsilon_1} \tag{4.67}$$

Usually, the subscript "0" is omitted in the formulation:

$$\boldsymbol{\varepsilon_0} = \left\{ \begin{array}{c} \varepsilon_{xx} \\ \varepsilon_{yy} \\ \gamma_{xy} \\ \gamma_{yz} \\ \gamma_{xz} \end{array} \right\} \quad \boldsymbol{\varepsilon_1} = \left\{ \begin{array}{c} \kappa_{xx} \\ \kappa_{yy} \\ \kappa_{xy} \\ 0 \\ 0 \end{array} \right\} \tag{4.68}$$

The variation of strain energy of the plate can be written as:

$$\delta U = \int_\Omega \boldsymbol{\sigma}^T \delta\varepsilon d\Omega = \int_\Omega \boldsymbol{\sigma}^T \left(\delta\varepsilon_0 + z\delta\boldsymbol{\varepsilon_1}\right) d\Omega \tag{4.69}$$

where $\boldsymbol{\sigma}$ is the vector of in-plane stresses and the shear stresses, given by:

$$\boldsymbol{\sigma} = \left\{ \begin{array}{c} \sigma_{xx} \\ \sigma_{yy} \\ \tau_{xy} \\ \tau_{yz} \\ \tau_{xz} \end{array} \right\} \tag{4.70}$$

Separating integration of Eq. (4.69) through the thickness, it follows:

$$\delta U = \iint_{xy} \left(\int_{z=-\frac{h}{2}}^{+\frac{h}{2}} \boldsymbol{\sigma}^T \delta \boldsymbol{\varepsilon_0} dz + \int_{z=-\frac{h}{2}}^{+\frac{h}{2}} z \boldsymbol{\sigma}^T \delta \boldsymbol{\varepsilon_1} dz \right) dxdy \tag{4.71}$$

$$\delta U = \iint_{xy} \left[\left(\int_{z=-\frac{h}{2}}^{+\frac{h}{2}} \boldsymbol{\sigma}^T dz \right) \delta \boldsymbol{\varepsilon_0} + \left(\int_{z=-\frac{h}{2}}^{+\frac{h}{2}} z \boldsymbol{\sigma}^T dz \right) \delta \boldsymbol{\varepsilon_1} \right] dxdy \tag{4.72}$$

$$\delta U = \iint_{xy} \left[\left(\int_{z=-\frac{h}{2}}^{+\frac{h}{2}} \begin{Bmatrix} \sigma_{xx} \\ \sigma_{yy} \\ \tau_{xy} \\ \tau_{yz} \\ \tau_{xz} \end{Bmatrix}^T dz \right) \delta \boldsymbol{\varepsilon_0} + \left(\int_{z=-\frac{h}{2}}^{+\frac{h}{2}} z \begin{Bmatrix} \sigma_{xx} \\ \sigma_{yy} \\ \tau_{xy} \\ \tau_{yz} \\ \tau_{xz} \end{Bmatrix}^T dz \right) \delta \boldsymbol{\varepsilon_1} \right] dxdy \tag{4.73}$$

The membrane stresses, transverse stresses and bending stresses (see Fig. 23) can be obtained integrating the stresses along the thickness of the FSDT plate:

Figure 23 – Direction of forces and moments of the FSDT plate.

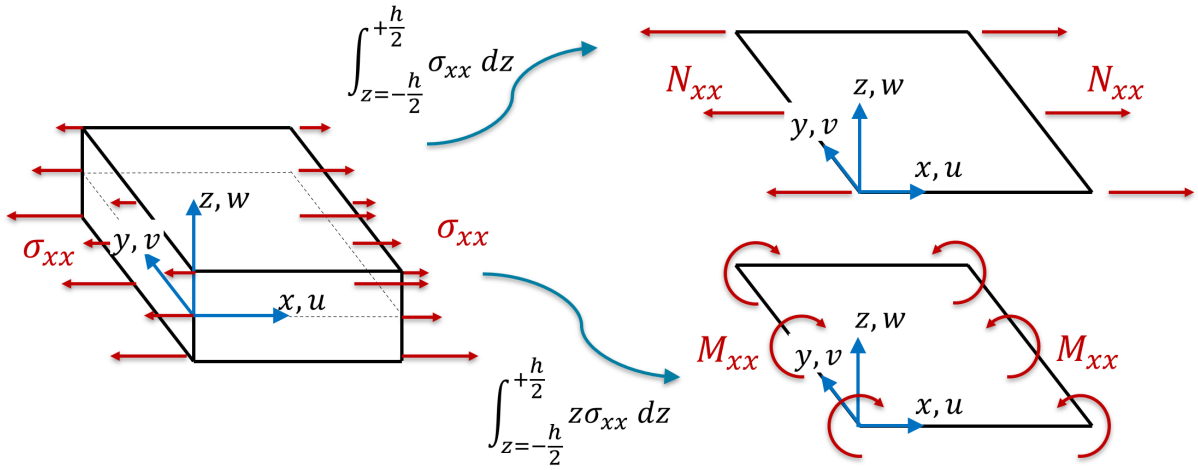

Source: Castro (2022b).

$$\begin{Bmatrix} N_{xx} \\ N_{yy} \\ N_{xy} \\ Q_y \\ Q_x \end{Bmatrix} = \boldsymbol{N} = \int_{z=-\frac{h}{2}}^{+\frac{h}{2}} \begin{Bmatrix} \sigma_{xx} \\ \sigma_{yy} \\ \tau_{xy} \\ \tau_{yz} \\ \tau_{xz} \end{Bmatrix} dz \tag{4.74}$$

$$\left\{ \begin{array}{c} M_{xx} \\ M_{yy} \\ M_{xy} \\ 0 \\ 0 \end{array} \right\} = \boldsymbol{M} = \int_{z=-\frac{h}{2}}^{+\frac{h}{2}} z \left\{ \begin{array}{c} \sigma_{xx} \\ \sigma_{yy} \\ \tau_{xy} \\ \tau_{yz} \\ \tau_{xz} \end{array} \right\} dz \tag{4.75}$$

Applying Eqs. (4.74) and (4.75) into Eq. (4.72), it follows:

$$\delta U = \iint_{xy} \left(\left\{ \begin{array}{c} N_{xx} \\ N_{yy} \\ N_{xy} \\ Q_y \\ Q_x \end{array} \right\}^T \delta \boldsymbol{\varepsilon_0} + \left\{ \begin{array}{c} M_{xx} \\ M_{yy} \\ M_{xy} \\ 0 \\ 0 \end{array} \right\}^T \delta \boldsymbol{\varepsilon_1} \right) dxdy \tag{4.76}$$

$$\delta U = \iint_{xy} \left(\left\{ \begin{array}{c} N_{xx} \\ N_{yy} \\ N_{xy} \end{array} \right\}^T \left\{ \begin{array}{c} \delta\varepsilon_{xx} \\ \delta\varepsilon_{yy} \\ \delta\gamma_{xy} \end{array} \right\} + \left\{ \begin{array}{c} Q_y \\ Q_x \end{array} \right\}^T \left\{ \begin{array}{c} \delta\tau_{yz} \\ \delta\tau_{xz} \end{array} \right\} + \left\{ \begin{array}{c} M_{xx} \\ M_{yy} \\ M_{xy} \end{array} \right\}^T \left\{ \begin{array}{c} \delta\kappa_{xx} \\ \delta\kappa_{yy} \\ \delta\kappa_{xy} \end{array} \right\} \right) dxdy \tag{4.77}$$

$$\delta U = \iint_{xy} \left(\boldsymbol{N}^T \left\{ \begin{array}{c} \delta\varepsilon_{xx} \\ \delta\varepsilon_{yy} \\ \delta\gamma_{xy} \end{array} \right\} + \boldsymbol{Q}^T \left\{ \begin{array}{c} \delta\tau_{yz} \\ \delta\tau_{xz} \end{array} \right\} + \boldsymbol{M}^T \left\{ \begin{array}{c} \delta\kappa_{xx} \\ \delta\kappa_{yy} \\ \delta\kappa_{xy} \end{array} \right\} \right) dxdy \tag{4.78}$$

The constitutive relations are used to obtain the in-plane stresses and the shear stress components:

$$\left\{ \begin{array}{c} \sigma_{xx} \\ \sigma_{yy} \\ \tau_{xy} \end{array} \right\} = \frac{E}{1-\nu^2} \left[\begin{array}{ccc} 1 & \nu & 0 \\ -\nu & 1 & 0 \\ 0 & 0 & \frac{1-\nu}{2} \end{array} \right] \left\{ \begin{array}{c} \varepsilon_{xx} \\ \varepsilon_{yy} \\ \gamma_{xy} \end{array} \right\} \tag{4.79}$$

$$\left\{ \begin{array}{c} \tau_{yz} \\ \tau_{xz} \end{array} \right\} = \frac{E}{1-\nu^2} \left[\begin{array}{cc} \frac{1-\nu}{2} & 0 \\ 0 & \frac{1-\nu}{2} \end{array} \right] \left\{ \begin{array}{c} \gamma_{yz} \\ \gamma_{xz} \end{array} \right\} \tag{4.80}$$

The shear stresses can still be written as:

$$\tau_{xz} = \kappa G \gamma_{xz} \tag{4.81}$$

$$\tau_{yz} = \kappa G \gamma_{yz} \tag{4.82}$$

where κ is the shear correction factor. Similarly to the Timoshenko beam theory (TBT), the shear predicted by FSDT should be corrected since the model yields a constant value along the thickness, whereas it is at least parabolic in order to satisfy the stress free boundary conditions on the unloaded top and bottom faces of the plate. In literature, there are many methods to compute κ for the FSDT; for instance, Babuska, d'Harcourt and Schwab (1991) and Rössle (1999) present some of them.

Calculating the membrane stresses ($\boldsymbol{N}$), it follows:

$$\boldsymbol{N} = \left\{ \begin{array}{c} N_{xx} \\ N_{yy} \\ N_{xy} \end{array} \right\} \tag{4.83}$$

$$\boldsymbol{N} = \int_{-\frac{h}{2}}^{+\frac{h}{2}} \left\{ \begin{array}{c} \sigma_{xx} \\ \sigma_{yy} \\ \tau_{xy} \end{array} \right\} dz = \int_{-\frac{h}{2}}^{+\frac{h}{2}} \boldsymbol{C} \left(\left\{ \begin{array}{c} \varepsilon_{xx} \\ \varepsilon_{yy} \\ \gamma_{xy} \end{array} \right\} + z \left\{ \begin{array}{c} \kappa_{xx} \\ \kappa_{yy} \\ \kappa_{xy} \end{array} \right\} \right) dz = h\boldsymbol{C} \left\{ \begin{array}{c} \varepsilon_{xx} \\ \varepsilon_{yy} \\ \gamma_{xy} \end{array} \right\} \tag{4.84}$$

where $\boldsymbol{C}$ is given by:

$$\boldsymbol{C} = \frac{E}{1-v^2} \left[\begin{array}{ccc} 1 & v & 0 \\ -v & 1 & 0 \\ 0 & 0 & \dfrac{1-v}{2} \end{array} \right] \tag{4.85}$$

Analogously with composites, with an offset d, it follows:

$$\boldsymbol{N} = \int_{-\frac{h}{2}+d}^{+\frac{h}{2}+d} \left\{ \begin{array}{c} \sigma_{xx} \\ \sigma_{yy} \\ \tau_{xy} \end{array} \right\} dz = h\boldsymbol{C} \left\{ \begin{array}{c} \varepsilon_{xx} \\ \varepsilon_{yy} \\ \gamma_{xy} \end{array} \right\} + dh\boldsymbol{C} \left\{ \begin{array}{c} \kappa_{xx} \\ \kappa_{yy} \\ \kappa_{xy} \end{array} \right\} \tag{4.86}$$

Calculating the bending stresses ($\boldsymbol{M}$), it follows:

$$\boldsymbol{M} = \left\{ \begin{array}{c} M_{xx} \\ M_{yy} \\ M_{xy} \end{array} \right\} \tag{4.87}$$

$$\boldsymbol{M} = \int_{-\frac{h}{2}}^{+\frac{h}{2}} z \left\{ \begin{array}{c} \sigma_{xx} \\ \sigma_{yy} \\ \tau_{xy} \end{array} \right\} dz = \int_{-\frac{h}{2}}^{+\frac{h}{2}} \boldsymbol{C} \left(z \left\{ \begin{array}{c} \varepsilon_{xx} \\ \varepsilon_{yy} \\ \gamma_{xy} \end{array} \right\} + z^2 \left\{ \begin{array}{c} \kappa_{xx} \\ \kappa_{yy} \\ \kappa_{xy} \end{array} \right\} \right) dz = \frac{h^3}{12} \boldsymbol{C} \left\{ \begin{array}{c} \kappa_{xx} \\ \kappa_{yy} \\ \kappa_{xy} \end{array} \right\} \tag{4.88}$$

Analogously with composites, with an offset d, it follows:

$$\boldsymbol{M} = \int_{-\frac{h}{2}+d}^{+\frac{h}{2}+d} z \left\{ \begin{array}{c} \sigma_{xx} \\ \sigma_{yy} \\ \tau_{xy} \end{array} \right\} dz = dh\boldsymbol{C} \left\{ \begin{array}{c} \varepsilon_{xx} \\ \varepsilon_{yy} \\ \gamma_{xy} \end{array} \right\} + h \left(d^2 + \frac{h^2}{12} \right) \boldsymbol{C} \left\{ \begin{array}{c} \kappa_{xx} \\ \kappa_{yy} \\ \kappa_{xy} \end{array} \right\} \tag{4.89}$$

Calculating the transverse stresses ($\boldsymbol{Q}$), it follows:

$$\boldsymbol{Q} = \left\{ \begin{array}{c} Q_y \\ Q_x \end{array} \right\} \tag{4.90}$$

$$\boldsymbol{Q} = \int_{-\frac{h}{2}}^{+\frac{h}{2}} \left\{ \begin{array}{c} \tau_{yz} \\ \tau_{xz} \end{array} \right\} dz = \int_{-\frac{h}{2}}^{+\frac{h}{2}} \boldsymbol{S} \left\{ \begin{array}{c} \gamma_{yz} \\ \gamma_{xz} \end{array} \right\} dz = h\boldsymbol{S} \left\{ \begin{array}{c} \gamma_{yz} \\ \gamma_{xz} \end{array} \right\} \tag{4.91}$$

where $\boldsymbol{S}$ is given by:

$$\boldsymbol{S} = \frac{E}{1-v^2} \left[\begin{array}{cc} \frac{1-v}{2} & 0 \\ 0 & \frac{1-v}{2} \end{array} \right] \tag{4.92}$$

and with an offset, it becomes:

$$\boldsymbol{Q} = h\boldsymbol{S} \left\{ \begin{array}{c} \gamma_{yz} \\ \gamma_{xz} \end{array} \right\} \tag{4.93}$$

4.3.1 Interpolation Function

Likewise in the truss element formulation, here it is used the natural coordinates to calculate the stresses and strains for any element, since this approaches makes it easier to interpolate and easier to apply numerical integration.

Similar to one-dimensional elements, a natural coordinate system can be introduced for a two-dimensional element by normalizing the dimensional lengths along x and y, respectively. Fig. 24 shows the normalization: the length along x- and y-axes is set as 2 units, and the origin of the natural coordinate system is set at the geometric center of the rectangle element. As the result, the coordinates of four nodes in a natural coordinate system are $(-1,-1)$,$(+1,-1)$,$(+1,+1)$,$(-1,+1)$ for nodes 1, 2, 3, and 4, respectively.

The interpolations equations in natural coordinate system are then defined:

$$\begin{aligned} N_1(\xi,\eta) &= \frac{1}{4}(\xi\eta - \xi - \eta + 1) \\ N_2(\xi,\eta) &= -\frac{1}{4}(\xi\eta - \xi + \eta - 1) \\ N_3(\xi,\eta) &= \frac{1}{4}(\xi\eta + \xi + \eta + 1) \\ N_4(\xi,\eta) &= -\frac{1}{4}(\xi\eta + \xi - \eta - 1) \end{aligned} \tag{4.94}$$

Figure 24 – Natural coordinate system in two-dimensional rectangle element.

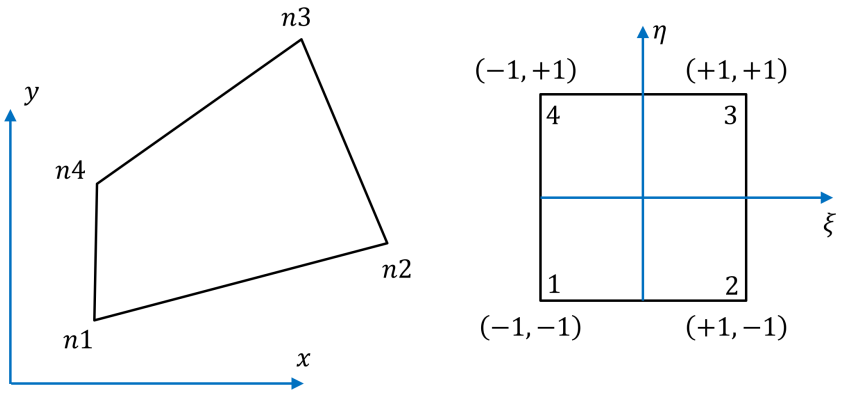

Source: Castro (2022b).

and the displacement and rotational field are expressed as:

$$
\begin{aligned}
u(\xi,\eta) &= \sum_{i=1}^{4} N_i(\xi,\eta)u_i \\
v(\xi,\eta) &= \sum_{i=1}^{4} N_i(\xi,\eta)v_i \\
w(\xi,\eta) &= \sum_{i=1}^{4} N_i(\xi,\eta)w_i \\
\phi_x(\xi,\eta) &= \sum_{i=1}^{4} N_i(\xi,\eta)\phi_{x_i} \\
\phi_y(\xi,\eta) &= \sum_{i=1}^{4} N_i(\xi,\eta)\phi_{y_i}
\end{aligned}
\tag{4.95}
$$

Figure 25 shows the relation between cartesian and natural coordinate system. Note that $\boldsymbol{r}$ is a vector in the x and y space defined as a function of ξ and η; thus providing $x(\xi,\eta)$ and $y(\xi,\eta)$:

Figure 25 – Natural coordinate system in two-dimensional rectangle element.

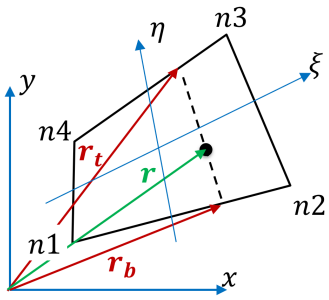

Source: Castro (2022b).

$$\boldsymbol{r_b}(\xi) = \boldsymbol{r_1} + (\boldsymbol{r_2} - \boldsymbol{r_1}) \frac{(\xi + 1)}{2} \tag{4.96}$$

$$\boldsymbol{r_t}(\xi) = \boldsymbol{r_4} + (\boldsymbol{r}_3 - \boldsymbol{r_4}) \frac{(\xi + 1)}{2} \tag{4.97}$$

$$\boldsymbol{r}(\xi, \eta) = \boldsymbol{r_b}(\xi) + (\boldsymbol{r_t}(\xi) - \boldsymbol{r_b}(\xi)) \frac{(\eta + 1)}{2} \tag{4.98}$$

A more general procedure for finding $x(\xi, \eta)$ and $y(\xi, \eta)$ usually involves Lagrange polynomials.

Due to the use of natural coordinates, it is necessary to express the kinematic equations (strain-displacements) in terms of natural coordinates. Therefore, if $x(\xi, \eta)$ and $y(\xi, \eta)$, it comes that $\xi(x, y)$ and $\eta(x, y)$, such that:

$$\frac{\partial f}{\partial x} = \frac{\partial f}{\partial \xi}\frac{\partial \xi}{\partial x} + \frac{\partial f}{\partial \eta}\frac{\partial \eta}{\partial x} \tag{4.99}$$

$$\frac{\partial f}{\partial y} = \frac{\partial f}{\partial \xi}\frac{\partial \xi}{\partial y} + \frac{\partial f}{\partial \eta}\frac{\partial \eta}{\partial y} \tag{4.100}$$

It is worthy mentioning that $\xi(x, y)$ and $\eta(x, y)$ usually do not have analytical expressions. Therefore, the values for $\frac{\partial \xi}{\partial x}$, $\frac{\partial \xi}{\partial y}$, $\frac{\partial \eta}{\partial x}$, $\frac{\partial \eta}{\partial y}$ are calculated numerically.

Furthermore, having those relations stated, it is possible to rewrite the strains in natural coordinates:

$$\begin{aligned}
\varepsilon_{xx} &= \frac{\partial u}{\partial x} = \frac{\partial u}{\partial \xi}\frac{\partial \xi}{\partial x} + \frac{\partial u}{\partial \eta}\frac{\partial \eta}{\partial x} \\
\varepsilon_{yy} &= \frac{\partial v}{\partial y} = \frac{\partial v}{\partial \xi}\frac{\partial \xi}{\partial y} + \frac{\partial v}{\partial \eta}\frac{\partial \eta}{\partial y} \\
\gamma_{xy} &= \frac{\partial u}{\partial y} + \frac{\partial v}{\partial x} = \frac{\partial u}{\partial \xi}\frac{\partial \xi}{\partial y} + \frac{\partial u}{\partial \eta}\frac{\partial \eta}{\partial y} + \frac{\partial v}{\partial \xi}\frac{\partial \xi}{\partial x} + \frac{\partial v}{\partial \eta}\frac{\partial \eta}{\partial x}
\end{aligned} \tag{4.101}$$

The corresponding derivatives in terms of natural coordinate system are calculated applying the chain rule:

$$\begin{aligned}
\frac{\partial f}{\partial \xi} &= \frac{\partial f}{\partial x}\frac{\partial x}{\partial \xi} + \frac{\partial f}{\partial y}\frac{\partial y}{\partial \xi} \\
\frac{\partial f}{\partial \eta} &= \frac{\partial f}{\partial x}\frac{\partial x}{\partial \eta} + \frac{\partial f}{\partial y}\frac{\partial y}{\partial \eta}
\end{aligned} \quad \text{and} \quad
\begin{aligned}
\frac{\partial f}{\partial x} &= \frac{\partial f}{\partial \xi}\frac{\partial \xi}{\partial x} + \frac{\partial f}{\partial \eta}\frac{\partial \eta}{\partial x} \\
\frac{\partial f}{\partial y} &= \frac{\partial f}{\partial \xi}\frac{\partial \xi}{\partial x} + \frac{\partial f}{\partial \eta}\frac{\partial \eta}{\partial x}
\end{aligned} \tag{4.102}$$

or in matrix form:

$$\begin{Bmatrix} \frac{\partial}{\partial \xi} \\ \frac{\partial}{\partial \eta} \end{Bmatrix} = \boldsymbol{J} \begin{Bmatrix} \frac{\partial}{\partial x} \\ \frac{\partial}{\partial y} \end{Bmatrix} \quad \text{and} \quad \begin{Bmatrix} \frac{\partial}{\partial x} \\ \frac{\partial}{\partial y} \end{Bmatrix} = \boldsymbol{J}^{-1} \begin{Bmatrix} \frac{\partial}{\partial \xi} \\ \frac{\partial}{\partial \eta} \end{Bmatrix} \tag{4.103}$$

where matrix $\boldsymbol{J}$ is the Jacobian, which is expressed by:

$$\boldsymbol{J} = \begin{bmatrix} \dfrac{\partial x}{\partial \xi} & \dfrac{\partial y}{\partial \xi} \\ \dfrac{\partial x}{\partial \eta} & \dfrac{\partial y}{\partial \eta} \end{bmatrix} \quad \text{and} \quad \boldsymbol{J^{-1}} = \begin{bmatrix} \dfrac{\partial \xi}{\partial x} & \dfrac{\partial \eta}{\partial x} \\ \dfrac{\partial \xi}{\partial y} & \dfrac{\partial \eta}{\partial y} \end{bmatrix} \tag{4.104}$$

Equation (4.78) was written in terms of cartesian coordinates. Thus, it is necessary to transform it to natural coordinate system. To do so, the derivatives dx and dy can be expressed in terms of the natural coordinates as:

$$\begin{aligned} \boldsymbol{dx} &= \frac{\partial x}{\partial \xi}\boldsymbol{d\xi} + \frac{\partial x}{\partial \eta}\boldsymbol{d\eta} \\ \boldsymbol{dy} &= \frac{\partial y}{\partial \xi}\boldsymbol{d\xi} + \frac{\partial y}{\partial \eta}\boldsymbol{d\eta} \end{aligned} \tag{4.105}$$

$$dxdy = \begin{vmatrix} \boldsymbol{\xi} & \boldsymbol{\eta} & \mathbf{1} \\ \dfrac{\partial x}{\partial \xi} & \dfrac{\partial x}{\partial \eta} & 0 \\ \dfrac{\partial y}{\partial \xi} & \dfrac{\partial y}{\partial \eta} & 0 \end{vmatrix} = \left(\frac{\partial x}{\partial \xi}\frac{\partial y}{\partial \eta} - \frac{\partial x}{\partial \eta}\frac{\partial y}{\partial \xi} \right) d\xi d\eta = \det \boldsymbol{J} d\xi d\eta \tag{4.106}$$

4.3.2 Consistent Mass Matrices for Plates

To get started, consider the inertial term:

$$\int_{\Omega} \rho \left(\ddot{\boldsymbol{u}}^{\boldsymbol{T}} \delta \boldsymbol{u} \right) d\Omega \tag{4.107}$$

If:

$$\boldsymbol{u} = \begin{Bmatrix} u \\ v \\ w \end{Bmatrix} \tag{4.108}$$

$$\boldsymbol{u} = \boldsymbol{U}(x,y,z) f(t) \tag{4.109}$$

$$\ddot{\boldsymbol{u}} = \boldsymbol{U}(x,y,z) \ddot{f}(t) \tag{4.110}$$

Thus:

$$\ddot{f}(t) \iiint_{x,y,z} \rho \left(\boldsymbol{U}^T \delta \boldsymbol{U} \right) dxdydz f(t) \tag{4.111}$$

For the FSDT:

$$\begin{aligned} u(x,y,z) &= u_0(x,y) + z\phi_x(x,y) \\ v(x,y,z) &= v_0(x,y) + z\phi_y(x,y) \\ w(x,y,z) &= w_0(x,y) \end{aligned} \tag{4.112}$$

$$\ddot{f}(t)\iint_{x,y}\rho\int_{z=-\frac{h}{2}}^{+\frac{h}{2}}\left(\boldsymbol{U}^{\boldsymbol{T}}\delta\boldsymbol{U}\right)dzdxdyf(t) \tag{4.113}$$

where $\boldsymbol{U}$ is given by:

$$\boldsymbol{U}(x,y)=\boldsymbol{N}(x,y)\boldsymbol{U_n} \tag{4.114}$$

Applying Eq. (4.95) into Eq. (4.114), and applying the result into Eq. (4.113), it follows:

$$\ddot{f}(t)\sum_{e}\boldsymbol{M}_e f(t) \tag{4.115}$$

Therefore, the consistent mass matrix for plates are given by:

$$\begin{aligned}\boldsymbol{M_e}=\iint_{\xi,\eta}\rho\Big(&h\left[N^u\right]^T\left[N^u\right]+h\left[N^v\right]^T\left[N^v\right]+h\left[N^w\right]^T\left[N^w\right]\\&+\frac{h^3}{12}\left[N^{\phi_x}\right]^T\left[N^{\phi_x}\right]+\frac{h^3}{12}\left[N^{\phi_y}\right]^T\left[N^{\phi_y}\right]\Big)\det Jd\xi d\eta\end{aligned} \tag{4.116}$$

which is obtained without offset and assuming ρ constant.

4.3.3 Lumped Mass Matrices for 2D Plates

The lumped mass matrix for plates can be expressed as:

$$[M]_e=\begin{array}{c}\begin{array}{ccccccc}u & v & w & \phi_x & \phi_y & & \end{array}\\\begin{bmatrix}m_1 & & & & 0 & & \\ & m_1 & & & & & \\ & & m_1 & & & & \\ & & & I_{yy_1} & & \cdots & \\ & & & & I_{xx_1} & & \\ & 0 & & \vdots & & & \end{bmatrix}\end{array} \tag{4.117}$$

where m_1, I_{yy_1} and I_{xx_1} are given by:

$$m_1=\int_{\eta=-1}^{\eta=0}\int_{\xi=-1}^{\xi=0}\rho h\det\boldsymbol{J}d\xi d\eta \tag{4.118}$$

$$I_{yy_1}=\int_{\eta=-1}^{\eta=0}\int_{\xi=-1}^{\xi=0}(x-x_1)^2\rho h\det Jd\xi d\eta \tag{4.119}$$

$$I_{xx_1}=\int_{\eta=-1}^{\eta=0}\int_{\xi=-1}^{\xi=0}(y-y_1)^2\rho h\det Jd\xi d\eta \tag{4.120}$$

Furthermore, for the other nodes, i.e., nodes 2, 3 and 4, the terms become:

$$m_2 = \int_{\eta=-1}^{\eta=0} \int_{\xi=0}^{\xi=+1} \rho h \det \boldsymbol{J} d\xi d\eta \tag{4.121}$$

$$I_{yy_2} = \int_{\eta=-1}^{\eta=0} \int_{\xi=0}^{\xi=+1} (x-x_2)^2 \rho h \det \boldsymbol{J} d\xi d\eta \tag{4.122}$$

$$I_{xx_2} = \int_{\eta=-1}^{\eta=0} \int_{\xi=0}^{\xi=+1} (y-y_2)^2 \rho h \det \boldsymbol{J} d\xi d\eta \tag{4.123}$$

$$m_3 = \int_{\eta=0}^{\eta=+1} \int_{\xi=0}^{\xi=+1} \rho h \det \boldsymbol{J} d\xi d\eta \tag{4.124}$$

$$I_{yy_3} = \int_{\eta=0}^{\eta=+1} \int_{\xi=0}^{\xi=+1} (x-x_3)^2 \rho h \det \boldsymbol{J} d\xi d\eta \tag{4.125}$$

$$I_{xx_3} = \int_{\eta=0}^{\eta=+1} \int_{\xi=0}^{\xi=+1} (y-y_3)^2 \rho h \det \boldsymbol{J} d\xi d\eta \tag{4.126}$$

$$m_4 = \int_{\eta=0}^{\eta=+1} \int_{\xi=-1}^{\xi=0} \rho h \det \boldsymbol{J} d\xi d\eta \tag{4.127}$$

$$I_{yy_4} = \int_{\eta=0}^{\eta=+1} \int_{\xi=-1}^{\xi=0} (x-x_4)^2 \rho h \det \boldsymbol{J} d\xi d\eta \tag{4.128}$$

$$I_{xx_4} = \int_{\eta=0}^{\eta=+1} \int_{\xi=-1}^{\xi=0} (y-y_4)^2 \rho h \det \boldsymbol{J} d\xi d\eta \tag{4.129}$$

4.3.4 Shear Locking and Drilling

The hourglass control is implemented according to Brockman (1987), where the second derivatives of the bi-linear interpolation functions are used to define generalized hourglass strain components that apply to each translational degree-of-freedom: ε_h^u, ε_h^v and ε_h^w; and generalized hourglass strains that apply to two rotational degrees-of-freedom: $\varepsilon_h^{r_x}$, $\varepsilon_h^{r_y}$; noting that no hourglass strain or stiffness is added to the drilling degree-of-freedom r_z.

A generalized hourglass stiffness is defined for each generalized hourglass strain. Because Brockman's work is based on metallic structures, the originally proposed generalized hourglass stiffnesses need to be modified to account for laminated composite plates as follows:

$$
\begin{aligned}
E_h^u &= \frac{0.1E_{1eq}h}{1.0+1.0/A_e} \\
E_h^v &= \frac{0.1E_{2eq}h}{1.0+1.0/A_e} \\
E_h^{r_x} &= \frac{0.1E_{2eq}h^3}{1.0+1.0/A_e} \\
E_h^{r_y} &= \frac{0.1E_{1eq}h^3}{1.0+1.0/A_e} \\
E_h^w &= \frac{1}{2}(E_h^{r_x}+E_h^{r_y})
\end{aligned}
\tag{4.130}
$$

where A_e is the area of the quadrilateral element; h is the total thickness of the element; $E_{1eq} = 1/(ha_{11})$ and $E_{2eq} = 1/(ha_{22})$ with a_{11} and a_{22} components of the flexibility matrix of the laminated composite plate. The variation of the hourglass strain energy δU_h is therefore given by the integral:

$$
\delta U_h = \bar{\boldsymbol{u}}_{\boldsymbol{e}}{}^{\top} \iint_{x,y} \left(\boldsymbol{N}_h^{u\top} E_h^u \boldsymbol{N}_h^u + \boldsymbol{N}_h^{v\top} E_h^v \boldsymbol{N}_h^v + \boldsymbol{N}_h^{w\top} E_h^w \boldsymbol{N}_h^w + \boldsymbol{N}_h^{r_x\top} E_h^{r_x} \boldsymbol{N}_h^{r_x} + \boldsymbol{N}_h^{r_y\top} E_h^{r_y} \boldsymbol{N}_h^{r_y} \right) dxdy \;\; \delta\bar{\boldsymbol{u}}_{\boldsymbol{e}}
\tag{4.131}
$$

which is then added to the strain energy ultimately contributing to the constitutive stiffness matrix of the system.

The drilling degree-of-freedom is calculated simply penalizing the in-plane rotational shear, as for instance discussed by Adam, Mohamed and Hassaballa (2013). Here, the drilling stiffness $E_{drilling}$ is calculated based on the laminated composite plate stiffness component A_{66}, such that:

$$
E_{drilling} = \frac{A_{66}}{h}
\tag{4.132}
$$

4.3.5 Consistent Mass Matrix for 3D Plates

In order to calculate the consistent mass matrix for 3D plates considering the drilling contribution, Guo (2012) presents further details. Mathematically, for a case of ρ constant and without offset, it follows:

$$\begin{aligned} \boldsymbol{M_e} = \iint_{\xi,\eta} \rho \Big(& h\boldsymbol{N^{u}}^T\boldsymbol{N^{u}} + h\boldsymbol{N^{v}}^T\boldsymbol{N^{v}} + h\boldsymbol{N^{w}}\boldsymbol{N^{w}} \\ & + \frac{h^3}{12}\boldsymbol{N^{r_x}}^T\boldsymbol{N^{r_x}} + \frac{h^3}{12}\boldsymbol{N^{r}}^T\boldsymbol{N^{r_y}} + h\boldsymbol{N^{r_z}}^T\boldsymbol{N^{r_z}} \Big) \det \boldsymbol{J} d\xi d\eta \end{aligned} \tag{4.133}$$

or for a more general case considering an offset of d and a ρ variable through the thickness:

$$\begin{aligned} \boldsymbol{M_e} = \iint_{\xi,\eta} \Bigg(& \int_{-\frac{h}{2}+d}^{+\frac{h}{2}+d} \rho \boldsymbol{N^{u}}^T\boldsymbol{N^{u}} dz + \int_{-\frac{h}{2}+d}^{+\frac{h}{2}+d} \rho \boldsymbol{N^{v}}^T\boldsymbol{N^{v}} dz + \int_{-\frac{h}{2}+d}^{+\frac{h}{2}+d} \rho \boldsymbol{N^{w}}^T\boldsymbol{N^{w}} dz \\ & \int_{-\frac{h}{2}+d}^{+\frac{h}{2}+d} \rho z \left(\boldsymbol{N^{u}}^T\boldsymbol{N^{r_y}} + \boldsymbol{N^{r}}^T\boldsymbol{N^{u}} \right) dz - \int_{-\frac{h}{2}+d}^{+\frac{h}{2}+d} \rho z \left(\boldsymbol{N^{v}}^T\boldsymbol{N^{r_x}} + \boldsymbol{N^{r}}^T\boldsymbol{N^{v}} \right) dz \\ & + \int_{-\frac{h}{2}+d}^{+\frac{h}{2}+d} \rho z^2 \boldsymbol{N^{r_x}}^T\boldsymbol{N^{r_x}} dz + \int_{-\frac{h}{2}+d}^{+\frac{h}{2}+d} \rho z^2 \boldsymbol{N^{r_y}}^T\boldsymbol{N^{r_y}} dz + \int_{-\frac{h}{2}+d}^{+\frac{h}{2}+d} \rho \boldsymbol{N^{r_z}}^T\boldsymbol{N^{r_z}} dz \Bigg) \det \boldsymbol{J} d\xi d\eta \end{aligned} \tag{4.134}$$

As explained by Brockman (1987):

- For dynamic analyses, “low- energy deformation patterns consisting mainly of hourglassing motions represent likely modes of low-frequency oscillations”; resulting in non-physical solutions that may contaminate that portion of the vibration spectrum which frequently is of greatest interest.

- The artificial stiffness associated with the hourglass modes are made small deliberately to avoid locking problems, being these modes orthogonal to the rigid-body and constant-strain states of interest.

- However, the kinetic energy of the hourglass modes is comparable to the rigid-body and uniform-strain motions.

- Consequently, artificial vibration modes whose frequency is governed exclusively by the generalized hourglass stiffness appear low in the element spectrum, intermixed with the lower-frequency vibration modes which are commonly of interest.

- This difficulty can be corrected by reducing or eliminating the kinetic energy associated with hourglass modes, while leaving the energy associated with rigid-body motions and uniform-strain states unchanged.

- The goal is to minimize the projection of the mass matrix on the hourglass modes of the element, so that they occur only at high frequencies, beyond the frequency range of interest.

4.3.6 Lumped Mass Matrix for 3D Plates

The lumped mass matrix for plates can be expressed as:

$$[M]_e = \begin{array}{c} \begin{matrix} u & v & w & r_x & r_y & r_z \end{matrix} \\ \begin{bmatrix} m_1 & & & & 0 & \\ & m_1 & & & & \\ & & m_1 & & & \\ & & & I_{yy_1} & & \cdots \\ & & & & I_{xx_1} & \\ & 0 & & \vdots & & I_{zz_1} \end{bmatrix} \end{array} \tag{4.135}$$

where m_i, I_{xx_i} and I_{zz_i} for $i = 1,2,3,4$ are the same ones defined for 2D model. The extra terms here are the I_{zz_1}, I_{zz_2}, I_{zz_3} and I_{zz_4}, which are given by:

$$I_{zz_1} = \int_{\eta=-1}^{\eta=0} \int_{\xi=-1}^{\xi=0} r_1^2 \rho h \det \boldsymbol{J} d\xi d\eta \tag{4.136}$$

$$I_{zz_2} = \int_{\eta=-1}^{\eta=0} \int_{\xi=0}^{\xi=+1} r_2^2 \rho h \det \boldsymbol{J} d\xi d\eta \tag{4.137}$$

$$I_{zz_3} = \int_{\eta=0}^{\eta=+1} \int_{\xi=0}^{\xi=+1} r_3^2 \rho h \det \boldsymbol{J} d\xi d\eta \tag{4.138}$$

$$I_{zz_4} = \int_{\eta=0}^{\eta=+1} \int_{\xi=-1}^{\xi=0} r_4^2 \rho h \det \boldsymbol{J} d\xi d\eta \tag{4.139}$$

where r_1^2, r_2^2, r_3^2 and r_4^2 are given by:

$$\begin{aligned} r_1^2 &= (x-x_1)^2 + (y-y_1)^2 \\ r_2^2 &= (x-x_2)^2 + (y-y_2)^2 \\ r_3^2 &= (x-x_3)^2 + (y-y_3)^2 \\ r_4^2 &= (x-x_4)^2 + (y-y_4)^2 \end{aligned} \tag{4.140}$$

4.4 Structural Implementation and Verification

Having all the theory presented in this chapter, it is possible to implement a structural module in Python to perform the structural analyses, that is, to obtain the mass and stiffness matrices, calculate the natural frequencies, obtain the vibration modes and perform the stress and strain analysis for the elements.

It is important to highlight that to use the structural module is necessary to verify it with another well-established reference. For this work, the verification was performed comparing the results to the ones obtained from Nastran, which in this case is executed on Femap with NX Nastran.

To make the verification, it is necessary to have a structure. At this moment, the structure chosen is the wing based on the FLEXOP project, which is presented in more details, including its dimensions, in Chapter 6 and Section 6.2.

To get started, it is presented a static analysis for two FLEXOP-wing-based models with 10 cross sections linearly spaced along the wingspan. The first and second model have an airfoil discretization of 8 and 20 points (nodes), respectively. This discretization defines the number of control points at each cross section and, consequently, the number of elements created by the Delaunay tessellation. More details regarding this design approach is presented in in Chapter 6 and Section 6.2. Fig. 26 depicts the truss-based structural mesh of the first and second models.

For the verification, the elements for both models are considered in Aluminum 7075 with Young's modulus of 71.7 GPa, Poisson ratio of 0.33, and density of 2795.7 kg/m^3. The truss elements have a diameter of 5 mm, and the plate elements of the skin have a thickness of 1 mm.

For the static analysis, the loads are obtained applying the DLM (see Chapter 3) and

Figure 26 – Truss-based structural meshes for 8 and 20 control points in each cross section, respectively.

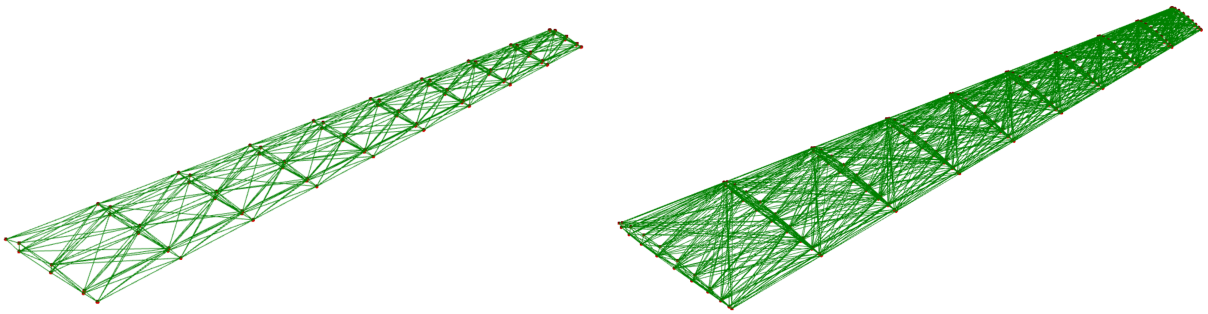

(a) 8 points spline. (b) 20 points spline.

Source: Elaborated by the author.

considering the same FLEXOP conventional cruise condition, i.e., a Mach number of 0.133 at altitude of 800 m. The aerodynamics loads are computed and applied to the first and second structural models. The deformed meshes are depicted in Fig. 27. In order to verify the results, the same analysis is performed in Nastran, and the comparison is available in Tab. 5.

Figure 27 – Static analysis for the first and second models, considering the FLEXOP cruise condition.

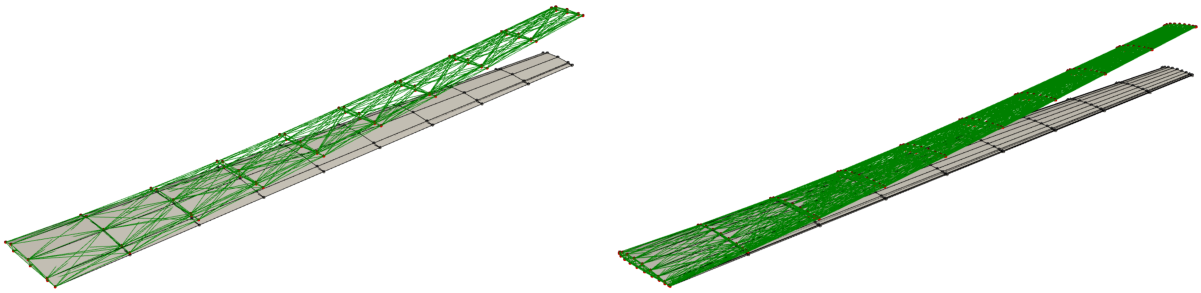

(a) First model - 8 nodes at each cross section. (b) Second model - 20 nodes at each cross section.

Source: Elaborated by the author.

Table 5 – Static analysis results and verification with Nastran.

	First model (8 points discretization)			Second model (20 points discretization)		
	Structural solver	Nastran	RE	Structural solver	Nastran	RE
u_{min} [m]	-0.00106	-0.00107	-1.12%	-0.0007633	-0.0007691	-0.76%
u_{max} [m]	0.002341	0.00237	-1.22%	0.001069	0.001073	-0.34%
v_{min} [m]	-0.00151	-0.00152	-0.61%	-0.0004409	-0.0004435	-0.59%
v_{max} [m]	0.001102	0.001124	-1.98%	0.0002640	0.0002662	-0.82%
w_{min} [m]	0	0	0.00%	0	0	0.00%
w_{max} [m]	0.2797	0.2849	-1.84%	0.09734	0.09793	-0.61%

The structural solver also computes the modal analysis for both wing structures. The first four modes for each model are depicted in Fig. 28. The natural frequencies obtained here are compared to the ones obtained from Nastran and displayed in Tab. 6. The first and second wing model has a total weight of **100.71 kg** and **318.62 kg**, respectively. It is worth mentioning that the first model has 345 truss elements and the second model has 937 elements.

Figure 28 – Modal analysis for first and second wing structural models.

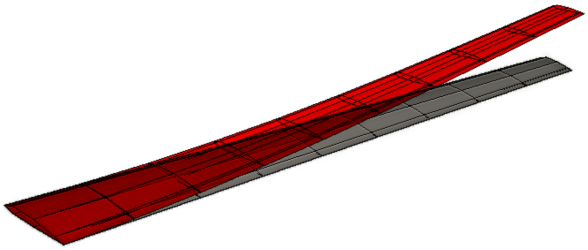

(a) First model - mode #1: 2.23 Hz.

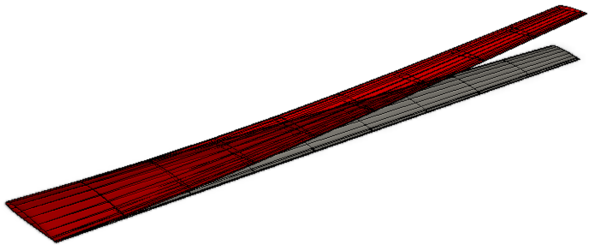

(b) Second model - mode #1: 2.07 Hz.

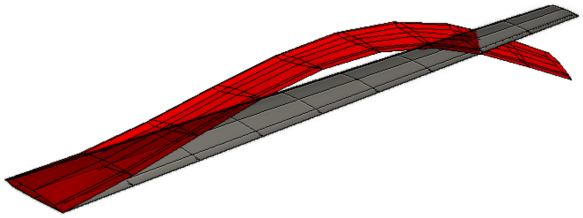

(c) First model - mode #2: 11.97 Hz.

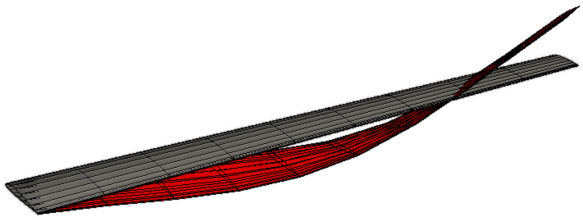

(d) Second model - mode #2: 11.29 Hz.

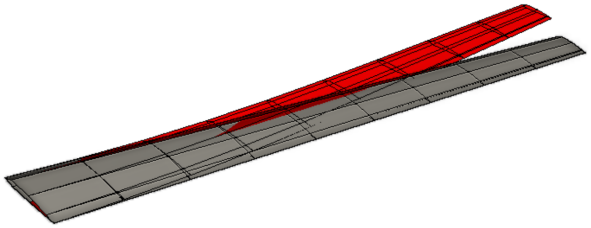

(e) First model - mode #3: 19.84 Hz.

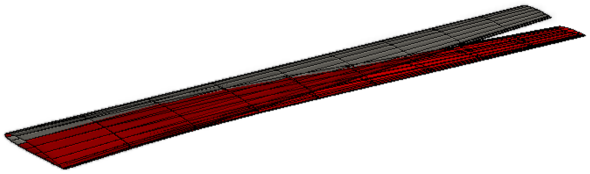

(f) Second model - mode #3: 19.54 Hz.

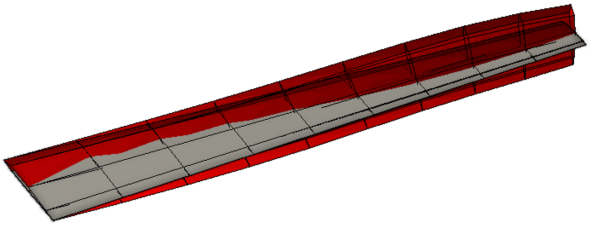

(g) First model - mode #4: 28.28 Hz.

(h) Second model - mode #4: 28.15 Hz.

Source: Elaborated by the author.

Table 6 – Natural frequencies verification with Nastran.

	First model (8 points discretization)			Second model (20 points discretization)		
	Structural solver	Nastran	RE	Structural solver	Nastran	RE
mode #1	2.23 Hz	2.27 Hz	-1.93%	2.07	2.09	-1.21%
mode #2	11.97 Hz	12.16 Hz	-1.63%	11.29	11.44	-1.43%
mode #3	19.84 Hz	20.40 Hz	-2.83%	19.54	20.03	-1.82%
mode #4	28.28 Hz	28.43 Hz	-0.29%	28.15	28.29.48	-0.12%

The results obtained by the presented implementation of the structural module in Python are in very good agreement with those obtained from Nastran. It is worth mentioning that the module `pyfe3d` has its own verification, which is available in Castro (2022a).

CHAPTER

5

AEROELASTIC MODELING

"Some fear flutter because they do not understand it.
And some fear it because they do"
— Theodore von Karman

AEROELASTICITY is the subject that studies the phenomena that result from the interactions between non-stationary aerodynamic flows and flexible structural systems. At the beginning of the last century, Lanchester began his studies in this area by analyzing the flutter phenomenon that occurred in a Handley-Page bomber biplane, mathematically equating it with the objective of minimizing the aeroelastic effects found in the structure. The multidisciplinarity of the subject can be visualized through the Collar's diagram (Fig. 29), also known as the diagram of the three rings.

Figure 29 – Collar's triangle.

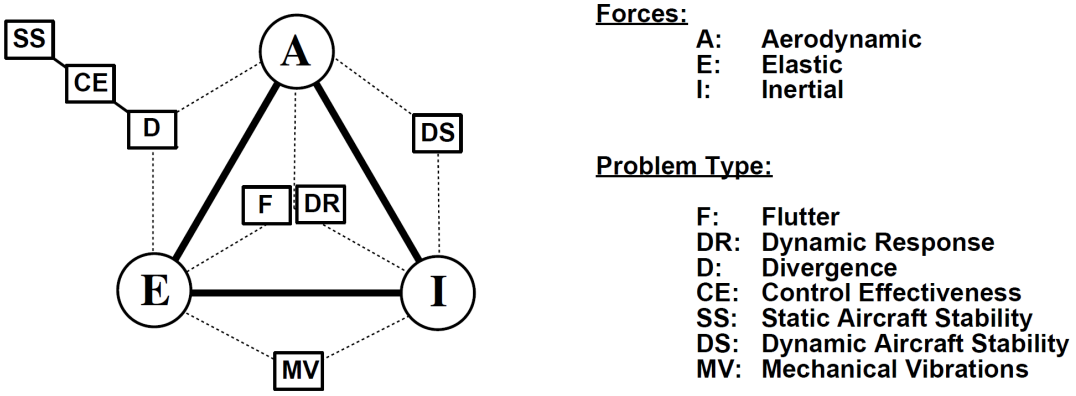

Source: Collar (1946).

Over the last decades, it has become common to further generalize the Collar's diagram, as supersonic aircraft designs still need to take into account the effects of thermal coupling. In addition, advanced control techniques are increasingly present to optimize the dynamic behavior of aerospace structures. These new problems are distributed in the areas of aeroservoelasticity and aerothermoelasticity (see Fig. 30).

Figure 30 – Friedmann's Hexahedron.

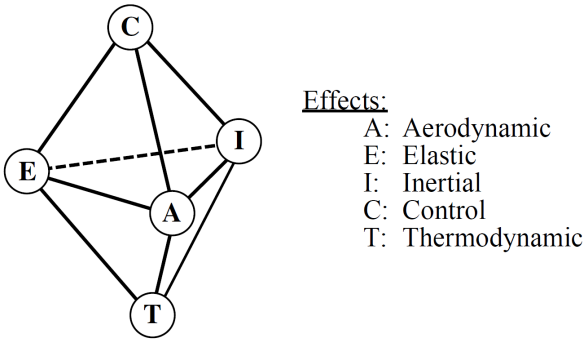

Source: Friedmann (1999).

This chapter is dedicated to the aeroelastic modeling of dynamic phenomena, in particular flutter. An attention to unsteady aerodynamic modeling discussed in Chapter 3 was especially helpful in designing a program for aeroelastic analysis. In this way, it is possible to establish total control over all aspects of the problem, from the aerodynamic basis and approximations made to the modeling of structural dynamics via finite elements and their coupling. In this chapter, aspects related to the construction of the aeroelastic problem for generalized structures, structural and aerodynamic coupling, and construction of generalized forces will be discussed.

5.1 Fundamentals of Structural Dynamics

The equations of motion of a linear structure discretized in N degrees of freedom can be represented, in matrix form, by Eq. (5.1), where the structural damping was neglected (CLOUGH; PENZIEN, 1975; MEIROVITCH, 1986)

$$[M]\{\ddot{x}(t)\} + [K]\{x(t)\} = \{L(x,\dot{x},t)\} \tag{5.1}$$

The matrices $[M]$ and $[K]$ are squares of order N and represent the matrices of mass and stiffness of the structure, respectively. The vectors $\{x(t)\}$ and $\{\ddot{x}(t)\}$ have dimension $N \times 1$ and represent

the displacements and accelerations suffered by the structure due to the application of external forces $\{L(x,\dot{x},t)\}$. In the particular case of an aircraft wing, which is the structure to be analyzed, $\{L(x,\dot{x},t)\}$ is the vector that represents the aerodynamic forces on the wing. An important characteristic of the aerodynamic force vector is that it not only depends on time, but also on the position of the wing in relation to the airflow and on the speed with which structural deformations occur.

The modes of vibration and the natural frequencies of the structure are obtained from the solution of the free vibration problem:

$$[M]\{\ddot{x}(t)\} + [K]\{x(t)\} = \{0\} \tag{5.2}$$

Assuming as a solution to Eq. (5.2) a simple harmonic motion in the form:

$$\{x(t)\} = \{\phi\}e^{i\omega t} \tag{5.3}$$

where ω is the frequency of the movement and $\{\phi\}$ is a vector representing the shape of the movement, it follows:

$$\left([K] - \omega^2[M]\right)\{\phi\} = \{0\} \tag{5.4}$$

which is an eigenvalue problem (MEIROVITCH, 1986), and its non-trivial solution is obtained for

$$\det\left([K] - \omega^2[M]\right) = 0 \tag{5.5}$$

Expansion of the determinant of Eq. (5.5) results in a polynomial equation of order N in ω^2 , also known as a characteristic polynomial. The roots of this equation correspond to the squares of the N natural frequencies of the structure.

The natural frequencies obtained then correspond to the eigenvalues of Eq. (5.4) and an eigenvector is associated with each one, which represents the vibration mode of the structure. Thus, substituting each value of ω in Eq. (5.4), the corresponding mode $\{\phi\}$ is obtained. However, Eq. (5.4) is homogeneous and has infinite solutions for $\{\phi\}$. Thus, the amplitudes of the vibration modes are indeterminate, but the shapes of these modes are unique, since $N-1$ components of the vector$\{\phi\}$ can be written as a function of another component, in a process known as normalization (MEIROVITCH, 1986). A very common type of normalization is to make the largest element of the vector $\{\phi\}$ equal to 1.

Having the modes of vibration determined, they can be grouped in the so-called modal matrix, given by the following:

$$[\Phi] = \begin{bmatrix} \{\phi\}_1 & \{\phi\}_2 & \{\phi\}_3 & \cdots & \{\phi\}_N \end{bmatrix} \tag{5.6}$$

The modal matrix will be used as a coordinate transformation matrix in the relation:

$$\{x(t)\} = [\Phi]\{\eta(t)\} = \sum_{r=1}^{N} \{\phi\}_r \eta_r(t) \tag{5.7}$$

where the vector $\{\eta(t)\}$ represents the displacements of the structure in a modal domain and can be understood as a vector of coefficients that determine the contribution of each mode of vibration in the physical response of the structure (CLOUGH; PENZIEN, 1975).

Since the modal matrix $[\Phi]$ is constant, the following relations are written:

$$\{\dot{x}(t)\} = [\Phi]\{\dot{\eta}(t)\} \tag{5.8}$$

$$\{\ddot{x}(t)\} = [\Phi]\{\ddot{\eta}(t)\} \tag{5.9}$$

Substituting Eqs. (5.7) and (5.9) in the equation of motion given by Eq. (5.1) and pre-multiplying all the terms obtained by $[\Phi]^T$, it follows:

$$[\Phi]^T[M][\Phi]\{\ddot{\eta}(t)\} + [\Phi]^T[K][\Phi]\{\eta(t)\} = [\Phi]^T\{L(x,\dot{x},t)\} \tag{5.10}$$

which can be rewritten in the form:

$$[\bar{M}]\{\ddot{\eta}(t)\} + [\bar{K}]\{\eta(t)\} = [\Phi]^T\{L(x,\dot{x},t)\} \tag{5.11}$$

where $[\bar{M}] = [\Phi]^T[M][\Phi]$ and $[\bar{K}] = [\Phi]^T[K][\Phi]$ are called modal mass and stiffness matrices, respectively.

An important property of vibrating modes is orthogonality. For two distinct modes of vibration $\{\phi\}_r$ and $\{\phi\}_s$, it is verified that the following Eqs. (5.12) and (5.13) are valid (MEIROVITCH, 1986). The proof of these equations is based on the fact that the mass and stiffness matrices are symmetrical, which is a characteristic of linear structures.

$$\{\phi\}_r^T[M]\{\phi\}_s = 0 \tag{5.12}$$

$$\{\phi\}_r^T [K] \{\phi\}_s = 0 \tag{5.13}$$

Based on the orthogonality properties, it can be concluded that the matrices $[\bar{M}]$ and $[\bar{K}]$ are diagonal and therefore the system of N simultaneous equations represented in Eq. (5.1) reduces to N independent equations of motion, each one representing the equation of movement of a structure with a single degree of freedom, whose solution can be obtained much more easily. Considering a certain mode r, then $\omega_r^2 = \dfrac{\bar{K}_r}{\bar{M}_r}$. This technique of decoupling the equations of motion is known as modal superposition (CLOUGH; PENZIEN, 1975), since the physical response of the structure is obtained by a superposition of modal solutions (according to Eq. (5.7)).

Using a special type of normalization in the process of obtaining the eigenvectors, defined in Eq. (5.14), the modal mass matrix $[\bar{M}]$ is equal to the identity matrix and the modal stiffness matrix is reduced to a diagonal matrix containing the natural frequencies squared. Eq. (5.11) can then be written in the form of Eq. (5.15).

$$[\Phi] = [\bar{\Phi}][\bar{M}]^{-1/2} \tag{5.14}$$

$$\{\ddot{\eta}(t)\} + \left[\omega^2\right] \{\eta(t)\} = [\Phi]^T \{L(x,\dot{x},t)\} \tag{5.15}$$

Observing Eq. (5.15), it can be concluded that to represent the dynamics of a structure it may only be necessary to know its natural frequencies and its modes of vibrating. However, these characteristics depend on the mass and stiffness matrices, which in turn are dependent on the discretization process adopted for the structure. For complex structures, such as an airplane wing, the most used tool in the discretization process is the finite element method, which is the approach of this work and presented in Chapter 4.

5.2 Coupling of Structural and Aerodynamic Models

The first difficulty that arises in the assembly of the equation of motion of the aeroelastic system is due to the fact that the modes of vibration and the aerodynamic forces are calculated

using different discretization methods. To solve this problem, it is necessary that the aerodynamic forces applied to points of the aerodynamic mesh are converted to points of the structural mesh and that the displacements suffered by points of the structural mesh are transferred to the aerodynamic mesh. This exchange of information between the meshes can be represented by a coordinate transformation matrix, as shown in Eq. (5.16), where the subscript a refers to the aerodynamic mesh, the subscript e refers to the structural mesh and the matrix $[G]$ represents the transformation matrix.

$$\{x\}_a = [G]\{x\}_e \tag{5.16}$$

The same transformation matrix can be used to convert the vibration modes obtained in the structural coordinates to the aerodynamic coordinates, such as:

$$[\Phi]_a = [G][\Phi]_e \tag{5.17}$$

Since the forces represented in the structural coordinate system must be structurally equivalent to the forces represented in the aerodynamic coordinate system, the virtual work done by these forces must be equal:

$$\{\delta x\}_a^T \{L\}_a = \{\delta x\}_e^T [G]^T \{L\}_a = \{\delta x\}_e^T \{L\}_e \tag{5.18}$$

As the virtual displacements are arbitrary, it follows:

$$\{L\}_e = [G]^T \{L\}_a \tag{5.19}$$

which represents the transformation between the involved forces represented in the two systems.

The equation of motion (5.15) can then be rewritten in the form:

$$\{\ddot{\eta}(t)\} + \left[\omega^2\right] \{\eta(t)\} = [\Phi]_e^T [G]^T \{L(\eta, \dot{\eta}, t)\}_a \tag{5.20}$$

Substituting Eq. (5.17) into (5.20), it follows:

$$\{\ddot{\eta}(t)\} + \left\lfloor\omega^2\right\rfloor \{\eta(t)\} = [\Phi]_a^T \{L(\eta, \dot{\eta}, t)\}_a \tag{5.21}$$

which represents the equation of motion of the aeroelastic system with the external forces obtained in the aerodynamic mesh and converted to the structural mesh.

It is observed that this conversion between the meshes was done by pre-multiplying the vector of aerodynamic forces by the transpose of the matrix of modes of vibration written in the aerodynamic coordinates. The most popular method to obtain this matrix is the interpolation by surface splines, developed by Harder and Desmarais (1972) and described in the next section.

An important point to note is that the matrix of modes of vibration written in aerodynamic coordinates depends on the set of points chosen to represent the aerodynamic mesh. When the objective is to transfer the forces obtained in the aerodynamic mesh to the structural mesh, this set of points must be formed by the points where the aerodynamic forces are defined. These points are the control points, located in the center of each vortex ring and are represented by the vector $\{x\}_a$. The transformation of the coordinates between this set of points and the structural mesh is given by the matrix $[G]$ used above.

5.3 Interpolation by Surface Spline

The surface spline interpolation procedure is one of the methods used to determine the structural deformations at aerodynamic points, that is, points on which the aerodynamic loading is calculated. This method is based on the solution of the equation for small deformations of an infinite flat plate, given by

$$D\nabla^4\{w\} = D\frac{1}{r}\frac{d}{dr}\left\{r\frac{d}{dr}\left[\frac{1}{r}\frac{d}{dr}\left(r\frac{d\{w\}}{dr}\right)\right]\right\} = \{P\} \tag{5.22}$$

where D is the stiffness of the plate, $\{w\}$ is the displacement vector and $\{P\}$ is the vector of forces applied to the plate.

The application of this method in aeroelastic analyzes aims to make the solution of Eq. (5.22) reproduce the displacements from a structural mesh in an aerodynamic mesh. Considering a structural mesh with n points (x_i, y_i) and known displacements w_i, it is necessary to find the forces that must be applied in these n points to reproduce the structural displacements.

The solution of Eq. (5.22) for a force applied at the origin of the plate is given by Eq. (5.23), written in terms of the polar coordinate r, where A and B are coefficients that need to be determined and P is the applied force (HARDER; DESMARAIS, 1972).

$$w(r) = A + Br^2 + \frac{P}{16\pi D}r^2\ln r^2 \tag{5.23}$$

An arbitrary deformation of the plate can be achieved by summing the solutions given by Eq. (5.23) at the n points of the structural mesh. This sum is given by:

$$w(x,y) = \sum_{i=1}^{n} \left[A_i + B_i r_i^2 + \frac{P_i}{16\pi D} r_i^2 \ln r_i^2 \right] \tag{5.24}$$

where

$$r_i^2 = (x - x_i)^2 + (y - y_i)^2 \tag{5.25}$$

A more usual way to represent Eq. (5.24) is given by:

$$w(x,y) = a_0 + a_1 x + a_2 y + \sum_{i=1}^{n} F_i r_i^2 \ln r_i^2 \tag{5.26}$$

where

$$F_i = \frac{P_i}{16\pi D} \tag{5.27}$$

The derivative of Eq. (5.26) gives the local slope, given by:

$$\frac{\partial w}{\partial x} = a_1 + 2 \sum_{i=1}^{n} (x - x_i) \left[1 + \ln \left(r_i^2 \right) \right] F_i \tag{5.28}$$

The solution of Eq. (5.26) involves the determination of $n+3$ coefficients a_0, a_1, a_2, F_i, which are obtained from the following equations:

$$\sum_{i=1}^{n} F_i = 0 \tag{5.29}$$

$$\sum_{i=1}^{n} F_i x_i = 0 \tag{5.30}$$

$$\sum_{i=1}^{n} F_i y_i = 0 \tag{5.31}$$

$$w_j = a_0 + a_1 x_j + a_2 y_j + \sum_{i=1}^{n} \kappa_{ij} F_i, \quad j = 1, 2, \ldots, n \tag{5.32}$$

where

$$\kappa_{ij} = r_{ij}^2 \ln \left(r_{ij}^2 \right) \tag{5.33}$$

$$r_{ij}^2 = \left(x_j - x_i \right)^2 + \left(y_j - y_i \right)^2 \tag{5.34}$$

Equations (5.29) to (5.34) constitute a linear system and can be written in matrix form as expressed in Eq. (5.35), described in the work of Silva (1994) and in Aeroelastic Analysis User's Guide of MSC Nastran (2021).

$$\begin{Bmatrix} 0 \\ 0 \\ 0 \\ w_1 \\ w_2 \\ \vdots \\ w_j \\ \vdots \\ w_n \end{Bmatrix} = \begin{bmatrix} 0 & 0 & 0 & 1 & 1 & \cdots & 1 & \cdots & 1 \\ 0 & 0 & 0 & x_1 & x_2 & \cdots & x_j & \cdots & x_n \\ 0 & 0 & 0 & y_1 & y_2 & \cdots & y_j & \cdots & y_n \\ 1 & x_1 & y_1 & \kappa_{11} & \kappa_{12} & \cdots & \kappa_{1j} & \cdots & \kappa_{1n} \\ 1 & x_2 & y_2 & \kappa_{21} & \kappa_{22} & \cdots & \kappa_{2j} & \cdots & \kappa_{2n} \\ \vdots & \vdots & \vdots & \vdots & \vdots & \ddots & \vdots & \ddots & \vdots \\ 1 & x_j & y_j & \kappa_{j1} & \kappa_{j2} & \cdots & \kappa_{jj} & \cdots & \kappa_{jn} \\ \vdots & \vdots & \vdots & \vdots & \vdots & \ddots & \vdots & \ddots & \vdots \\ 1 & x_n & y_n & \kappa_{n1} & \kappa_{n2} & \cdots & \kappa_{nj} & \cdots & \kappa_{nn} \end{bmatrix} \begin{Bmatrix} a_0 \\ a_1 \\ a_2 \\ F_1 \\ F_2 \\ \vdots \\ F_j \\ \vdots \\ F_n \end{Bmatrix} \tag{5.35}$$

The steps to obtain the displacements in the system of interest, from this formulation, are as follows. Initially, the displacements of the structural modes given by w_i are known, which are the components in the z_i direction of cartesian system, used in the definition of the structural coordinate system. Other known values are the coordinates of the points on which the structural displacements are defined, given by x_i and y_i. The κ_{ij} values are obtained by applying the known x_i and y_i coordinates, according to Eq. (5.35). The algebraic solution of this system will provide as an answer the values of the coefficients a_0, a_1, and a_2 as well as F_1 to F_n. With these values, it is possible to write the function given by Eq. (5.26) for displacements, and (5.28) for slopes, and thus represent the displacements and structural slopes at points of the aerodynamic mesh.

5.4 Generalized Matrices

From Chapter 3, the aerodynamic loading can be expressed as:

$$\{L_a(ik)\} = q_\infty [S] \left\{\Delta C_p(ik)\right\} \tag{5.36}$$

where q_∞ is the dynamic pressure, $[S]$ is a matrix that represents the areas of the panels of the aerodynamic mesh, and $\left\{\Delta C_p(ik)\right\}$ is the vector of pressure coefficients obtained from the Doublet-Lattice Method (DLM). Furthermore, Eq. (5.36) can also be written as:

$$\{L_a(ik)\} = q_\infty [S][AIC(ik)]\{w(ik)\} \tag{5.37}$$

where $[AIC(ik)]$ is the matrix of aerodynamic influence coefficients and $\{w(ik)\}$ is the vector of downwash, which can be expressed in frequency domain as:

$$\{w(x,y,0,ik)\} = \frac{\partial h(x,y,0)}{\partial x} + ikh(x,y,0) = [F(ik)]\{h(x,y,0)\} \tag{5.38}$$

where $\{h\}$ is the vector of displacements of the aerodynamic panels, and $[F(ik)]$ is an operator that represents the substantial derivative of the mode of motion, given by:

$$[F(ik)](\cdot) = \left[\frac{\partial(\cdot)}{\partial x} + ik(\cdot)\right] \tag{5.39}$$

Therefore, the aerodynamic loading can be written in terms of the displacements of the aerodynamic panels, such as:

$$\{L_a(ik)\} = q_\infty[S][AIC(ik)][F(ik)]\{h\} \tag{5.40}$$

Furthermore, the aerodynamic loading that, a priori, was calculated at points defined by an aerodynamic mesh can be represented at the points that define the structural mesh by:

$$\left\{L_a^{str}(x_s,y_s,z_s,ik)\right\} = q_\infty[G]^T[S][AIC(ik)][F(ik)][G]\left\{u(x_s,y_s,z_s)\right\} \tag{5.41}$$

where the subscript s refers to structural mesh and $[G]$ represents the transformation of the displacements defined at the model nodes in finite elements for the control points of the aerodynamic panels, and it is calculated from the surface spline.

Similarly, the generalized aerodynamic loading $[Q]$, that is, the loading on the j-th modal basis, is given by:

$$[Q(ik)] = [\Phi_a]^T[G]^T[S][\mathrm{AIC}(ik)][F(ik)][G][\Phi_a] \tag{5.42}$$

where $[\Phi_a]$ corresponds to the j-th mode of vibration of the structure, obtained through the solution of eigenvalue and eigenvector of the FEM code. Eq. (5.42) represents the calculation of the so-called generalized aerodynamic matrix (GAM).

The generalized equation of motion is expressed in terms of the modal coordinates q, since $\delta = \Phi q$, where Φ is the modal matrix. Then, Eq. (5.1) can be expressed as:

$$\left[M_q\right]\{\ddot{q}\} + \left[K_q\right]\{q\} = \frac{\rho V^2}{2}[Q]\{q\} \tag{5.43}$$

where $\{q\} = \{h_{\mathrm{modal}}\}$.

The generalized aerodynamic forces matrix (GAM) is a complex matrix as a function of Mach and reduced frequency, derived from the matrix $[AIC]$, and reduced on the modal basis. Aeroelastic analysis assumes that complex loading can be separated into real and imaginary terms, denoting, respectively, the aerodynamic influence on damping and stiffness of the system. In this way, Eq. (5.43) can be rewritten in terms of the real and imaginary part of the matrix, $[Q]$, such as:

$$\left[M_q\right]\{\ddot{q}\} + \left[K_q\right]\{q\} = \frac{\rho V}{2}[Q_I]\{\dot{q}\} + \frac{\rho V^2}{2}[Q_R]\{q\} \tag{5.44}$$

Equation (5.44) is the aeroelastic equation of the system described in modal coordinates. It can be represented in the classic aeroelastic form described by Wright and Cooper (2014) as:

$$\boldsymbol{A}\ddot{q} + \rho V \boldsymbol{B}\dot{q} + \left(\rho V^2 \boldsymbol{C} + \boldsymbol{E}\right) q = 0 \tag{5.45}$$

where $\boldsymbol{A}$ is the modal mass matrix, $\boldsymbol{B}$ the aerodynamic damping matrix due to flow, $\boldsymbol{C}$ the aerodynamic stiffness matrix and $\bar{\boldsymbol{E}}$ the structural stiffness matrix, with the aerodynamic terms being reduced frequency dependent.

5.5 Flutter Prediction Methods

The aeroelastic analysis has as main objective to establish the velocity range in which the aircraft, or any other system under analysis, is free from aeroelastic phenomena. To determine this so-called flight envelope, it is necessary to establish a mathematical procedure by which the critical flutter velocity is calculated.

As discussed in the preceding chapters, aerodynamic forces are usually presented by functions dependent on the dimensionless parameter reduced frequency (k). In this way, it becomes appropriate to present the equations of motion associated with the model as a typical problem of eigenvalues and eigenvectors. With this frequency domain approach, relationships are defined between the eigenvalues of the dynamic matrix and the reduced frequency carried by the aerodynamic parts.

In order to establish this relationship and provide an approximation of the flutter velocity, two classic methods of aeroelastic stability analysis are highlighted: k and p-k method (WRIGHT;

COOPER, 2014). The last method is the most used and also presents several derivations in the literature, where methodologies mainly of numerical nature were implemented in order to improve the accuracy of the estimation of the flutter velocity or of the prediction of relative damping, in addition to including methodologies for achieve convergence of values more efficiently.

In both of the aforementioned methods, it is desired to draw the classical stability analysis diagrams, known as *v-g-f diagrams* (velocity, damping, frequency). In these diagrams, it is possible to observe the evolution of frequencies and damping factors of each mode of the structure as a function of velocity. The critical velocity is that which is associated with a change in the sign of the damping factor. In these regions, it is usual to observe the coalescence of the frequencies of two of the most aeroelastic modes of the structure, characterizing the occurrence of the flutter phenomenon.

5.5.1 p-k Method

The *p-k* method consists of an iterative process that allows obtaining the velocity, frequency and damping values of the model. It is noteworthy that, since there is no substitution or introduction of a parameter, as in the *k* method, the damping curve has a physical value, which makes this approach more suitable to base, for example, stability analyzes that will serve as a basis for experimental compositions.

The starting point is to treat the aeroelastic Eq. (5.43) as a nonlinear eigenvalue problem, assuming that $p \equiv d/dt$. Thus, $\ddot{q} = p^2 q$:

$$\left(p^2 \left[M_q\right] + \left[K_q\right] - \frac{\rho V^2}{2}[Q(k)] \right) \{q\} = 0 \tag{5.46}$$

For a non-trivial solution, the so-called flutter determinant is evaluated in the form:

$$\left| p^2[I] + \left[M_q\right]^{-1} \left(\left[K_q\right] - \frac{\rho V^2}{2}[Q(k)] \right) \right| = 0 \tag{5.47}$$

Equation. (5.47) presents two unknowns to be solved, p and k, requiring another equation for its solution. In such a way, p^2 is an eigenvalue of the matrix given by:

$$\left[M_q\right]^{-1} \left(\left[K_q\right] - \frac{\rho V^2}{2}[Q(k)] \right) \tag{5.48}$$

where $k = \dfrac{\omega b}{V}$. Taking that the imaginary part of the eigenvalue is the frequency, the second necessary equation is:

$$\mathrm{Im}(p) = k\frac{V}{b} \tag{5.49}$$

The problem is to determine an eigenvalue and a frequency that satisfies both Eqs. (5.47) and (5.49). The solution to these equations is obtained iteratively, where initially a value for the frequency k is estimated, usually based on the natural frequencies of the structure, and then calculating p from the eigenvalue problem of Eq. (5.47). The values of p and k must then satisfy Eqs. (5.47) and (5.49), otherwise, the value of k is changed until the convergence of the calculation occurs.

Usually, to facilitate the solution of the flutter determinant, Eq. (5.47) is rewritten in state space form, making the order of the system to double. Thus, Eq. (5.47) becomes:

$$[A] = \begin{bmatrix} [0] & [I] \\ -\left[M_q\right]^{-1}\left(\left[K_q\right] - \dfrac{\rho V^2}{2}[\mathrm{Re}(Q)]\right) & -\left[M_q\right]^{-1}\left(-\dfrac{1}{4}\rho c V\dfrac{\mathrm{Im}(Q)}{k}\right) \end{bmatrix} \tag{5.50}$$

The solution to the problem given by Eq. (5.50) generates eigenvalues in the form:

$$p = \omega\left(\frac{g}{2} \pm i\right) \tag{5.51}$$

where

$$\omega = \mathrm{Im}(p) \tag{5.52}$$

$$g = \frac{2\,\mathrm{Re}(p)}{\mathrm{Im}(p)} \tag{5.53}$$

In this case, the damping g obtained is considered a more real solution, since the damping is considered small and is obtained from the equality of the imaginary parts, taking into account the modified equation of the *p-k* method. The convergence for the k values obtained must meet a stopping criterion evaluated by the absolute error between the frequencies, so that:

$$\begin{aligned} \left|k_s^{(j)} - k_s^{(j-1)}\right| < \varepsilon \quad &\rightarrow k_s^{(j-1)} < 1 \\ \left|k_s^{(j)} - k_s^{(j-1)}\right| < \varepsilon k_s^{(j-1)} &\rightarrow k_s^{(j-1)} \geq 1 \end{aligned} \tag{5.54}$$

where the superscript j represents the j-th iteration, and the subscript s is the reduced frequency evaluated by each mode, and ε is the tolerance value, usually used as 0.001 (RODDEN; JOHNSON, 1994).

The complete procedure of the *p-k* method is graphically illustrated by the flowchart in Fig. 31 and summarized in the following steps:

Figure 31 – Flow diagram of *p-k* method.

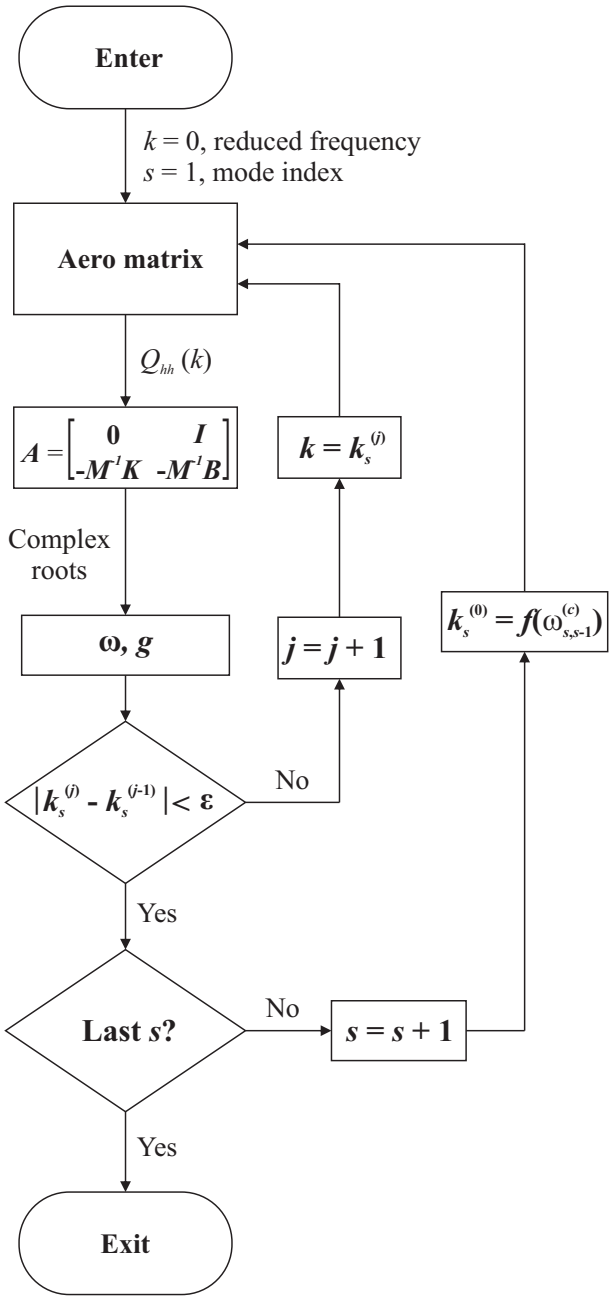

Source: Elaborated by the author.

i Select the range of velocities of interest.

ii For each V value analysis, follow the steps listed below for each mode:

a) Evaluate $[Q(k_n^j)]$. As a first estimate for k_n^j, it is used the natural frequencies of the structures, and then the converged reduced frequency values from previous steps are used. The superscript j and subscript n correspond to the aeroelastic mode and the iteration step, respectively.

b) Solve the eigenvalue problem defined in Eq. (5.50) and determine the new $p_{n+1}^j = \omega_{n+1}^j \left(\gamma_{n+1}^j + i\right)$ and $k_{n+1}^j = \frac{\omega_{n+1}^j b}{V}$.

c) Check the convergence criterion, i.e., $\left|k_{n+1}^j - k_n^j\right| < \varepsilon$.

d) If the convergence criterion is satisfied, terminate the iterations. Otherwise, repeat steps (a) to (c) using the new value of the reduced frequency, i.e., k_{n+1}^j.

iii Plot ω vs V curves for each aeroelastic mode.

iv Using g vs V and ω vs V curves, estimate the flutter speed V_{flutter} for which $g = 0$ at one of the modes, and the corresponding flutter frequency ω_f.

5.5.2 Interpolation of Generalized Aerodynamic Matrices

In a typical flutter analysis, the calculation of generalized aerodynamic matrices represents a large part of the computational cost required for the solution. As discussed throughout this work, these matrices are dependent on the reduced frequency and Mach number, being calculated for discrete values of these parameters. In methods of aeroelastic analysis in the frequency domain, such as the *p-k* method, other velocities are evaluated; therefore, other reduced frequencies are required, which are different from those previously calculated for the aerodynamic matrices.

These intermediate values are usually obtained through an interpolation of the calculated available values. This approach has been implemented in several commercial codes for aeroelastic solutions, such as ZAERO and Nastran. Among the most used methods for interpolation of aerodynamic matrices are linear spline, surface spline, and special linear interpolation. The last one is the approach adopted in this work and presented below.

For the *p-k* method, the generalized aerodynamic matrix can be interpolated using the form:

$$\boldsymbol{Q}_{hh}(k_{est}) = \sum_{j=1}^{nhdpts} C_j \left[\boldsymbol{Q}_{hh}^R(k_j) + \frac{i}{k_j}\boldsymbol{Q}_{hh}^I(k_j)\right] \tag{5.55}$$

where $\frac{\boldsymbol{Q}^I_{hh}}{k_j}$ is fit rather than $\boldsymbol{Q}^I_{hh}$ directly since the former quantity is a much smoother value of k and because it is needed in the formulation of Eq. (5.50). Further, this makes the response data symmetric with respect to a reduced frequency of zero and this "boundary condition" can be applied in the interpolation.

The vector C of Eq. (5.55) is calculated as:

$$\{C\} = [A]^{-1}\{B\} \tag{5.56}$$

with

$$A_{ij} = \begin{cases} \left|k_i - k_j\right|^3 + \left|k_i + k_j\right|^3 & \text{for } i \text{ and } j \leq nhdpts \\ 0 & \text{for } i = j = nhdpts+1 \\ 1 & \text{for } i = nhdpts+1 \text{ or } j = nhdpts+1 \end{cases} \tag{5.57}$$

$$B_i = \begin{cases} |k_{est} - k_i|^3 + |k_{est} + k_i|^3 & \text{for } i \leq nhdpts \\ 1 & \text{for } i = nhdpts+1 \end{cases} \tag{5.58}$$

where $nhdpts$ is the number of hard points (i.e., points at which $\boldsymbol{Q}_{hh}$ has been calculated), k_i are the reduced frequency values for these points, and k_{est} is the reduced frequency value to which the aerodynamics are to be interpolated.

In contrast, the local curve fit approach solves for the coefficients C of the following equations:

$$\begin{bmatrix} 1 & k_1 & k_1^2 & \cdots & k_1^{N-1} \\ 1 & k_2 & k_2^2 & \cdots & k_2^{N-1} \\ . & . & . & & . \\ . & . & . & & . \\ 1 & k_N & k_N^2 & \cdots & k_N^{N-1} \end{bmatrix} \begin{Bmatrix} C^R_{ij1} \\ C^R_{ij2} \\ . \\ . \\ C^R_{ijN} \end{Bmatrix} = \begin{Bmatrix} Q^R_{ij1} \\ Q^R_{ij2} \\ . \\ . \\ Q^R_{ijN} \end{Bmatrix} \tag{5.59}$$

and

$$\begin{bmatrix} 1 & k_1 & k_1^2 & \cdots & k_1^{N-1} \\ 1 & k_2 & k_2^2 & \cdots & k_2^{N-1} \\ . & . & . & & . \\ . & . & . & & . \\ 1 & k_N & k_N^2 & \cdots & k_N^{N-1} \end{bmatrix} \begin{Bmatrix} C^I_{ij1} \\ C^I_{ij2} \\ . \\ C^I_{ijN} \end{Bmatrix} = \begin{Bmatrix} \frac{1}{k_1} Q^I_{ij1} \\ \frac{1}{k_2} Q^I_{ij2} \\ \vdots \\ . \\ \frac{1}{k_N} Q^I_{ijN} \end{Bmatrix} \tag{5.60}$$

where the real and imaginary parts of $\boldsymbol{Q}_{hh}$ are independently by N^{th} order polynomials. Therefore, the terms of the generalized aerodynamic matrix are then obtained as:

$$Q_{ij}(k_{est}) = \sum_{l=1}^{N} C^R_{ijl} k_{est}^{l-1} + i \sum_{l=1}^{N} C_{ijl} k_{est}^{l-1} \tag{5.61}$$

5.6 Aeroelastic Integration and Code Implementation

At this point, all the necessary tools for the wing design have already been developed, i.e., there is a aerodynamic module (see Chapter 3) based on the Doublet-Lattice Method, which provides the unsteady subsonic loads, also there is a FEM module (see Chapter 4), which models the wing's structures (truss and skin), and finally there is a aeroelastic module, which makes the coupling between the structural and aerodynamic modules. Since the structural module have already been implemented in Python by Castro (2022a), so the other modules were entirely coded in Python as well. Therefore, the structure of coding is organized as depicted in Fig. 32.

The structural module groups all the subroutines related to the structural dynamics analysis of the problem. In this module, the finite element code (FEM) is implemented for the truss-based wing modeling, providing all the structural response of the system. The information generated by the code is archived to be used together with the aerodynamic outputs in the aeroelastic solution. Data referring to the finite element mesh, modal displacements and natural frequencies of the structure from the modal analysis are archived for each evaluated mode. The implemented finite element code was verified by comparing the results obtained by Nastran (see Chapter 4, Section 4.4).

The aerodynamic module comprises the entire aerodynamic modeling formulation discussed in Chapter 3. This module comprises a large part of the effort employed in this work to solve aeroelastic problems, and is composed of subroutines dedicated to performing the calculation of various aspects of the problem. These modules were implemented in order to be executed separately from the aeroelastic problem, thus facilitating the calculation and verification of the implemented DLM, providing only steady or unsteady aerodynamic loading.

Initially, the aerodynamic parameters of operation are defined by the input routine. In this routine, the reduced frequencies to be evaluated, the Mach, the aerodynamic mesh discretization mode and the definition of the surface geometry are defined. Once the input parameters are defined, the aerodynamic influence matrices are computed for each specified reduced frequency, by defining the points of interest (doublet line for the DLM) in the AIC matrix calculation routine. The unsteady load generation code was verified as presented in Chapter 3, Section 3.2.

Figure 32 – Flow diagram of modules integration.

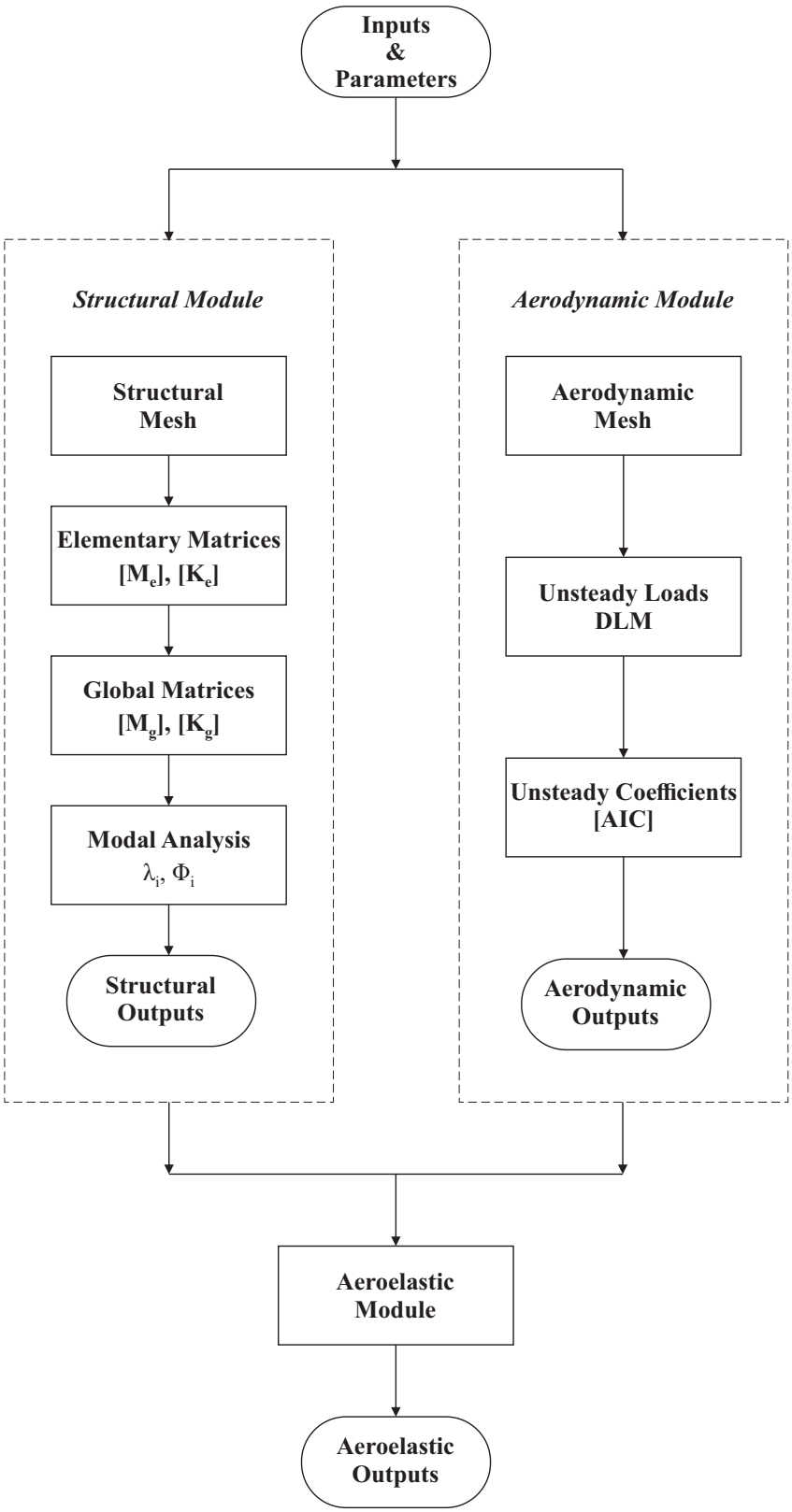

Source: Elaborated by the author.

Finally, in order to proceed to the aeroelastic analysis, generalized aerodynamic matrices are computed. The generalized matrix calculation routine uses the interpolation of the modal displacements obtained in the structural module of the wing to perform the reduction to modal basis and consequent formulation of the generalized equations of motion. The aeroelastic analyzes are performed from the interpolations and the solution of the p-k method presented earlier in the previous sections of this chapter (see Fig. 31). The output files, containing the velocities, frequencies, and damping are generated and used to plot the v-g-f diagrams. The aeroelastic verification is presented in the next section.

5.7 Aeroelastic Verification

This section brings the aeroelastic verification of the approach presented along the last sections and presented in Figs. 31 and 32. To do so, it is necessary to have a wing model. For this case, the objective was to highlight the bending and torsion modes, in order to allow a better aeroelastic coupling between them, thus obtaining a lower flutter velocity, which would allow a better visualization of the flutter velocity in the v-g-f diagram, enabling the aeroelastic verification.

Thus, it is assumed a wing model with the following dimensions listed in Tab. 7. Furthermore, the truss-based wing is meshed with 16 control points (nodes) in each cross sections and 10 cross sections linearly spaced along the wingspan. The mesh is created based on Delaunay tessellation, which is presented in more details in Section 6.1.1. The aerodynamic mesh, in turn, is discretized assuming 10 panels in x-direction and 30 panels in y-direction. Thus, the following structural and aerodynamic meshes are obtained, which are depicted in Figs. 33 and 34.

Table 7 – Geometric parameters for the FLEXOP reference wing.

Parameter	Value
Aerodynamic profile	NACA 2412
Inboard leading edge, (x,y,z) [m]	(0,0,0)
Inboard trailing edge, (x,y,z) [m]	(1.0,0,0)
Outboard trailing edge, (x,y,z) [m]	(1.3,3.5,0)
Outboard leading edge, (x,y,z) [m]	(0.5,3.5,0)

Source: Elaborated by the author.

Figure 33 – Structural mesh of truss-based wing model for the aeroelastic verification.

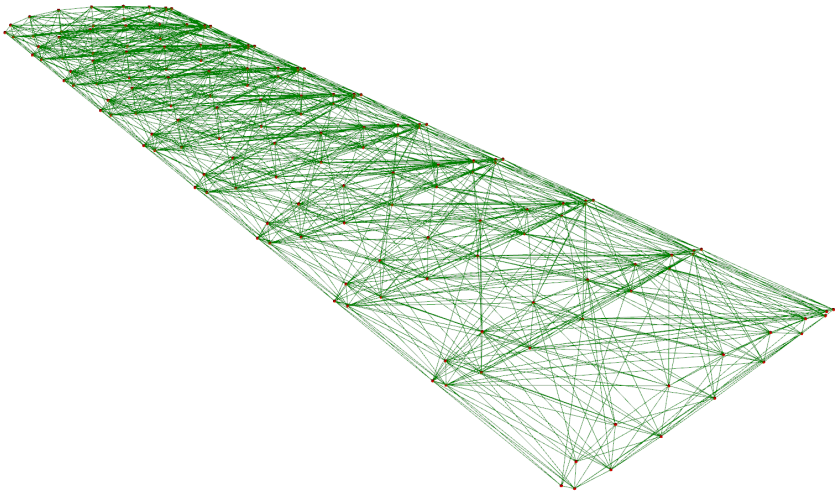

Source: Elaborated by the author.

Figure 34 – Aerodynamic mesh for the aeroelastic verification.

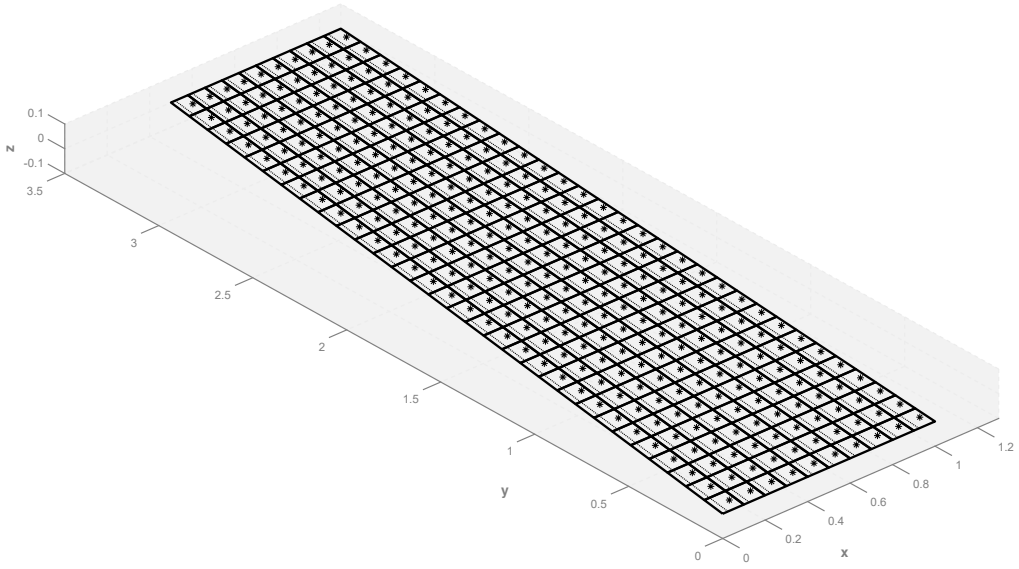

Source: Elaborated by the author.

For the aeroelastic verification, the truss elements are considered in Aluminum 7075 with Young's modulus of 71.7 GPa, Poisson ratio of 0.33, and density of 2795.7 kg/m^3. The truss elements have a solid diameter of 5 mm, and the plate elements of the skin have a thickness of 1 mm.

Therefore, the first analysis is the modal analysis, which is performed by the structural module. The values obtained are compared with the same analysis performed in Nastran and

listed in Tab. 8. For convenience, only the first five modes are listed here. There is a good correlation between the results obtained by the present code and those from Nastran. Also, for better visualization, the first five modes are illustrated in Fig. 35.

Table 8 – Results from modal analysis.

	Structural Module	Nastran	RE
mode #1	4.19 Hz	4.27 Hz	-1.93%
mode #2	17.22 Hz	17.49 Hz	-1.63%
mode #3	23.18 Hz	23.84 Hz	-2.83%
mode #4	39.91 Hz	40.02 Hz	-0.29%
mode #5	47.57 Hz	49.39 Hz	-3.83%

Figure 35 – First five modes for the wing model.

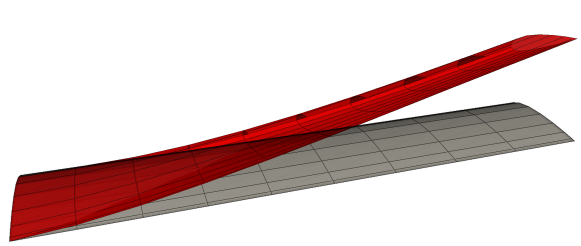

(a) Mode #1: 4.19 Hz.

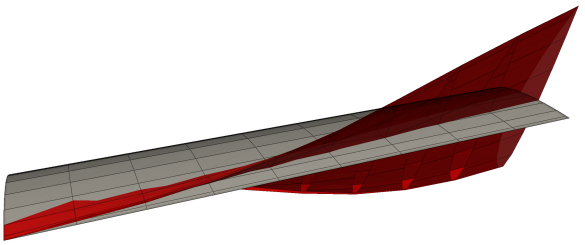

(b) Mode #2: 17.22 Hz.

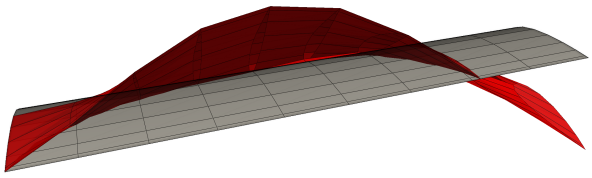

(c) Mode #3: 23.18 Hz.

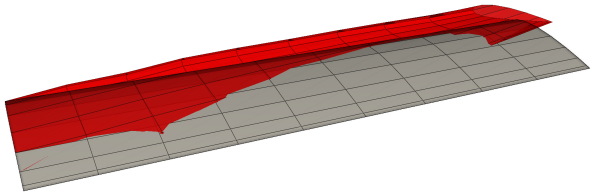

(d) Mode #4: 39.91 Hz.

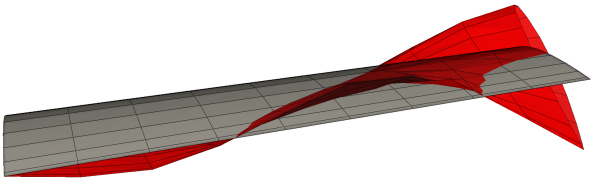

(e) Mode #5: 47.57 Hz.

Source: Elaborated by the author.

Furthermore, in the aerodynamic module, the aerodynamic influence coefficients ([AIC]) are obtained from the DLM and considering a Mach number of 0.25 at sea-level ($\rho_{air} = 1.225$ kg/m^3). To calculate the unsteady aerodynamic loads, first the downwash is computed applying the boundary conditions, i.e., the eigenvectors obtained from the modal analysis and the

corresponding aerodynamic control points. Next, having the [AIC] and the normalwash, then generalized aerodynamic loads are computed applying Eq. (5.42).

Finally, the flutter solution is calculated applying the p-k method, evaluating a range of velocities from 0 to 200 m/s. The interpolation of the aerodynamic matrices for different reduced frequency are done based on the methodology presented in Section 5.5.2.

Therefore, Fig. 36 shows the v-g-f diagram for the proposed wing, considering a velocity envelope from 0 to 200 m/s. For convenience, only the first five modes are plotted. Moreover, the solution obtained through SOL 145 of Nastran is also plotted in order to compare and verify the aeroelastic solution.

Figure 36 – V-g-f diagram of the flutter solution using p-k method.

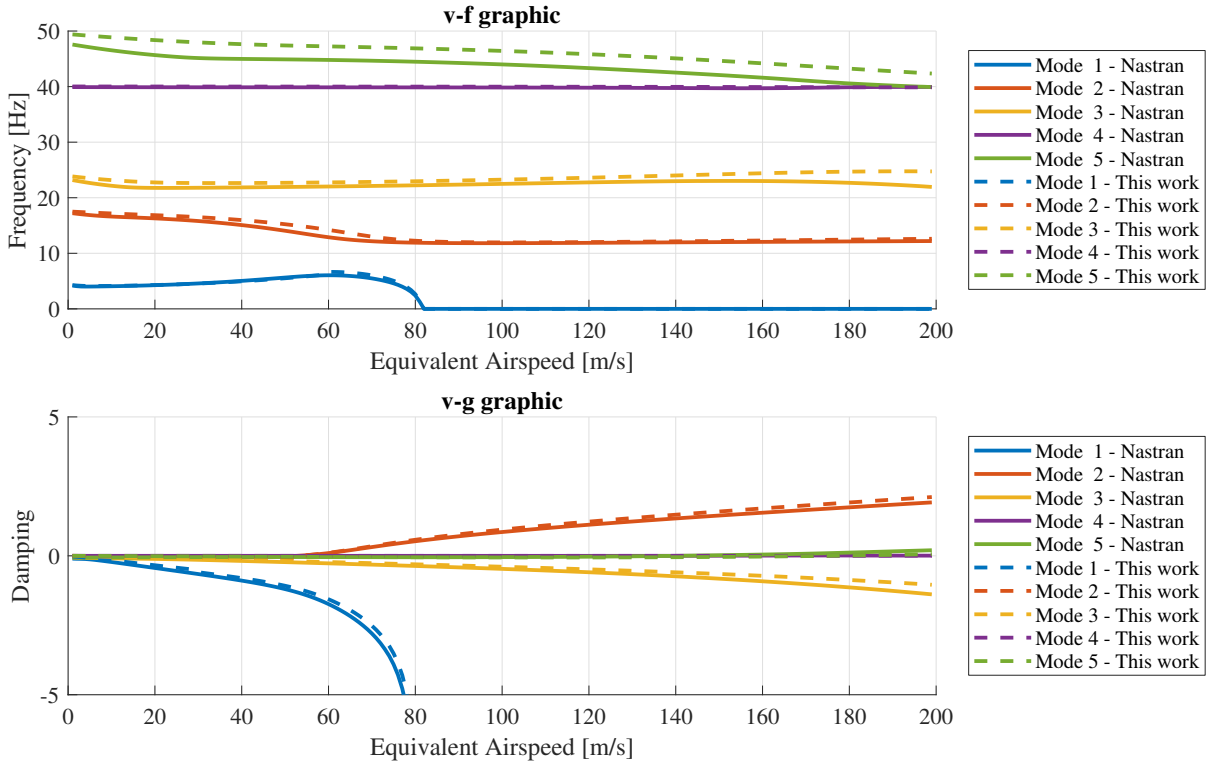

Source: Elaborated by the author.

Fig. 36 graphically illustrates the evolution of frequencies referring to the modes of bending (mode 1), torsion (mode 2) and other modes of the wing under analysis. Furthermore, the figure shows the critical point for the flutter velocity, which happens when the damping becomes positive, according to the solution developed in the p-k method. In this case, damping becomes positive for mode 2 (in red). This happens because the second mode (torsion) starts to

couple with the first mode (bending), leading to a dynamic instability. Thus, the flutter velocity value and its respective frequency are listed in Table 9.

Table 9 – Results from v-g-f diagram.

Parameter	Aeroelastic Module	Nastran	RE
$V_{flutter}$	54 m/s	53 m/s	1.89%
$\omega_{flutter}$	14.95 Hz	13.70 Hz	9.12%

The results presented are in good agreement with those obtained in Nastran. There are some small differences in the evolution of natural frequencies and damping, which causes a difference in the critical flutter frequency. This possibly happens due to the interpolation of generalized aerodynamic loads or even the numerical error due to the high order of the matrices in the p-k solution. The flutter velocities presented in Tab. 9, obtained in the null damping condition, are in agreement, as expected in the good representation of the damping evolution for the second mode (torsion), which is the unstable mode.

In general, the verification addressed here is as expected for the critical flutter condition. The differences obtained are justified by the methods and interpolations used in the aeroelastic solution. Although other differences may be present in the implementation of the p-k method, the convergence to the result of critical speeds is evident.

CHAPTER

6

WING DESIGN AND OPTIMIZATION

In this chapter, the proposed structural design of the wing is presented, as well as its optimization. The topological mesh of the structures are created from the Delaunay triangulation and tessellation. For the optimizations, a reference wing geometry from the FLEXOP project is used as a baseline. The optimizations are performed using NSGA-II algorithm.

6.1 Modular Truss-Based Wing Design

The work of Opgenoord and Willcox (2019) investigated what the authors called lattice structures, as illustrated in Fig. 10, in the design of wing structures. The authors focused on additive-manufactured elements, therefore not constrained by modularity requirements.

The wing designed in this work is based on the premise that modular structures will be used in its formation, that is, instead of traditional and conventional structures such as spars and ribs, truss-based modular structures will be used here. In other words, all internal wing-box components, except for the upper and lower skins, are replaced by truss-based structural elements. Thus, to do so, the trusses forming the lattice structure are defined from a catalogue of possible cross sections, and the number of possibilities in this catalogue defines the level of modularity of the design.

In this sense, to make the necessary connections between the modular structures, this work discretizes the wing as follows. First, as there are no ribs that form the airfoil, control points are used at each cross section. These control points are defined by means of a spline in

order to guarantee the selected aerodynamic profile. In the implementation, the definition of the points starts from the choice of the NACA profile of 4 or 5 digits and the number of points to form the spline. Furthermore, it is possible to determine if the trailing edge will be formed by only one point and if the spacing between the points will follow a half cosine based spacing. As an example, Fig. 37 depicts the spline and the corresponding control points for a profile NACA 2412 with 8 and 20 points, respectively. It is worth mentioning that those control points are going to be the nodes of the FEM model and the connection nodes of all elements.

Figure 37 – Cross section discretizations for NACA 2412.

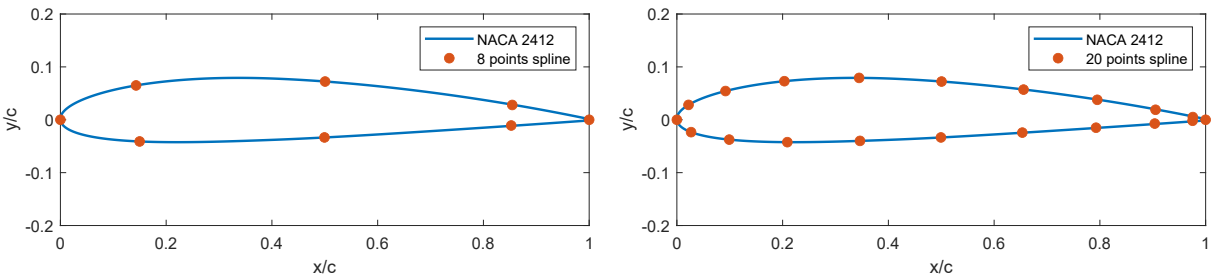

(a) 8 points spline.

(b) 20 points spline.

Source: Elaborated by the author.

Furthermore, instead of the conventional spars, the proposal here is to use the truss-based modular structures. However, to define the spatial arrangement of such structures is the big deal. Therefore, to create the structural mesh, this works makes use of the Delaunay Tessellation, i.e., the Delaunay Triangulation and Tetrahedrization to connect the cross section nodes and so create the maximum truss elements without without physically crossing them. This approach is presented in Section 6.1.1.

6.1.1 Delaunay Tessellation

Delaunay's algorithm is a finite element meshing process that has the ability to consistently subdivide the geometric domain into simplexes. Simplexes are extensions of triangles in other dimensions, i.e., line segments in one dimension, tetrahedrons in three-dimensional space, etc.

A simplex K is an ordered list of vertices $\{P_i\}$ with $1 \leq i \leq d+1$, where d is the dimension of the corresponding Euclidean space E. Det(K) is called the determinant of order

$d+1$ given by:

$$\det(K) = \begin{pmatrix} 1 & \cdots & \cdots & \cdots & 1 \\ P_1^1 & \cdots & \cdots & \cdots & P_{d+1}^1 \\ P_1^2 & \cdots & \cdots & \cdots & P_{d+1}^2 \\ \vdots & & & & \vdots \\ P_1^d & \cdots & \cdots & \cdots & P_{d+1}^d \end{pmatrix} \tag{6.1}$$

where P_i^j is the coordinate j of the point P_i for $1 \leq i \leq d+1$ and $1 \leq j \leq d$.

By definition, if $\det(K) > 0$, K is said to be positively oriented and if $\det(K) = 0$, K is said to be degenerate, that is, all its vertices belong to the same hyperplane (GEORGE; HERMELINE, 1992).

6.1.1.1 Principles of Triangulation

Triangulation of a domain Ω, which is supposed to be limited and polyhedral, is a set ζ of simplexes. For this set, the following conditions are valid (MARRETTO, 1999; SAKAMOTO, 2001):

- The intersection of two elements of ζ is empty or reduces to a vertex, an edge (in the two-dimensional case) or a face (in the three-dimensional case).
- The union of the elements of ζ is equal to Ω.
- The elements of ζ must be topologically regular: in the two-dimensional case, for example, these elements must be as close to equilaterality as possible, which does not oblige them to be equal.
- The circumcircle (two-dimensional) or circumsphere (three-dimensional) of an element is empty, in other words, no circumscribed (two-dimensional) circle or circumscribed (three-dimensional) sphere contains another node.

The domain Ω, in turn, can be decomposed into Voronoi V_i polyhedra associated with the P_i set of Ω, such that:

$$V_i = \left\{ P \in \Omega, \forall 1 \leq j \leq n, d\left(P, P_i\right) \leq d\left(P, P_j\right) \right\} \tag{6.2}$$

where $d\left(P, P_j\right)$ is the Euclidean distance between P and P_j, and n is the number of points.

From the polyhedra, the following results are demonstrable (MARRETTO, 1999):

- Polyhedra are convex, with a non-empty interior and form a cover such that two distinct elements have an empty intersection or reduced to a vertex, edge or face (Fig. 38a);
- For each vertex v (central vertex of a Voronoi polyhedron), it is associated a set that is called the convex envelope C_v.

A convex envelope C_v is a set of polyhedra that have v as one of its vertices. The set of convex envelopes C_v of a Voronoi polyhedron defines a Delaunay triangulation, in other words, the Delaunay mesh can be obtained by connecting two by two the central vertices (v_i, v_{i+1}) of the neighboring Voronoi polyhedra. neighbors (LEBENSZTAJN; FALCONE, 1989). The resulting mesh can be seen in Fig. 38b.

Figure 38 – Definitions of Delaunay triangulation.

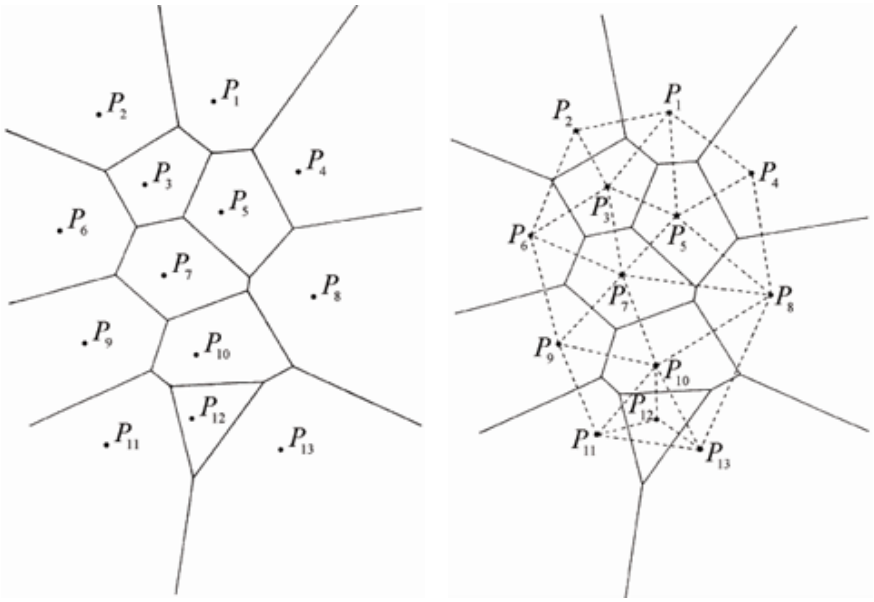

(a) Voronoi polyhedra. (b) Convex wrapping mesh.

Source: Marretto (1999).

6.1.1.2 Delaunay triangulation

A Delaunay triangulation (DT) for a set P of vertices must satisfy the Delaunay condition, which is: $DT(P)$ is a Delaunay triangulation such that no vertex of P lies within the circumcircle of any triangle in $DT(P)$. In Fig. 39, there is an example for a Delaunay triangulation for a set of

nine vertices. Given a set of vertices, which can be seen in Fig. 39a, it is possible to obtain the Delaunay triangulation in Fig. 39b for this set of points. Fig. 39c shows the triangles with their corresponding circumcircles.

Figure 39 – Definitions of Delaunay triangulation.

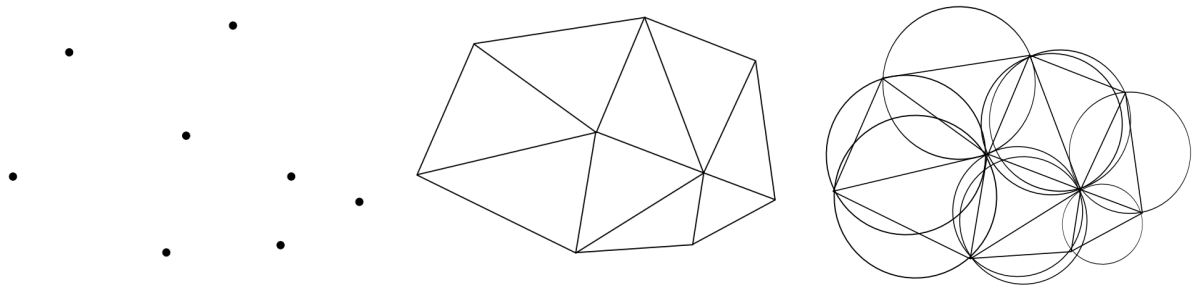

(a) Set of vertices. (b) Delaunay triangulation. (c) Circumcircles and triangles.

Source: Nogueira and Oliveira (2011).

The Delaunay triangulation maximizes the minimum angle of every triangle in the triangulation. This property is known as MaxMin. According to Shewchuk (1997), the MaxMin property was initially noticed by Lawson (1977) and this property contributed to the popularization of the Delaunay triangulation for the generation of meshes.

6.1.1.3 Conversion from 2D to 3D Delaunay Meshes

As mentioned in the previous sections, a 2D Voronoi polygon is defined by lines that bisect connection lines between neighbouring points. In 3D, the central point is surrounded by a convex polyhedron defined by planes which are limited by a surrounding polygon. These planes correspond to the line segments of a Voronoi polygon. Each plane bisects the line between two neighbouring points. In the same way, as the Voronoi diagram covers the complete area in 2D, a diagram of Voronoi polyhedra will fill the 3D space. The Delaunay diagram is defined by the connection lines between neighbouring points in the Voronoi diagram.

When Delaunay triangulation is extended to one more dimension, this results in Delaunay tetrahedrization. As three points are necessary to describe a plane in space, at least 4 points describe a volume element in space. The most elementary volume element is a tetrahedron, which is given by 4 points. In 2 dimensions there are no vertices from the network situated inside

the circumscribing circle of any triangle. The corresponding situation in 3 dimensions is called the sphere criterion: a Delaunay mesh in three dimensions consists of non-overlapping tetrahedra where no points in the network are enclosed by the circumscribing spheres of the tetrahedra.

Figure 40 lists the most important geometrical conditions of 2D triangulation together with their 3D versions.

Figure 40 – Geometrical conditions for Voronoi/Delaunay diagrams in 2 and 3 dimensions.

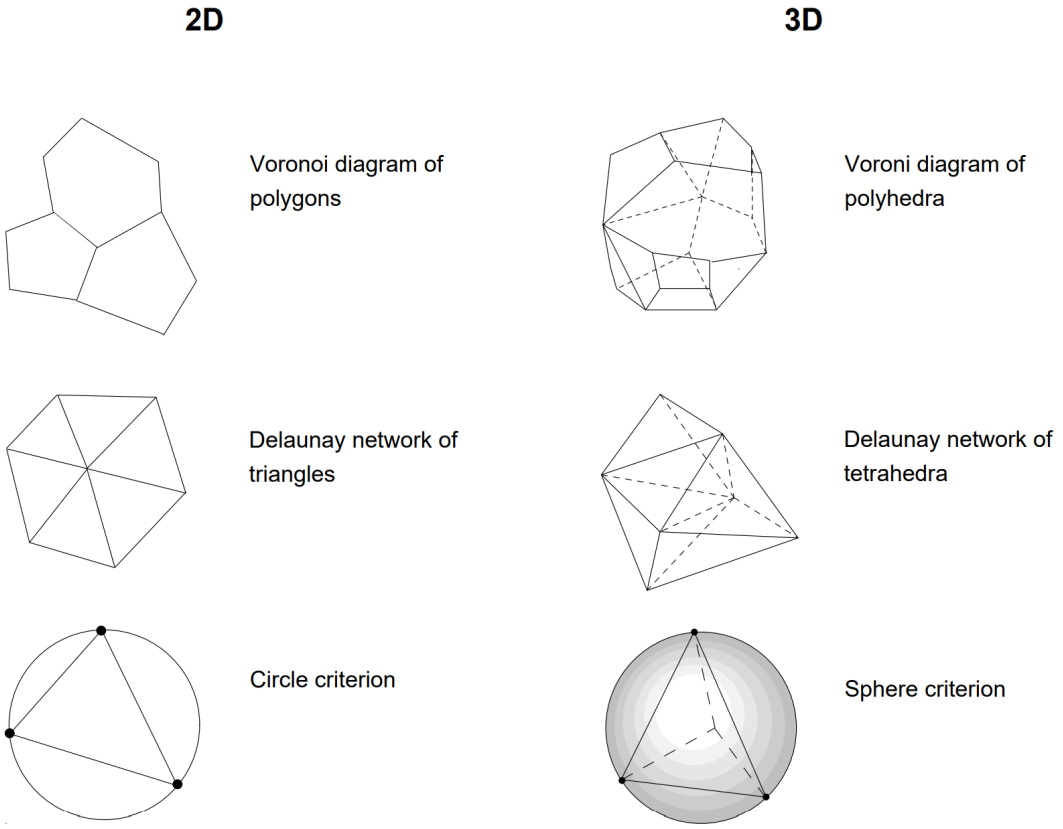

Source: Midtbo (1993).

6.1.1.4 Delaunay Triangulation and Tetrahedrization

The steps for the construction of the Delaunay triangulation in two-dimensional space and tetrahedrization in the three-dimensional space are very similar, the few differences concern the dimension of the coordinates, geometric shapes produced (edges and triangles; faces and tetrahedrons respectively) and the inclusion test of the new point that is performed by calculating the circumcircle in two dimensions and the circumsphere in three dimensions. Machado and Cardoso (1993) describes the steps for a Delaunay tetrahedrization and following the same procedures adopted, these steps are extended to two and three dimensions.

- Build a list with the coordinates of the n points that describe the domain. These coordinates are x, y for two-dimensional space and x, y, z for three-dimensional space.
- Determining an encompassing quadrilateral from the "extent" (extent of the domain). The "extent" is the calculation of the maximum and minimum coordinates of the n points. In the three-dimensional case, an encompassing hexahedron is determined.
- Decompose the quadrilateral into two triangles with the n points spread over them. For the hexahedron this division is done with six tetrahedra.
- The list of points is inserted into the "extent". By calculating the circumcircle (or circumsphere) of the initial mesh, the triangle (or tetrahedron) elements that include the new point are eliminated. Thus new elements are generated from the new point and the remaining elements. The process is repeated for the remaining points until all are included.
- After all points are included, elements (triangles/tetrahedrons) with vertices that coincide with the vertices of the "extent" are eliminated.

6.1.1.5 Wing Structural Mesh with Delaunay Tessellation

Having the Delaunay Triangulation and Tetrahedrization stated in the previous sections, the wing structural mesh is designed from the control points defined in each cross section. Therefore, as an example, the structural meshes for a wing of 10 cross section and considering 8 (as in Fig. 37a) and 20 (as in Fig. 37b) control points in each cross section are shown in Fig. 41a and 41b, respectively.

Figure 41 – Truss-based structural meshes for 8 and 20 control points in each cross section, respectively.

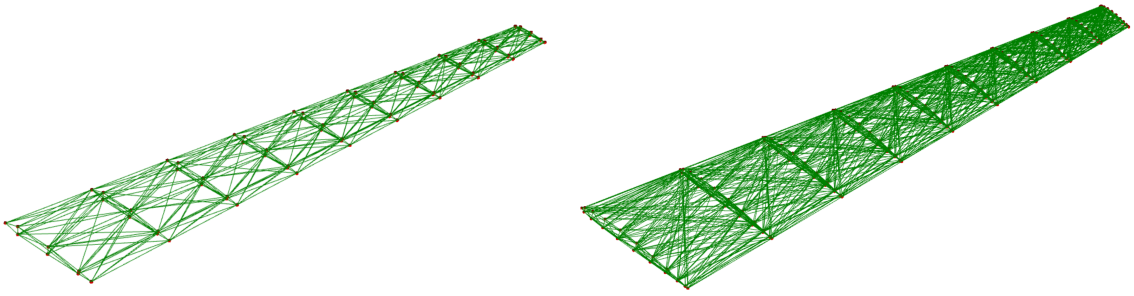

(a) 8 points spline. (b) 20 points spline.

Source: Elaborated by the author.

6.1.2 Joint Design

Metallic and lattice structures are quite common in civil engineering. The structure node is the intersection point of the bars. Connections are normally considered to be kneecap nodes with centered axial loads. However, the execution of nodes that guarantee a perfect kneecap condition is very difficult and expensive. In this way, what is sought is to design a connection with loads without eccentricities.

Since the structural wing design here is based on truss-elements, it is important to ensure the perfect union of the elements and the transfer of loads between them. Therefore, the choice and/or design of the connection joint of the modular elements is a very important issue that would demand a dedicated study.

According to Worku (2007), the type of jointing depends primarily on:

- The connecting technique, whether it is bolting, welding, or applying special mechanical connectors.
- The shape of the members, This usually involves a different connecting technique depending on whether the members are circular or square hollow sections or rolled steel sections.

In designing the jointing system, the following requirements should be considered:

- The joints must be strong and stiff;
- Simplicity in terms of structurally and mechanically ;
- Easy to fabricate without recourse to more advanced technology;
- The eccentricity at a joint should be kept to a minimum, yet the joints detailing should provide for the necessary tolerances that may be required during the construction;
- The joints of space frames must be designed to allow for easy and effective maintenance.

The cost of the production of joints is one of the most important factors affecting the final economy of the finished structure. Usually the steel consumption of the connectors will constitute

15 to 30% of the total. Therefore, a successful prefabricated system requires joints that must be repetitive, mass produced, simple to fabricate, and able to transmit all the forces in the members interconnected at the node.

6.1.2.1 Models of Joints

Over the last few decades, various models of joints have been developed for different applications, mainly in civil construction. Many joints weld the dams using a flat tip, while others allow the screwing of tubular elements. Fig. 42 shows some examples of joints. The subfigs depicts the following: (a) typical connection used in the United States in 1960; (b) connection with flattened steel tube at the ends and bols tin thin-walled plate used in 1968; (c) typical connection with flattened steel tube at the ends and connect with a bolt used in 1968; (d) connection proposed by Du Château in 1970; (e) Vestrut system patented connection space in 1980.

Figure 42 – Typical connection models for space trusses.

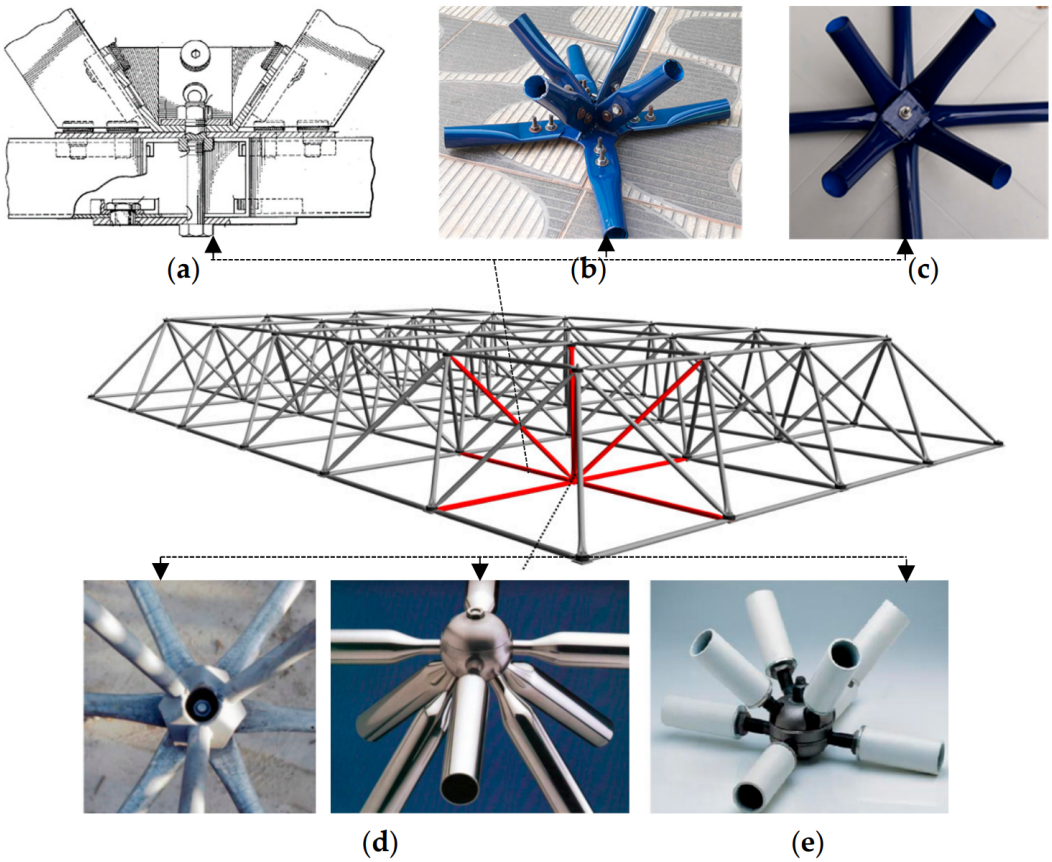

Source: Silva *et al.* (2020).

The Mero connector, introduced in 1940 by Dr. Mengeringhanusen, proved to be extremely popular and has been used for numerous temporary and permanent buildings. Its joint consists of a node that is spherical hot-pressed steel forging with flat facets and tapped holes. Members are circular hollow sections with cone-shaped steel forgings welded at the ends, which accommodate connecting bolts. Bolts are tightened by means of a hexagonal sleeve and dowel pin arrangement, resulting in a completed joint such as that shown in Fig. 43. Up to 18 members can be connected at a joint with no eccentricity (CHEN; LUI, 1999; DAVIES, 1967).

Figure 43 – Typical connection models for space trusses.

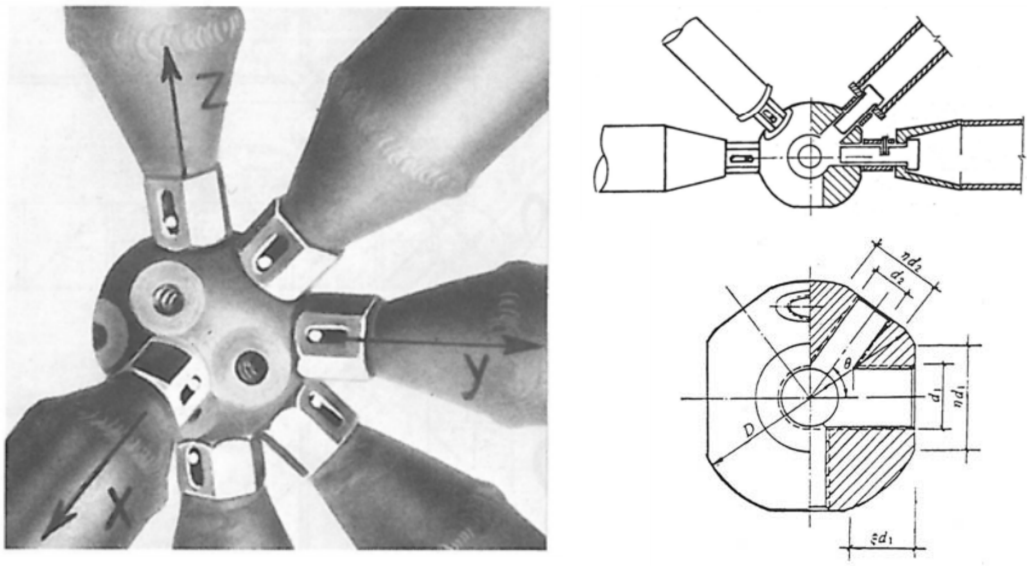

Source: Lan (1999).

The Mero connection has the advantage that the axes of all members pass through the center of the node, eliminating eccentricity loading at the joint; therefore the joint is only under axial forces. Tensile forces are then carried along the longitudinal axis of the bolts and resisted by the tube members through the end cones (LAN, 1999; MAKOWSKI, 2002). The size of the connecting bolt of compression members, based on the diameter estimated from internal forces, may be reduced by 6 to 9 mm. The diameter of a steel node may be determined by the following equation (LAN, 1999; CHEN; LUI, 1999):

$$D \geq \sqrt{\left(\frac{d_2}{\sin\theta} + (d_1 \cot\theta + 2\xi d_1)\right)^2 + \eta^2 d_1^2} \tag{6.3}$$

To satisfy the requirements of the connecting face of the sleeve, the diameter should be checked

using the following equation (LAN, 1999; CHEN; LUI, 1999):

$$D \geq \sqrt{\left(\frac{\eta d_2}{\sin\theta} + (\eta d_1 \cot\theta)\right)^2 + \eta^2 d_1^2} \tag{6.4}$$

where D is the diameter of steel ball, θ the smaller intersecting angle between two bolts, d_1 and d_2 are the diameter of bolts, ξ the ration between the inserted length of the bolt into the steel ball and the diameter of the bolt, η the ration between the diameter of the circumscribed circle of the sleeve and the diameter of the bolt.

After the invention of the Mero connection, several other systems were patented with the same principle: steel ball, hexagonal screw, connection sleeve, and hollow section bar. The connection system with spherical nodes showed satisfactory results in experimental tests, mainly because bending moments were not mobilized in the connection. The assembly system is theoretically simple, using only a torque wrench to tighten the bolt (AYDINCILAR, 2010; CAGLAYAN; YUKSEL, 2008; EBADI; DAVOODI, 2012; PIROGLU; OZAKGUL, 2016). On the other hand, this technology has a high manufacturing cost as a disadvantage. In this way, researchers and designers sought to develop a connection system with a lower cost that could be manufactured in small metallurgical companies (SOUZA, 2003), and then the typical connection system was developed. Other patented joints that allow greater adjustment, or even rotation of the elements, are the Vestrut and the SR (spherical rolling) joints, shown in Figs. 44a and 44b, respectively.

Figure 44 – Joints with more angle configurations.

(a) Vestrut joint. (b) Spherical rolling joint.

Source: Hephaist (2022).

6.1.3 Joint Mass Estimate

It was not the objective of this thesis to go into the detailed design of the joints. However, in the aeroelastic system it is important to consider the weight of the joints at the nodes, since it affects the total weight of the structure and even the dynamic behavior of the structure. Therefore, for this work, it was assumed a reasonable mass of 150 g for each joint in the structure. It is worth mentioning that in the sequence of this work it is intended to consider the joint design together with the wing design, as well as to take geometric connections as a constraint in the optimization of the truss elements, i.e., the angles between the elements in the joints will be considered as a design constraint.

6.2 FLEXOP's Wing Model

From the thematic exposition developed in the other chapters and sections, the objective of this work is to apply modular structures as alternatives in the projects of wings. Thus, it was necessary to choose a reference wing model to create a model and perform the analyses. Overall, there are several models and sizes of wings that could be used, given the wide range of aircraft categories available; however, the author chose to select a wing of a smaller aircraft whose model has been the object of study in publications in recent years both from a structural and aeroelastic point of view, such as the ones published by Roessler *et al.* (2020), Roessler *et al.* (2019), Takarics *et al.* (2020), Meddaikar *et al.* (2018).

Thus, the reference wing geometry selected for this work comes from the flying demonstrator of the FLEXOP (Flutter Free FLight Envelope eXpansion for ecOnomical Performance improvement) (SODJA; WERTER; De Breuker, 2018; SÜELÖZGEN; WÜSTENHAGEN, 2019), which is a project within the European Union's Horizon 2020 framework. The aircraft is depicted in Fig. 45. Its main goal is to raise efficiency of a currently existing wing by derivative solution with higher aspect ratio at no excess structural weight. Moreover, the project was launched in 2015, and a consortium of aerospace companies, universities and research institutions set the goal to develop methods and tools suitable for aircraft design with highly flexible wings and active flutter suppression, developing and demonstrating passive load alleviation using aeroelastic tailoring and active flutter control methodologies.

Figure 45 – FLEXOP flight demonstrator.

Source: Süelözgen and Wüstenhagen (2019).

Therefore, along those lines, such a model is convenient for the study and analysis of the proposal of this work. The work of Sodja, Werter and De Breuker (2018) shows information and some details about the geometry, dimensions and internal structures of the FLEXOP wing. Figure 46 illustrates the structural layout of the wing and Table 10 lists the main geometric parameters.

Figure 46 – Wing structural layout.

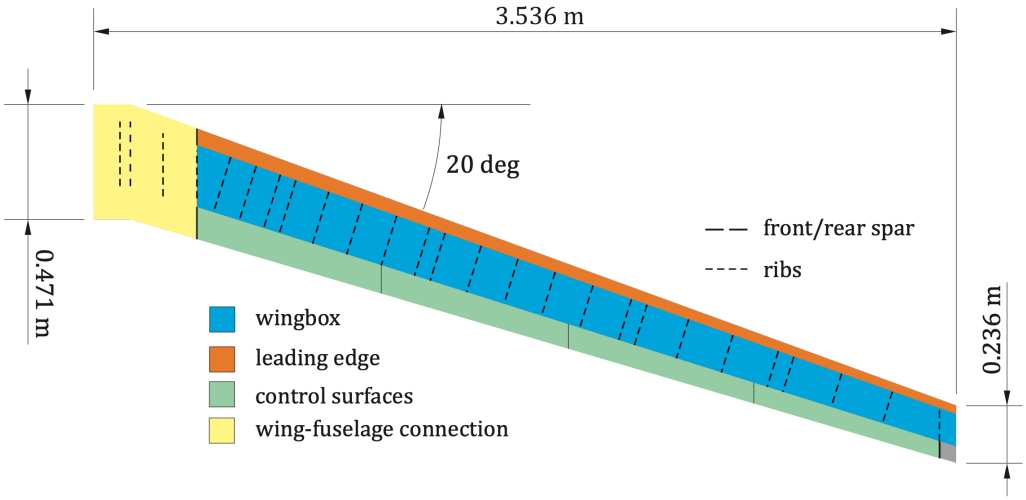

Source: Sodja, Werter and De Breuker (2018).

The high aspect ratio of 20 and thin airfoil profile makes the lightweight structural design especially challenging, given the low second area moment of inertial of the wingbox and the large bending loads at the wing root.

At this point, it is worth summarizing the wing design approach of this work. First, it uses the dimensions and geometry of the FLEXOP wing planform. Second, the number of cross

Table 10 – Geometric parameters for the FLEXOP reference wing.

Parameter	Value
Semi-span	3.536 m
Aspect ratio	20
Airfoil	try6
Chord, root	0.471 m
Chord, tip	0.236 m
Thickness, root	10% chord
Thickness, tip	8% chord
Sweep, leading edge	20 deg

Source: Sodja, Werter and De Breuker (2018).

sections along the wingspan is chosen. Next, the number of control points (nodes) in each of the cross sections is defined. Finally, a spatial mesh/arrangement of modular structures is created using the Delaunay tessellation method.

Thus, the structural model is then created and, using the tools developed in Chapters 3, 4 and 5, it is possible to obtain the unsteady aerodynamic loads, extract the mass and stiffness matrices and vibration modes from the modal analysis, and perform the aerostructural coupling, obtain the flutter solution and verify the aeroelastic stability condition. The flowcharts in Figs. 31 and 32 depict the integration of those tools.

The reader may have noticed that the definition of the number of cross sections and the number of control points (nodes) in each cross section directly affects the number of modular structures created by Delaunay's spatial tessellation. Furthermore, the wing design proposal in this work is to generate the lightest possible wing using modular structures, but accounting for structural and aeroelastic constrains. Therefore, it is necessary to think from an optimization point of view, that is, what is the best combination of design variables that generate such results and, finally, to study the trade-off of benefits through the Pareto curves obtained by the optimizations. The optimization method applied is presented in the next chapter.

6.3 Method of Optimization

For the optimizations developed in this work, it is necessary to choose some optimization method and algorithm. As the wing design goals are to minimize its weight and maximize the

flutter speed, the case here indicates a multi-objective optimization problem. Thus, the `pymoo` package in Python was used, which has already implemented several optimization algorithms. Furthermore, for this work, the NSGA-II was the algorithm chosen.

The Non-dominated Sorting Genetic Algorithm II (NSGA-II) was proposed by Deb *et al.* (2002). It is a widely used algorithm for solving multi-objective problems, having its application in several works in the literature. NSGA-II is a genetic algorithm as proposed by Holland (1992); thus, it is a bio-inspired metaheuristic that follows the principle of natural selection described by Darwin, in which the fittest individual has a greater probability of survival.

For multi-objective problem solving, the NSGA-II treats the possible solutions of the problem as individuals belonging to a population. This, in turn, goes through the process of evolution through iterations, known as generations.

NSGA-II has a new population selection scheme based on two main operators: Pareto Ranking and a parameter-free population diversity promotion metric called Crowding Distance (CD).

The Non-dominated Sorting (or Pareto Sorting) proposed by Goldberg (1989) consists of classifying a population P into d subsets such that $F_1 = \{$non-dominated individuals of P that are not dominated by any other of $P\}$ (rank 1), $F_2 = \{$non-dominated individuals of $P \backslash F_1$ and who are not dominated by any other of $P \backslash F_1\}$ (rank 2), $F_3 = \{$non-dominated individuals of $P \backslash \{F_1 \cup F_2\}$ and that are not dominated by any other of $P \backslash \{F_1 \cup F_2\}$ } (rank 3), ..., $F_d = \{$non-dominated individuals of $P \backslash \{F_1 \cup F_2 \cup \cdots \cup F_{d-1}\}$ and that are not dominated by any other of $P \setminus \{F_1 \cup F_2 \cup \cdots \cup F_{d-1}\}$ } (rank d), where $P = F_1 \cup F_2 \cup \cdots \cup F_d$. The survival selection is depicted in Fig. 47.

The crowding distance (CD) metric value of each solution is based on the distance its image is from the closest neighboring images for each objective function within the same rank. The higher the value of CD, the farther the solution is from its neighbors in the objective space, making it more preferred in selection for the next generation of the population. In order to keep the candidate solutions that have an image at the ends of a station, an infinite value is assigned to their CDs. In a problem with two objective functions, CD is the semiperimeter of a rectangle

Figure 47 – NSGA-II survival selection.

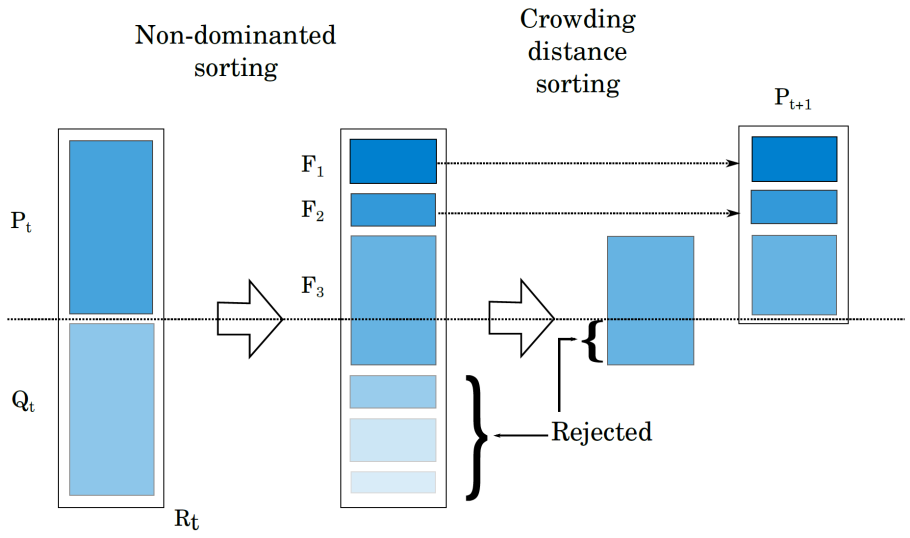

Source: Deb *et al.* (2002).

whose vertices are the closest neighboring images. The CD calculation is depicted in Fig. 48, where the points marked in filled circles are solutions of the same nondominated front.

Figure 48 – Crowding-distance calculation.

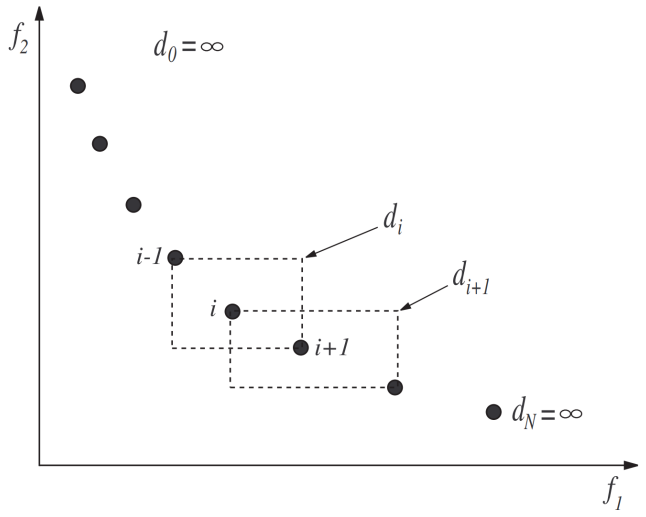

Source: Lobato (2008).

The procedure for selecting the new generation of the NSGA-II population is carried out as follows: the current population is joined with the generated children and this set is classified by the Pareto Sort procedure. Individuals with lower ranks will have preference for entry into the next generation of the population. When it is necessary to select an individual among 2 or more within the same rank, the individual with the highest CD value will be preferred.

6.4 Optimization #1

Once again, the proposal of this work is to design a structural model using modular truss-based elements, having the FLEXOP wing as geometry reference. To do so, the design will seek for minimizing the structural weight of the wing (W_{wing}) and maximizing the flutter speed ($V_{flutter}$), taking into consideration structural and aeroelastic constraints.

Along those lines, for the first optimization case, the following parameters are stated as design variables: the number of control points (nodes) in each cross section of the wing ($n_{\text{control points}}$), the number of cross sections distributed along the wingspan ($n_{\text{cross sections}}$), and the diameter of all elements of modular structures (D_{bar}), which are considered here as solid truss bars.

To get started, the search range of the design variables, i.e., the intervals of values for optimization for $n_{\text{control points}}$, $n_{\text{cross sections}}$, and D_{bar} go from 8 to 32, 6 to 14, and 3 to 10 mm, respectively. Thus, the multi-objective optimization problem #1 is summarized as follows:

$$\textit{Multi-objective optimization problem \#1} : \begin{cases} \min\left(W_{wing}\right) \quad \text{and} \quad \max\left(V_{flutter}\right) \\ \mathbf{x} : [n_{\text{control points}}, n_{\text{cross sections}}, D_{\text{bar}}] \\ 8 \leq n_{\text{control points}} \leq 32 \\ 6 \leq n_{\text{cross sections}} \leq 14 \\ 3 \leq D_{\text{bar}} \leq 10 \quad [\text{mm}] \end{cases}$$

Using the NSGA-II algorithm, the optimization was executed with a number of population of 100 and generations equal to 1000. The NSGA-II works with the selection scheme presented in section 6.3 and it generates the population of children from the population of parents using the SBX (Simulated Binary Crossover) operator. For this approach, the crossover index (η_c) and the mutation index (η_m) are defined as 3.0 and 3.0, respectively.

Furthermore, the aeroelastic constraint is accounting for the flutter speed and divergence speed. The p-k method (see Chapter 5 and Section 5.5.1) is evaluated from 0 to 200 m/s with a increment in speed (ΔV) of 0.1 m/s. The skin applied to the structure has a thickness (t_{skin}) of 1 mm. Regarding the structural constraints, it is evaluated for the truss bars the Yield strength

and Euler's critical load with a safety factor (FS) of 1.5. It is worth mentioning that the skin buckling is not evaluated in this work. Moreover, both the element types, i.e., truss bars and skin are assumed as made of Aluminum 7075 Heat Treated (T6), whose main properties include a modulus of elasticity (E) of 71.7 GPa, Poisson ratio of 0.33, and density of 2795.7 kg/m^3.

The optimization algorithm was run using Spyder, an IDE for Python, and on a computer with a processor 11th Gen Intel Core i7-1165G7 @ 2.80GHz, 16 GB of RAM, 512 GB of SSD, and the solution took around 156 hours to complete. Thus, the solution for the optimization problem #1 is given by the Pareto-optimal front depicted in blue circles in Fig. 49.

Figure 49 – Pareto front for Optimization #1.

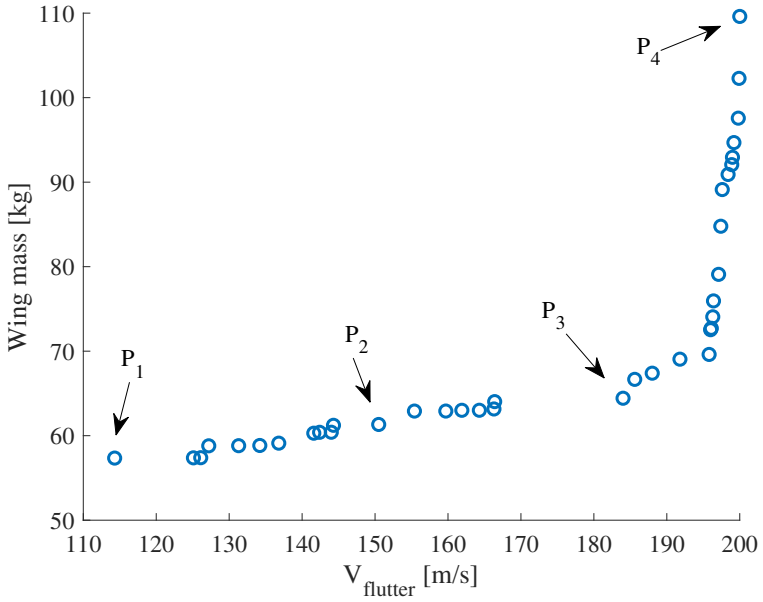

Source: Elaborated by the author.

As one can see, the result in Fig. 49 shows that to maximize the flutter speed, targeting a better aeroelastic behavior, there is a impact of the structural weight of the wing. Also, the feeling is mutual, i.e., it is possible to have a lighter wing, but the flutter speed is compromised. This trade-off is important in aircraft design, after all, the choice of design variables define the structural behavior and affects the overall aircraft weight. Regarding the design variables, the NSGA-II found different combinations that delivered that result. The $n_{\text{control points}}$ varied from 8 to 26, $n_{\text{cross sections}}$ from 6 to 14, and D_{bar} varied from 3 to 9 mm.

Also in Fig. 49, four points were selected: P_1, P_2, P_3, and P_4. These points represent four

different options for the wing design. P_1 is the case where the wing has the lowest weight and worst flutter speed in that range. At the other end, P_4 is the case where the aircraft has the highest weight and best flutter speed in that range. The other points between P_1 and P_4 have different combinations of the design variables. The details of the wing design optimization for the four points selected are displayed in Table 11 and the corresponding structures are depicted in Fig. 50.

Table 11 – Results of the design variables in optimization #1 for points P_1, P_2, P_3 and P_4 from Fig 49.

Parameter	P_1	P_2	P_3	P_4
$n_{\text{control points}}$	8	8	16	24
$n_{\text{cross sections}}$	6	11	14	9
D_{bar} [mm]	3	5	4	7
$V_{flutter}$ [m/s]	114.3	150.6	184.2	199.9
Wing mass [kg]	57.23	61.18	64.21	109.74

Figure 50 – Structural mesh of the truss-based wings obtained in P_1, P_2, P_3 and P_4.

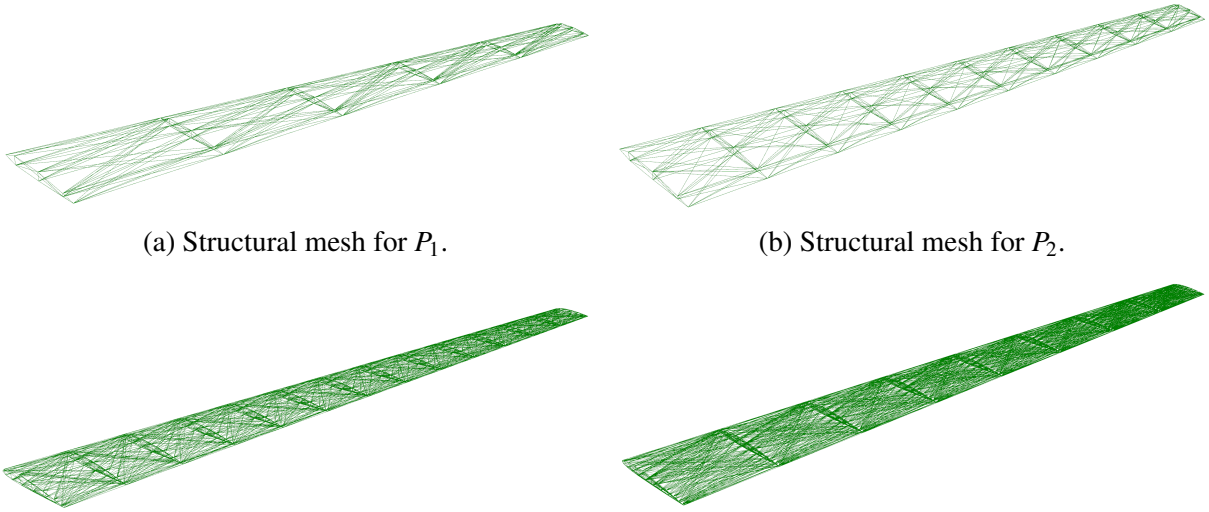

(a) Structural mesh for P_1.

(b) Structural mesh for P_2.

(c) Structural mesh for P_3.

(d) Structural mesh for P_4.

Source: Elaborated by the author.

Moreover, the flutter solutions for all four points are shown in Fig. 51 in terms of v-g-f diagrams. As one may notice, each structural mesh results in different modes, since there are different number of elements and also the diameter of the elements change over the optimization. Also, the mode of flutter onset changes among the four points; for example, for P_1, the v-f graphic shows a coupling of modes 1 an 2 (bending and torsion, respectively), while v-g graphic shows the mode 2 becomes unstable at 114.3 m/s. On the other hand, for P_2, the v-f graphic shows a coupling of modes 4 and 5, resulting in a flutter speed of 150.6 m/s.

Figure 51 – Flutter solutions for points P_1, P_2, P_3 and P_4.

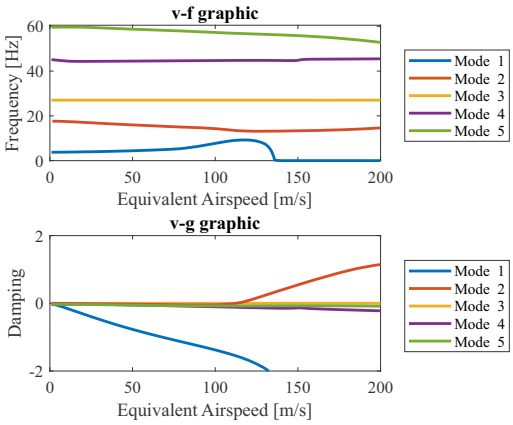

(a) V-g-f diagram for P_1.

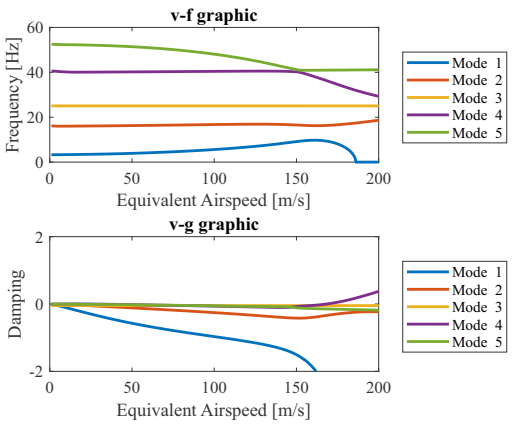

(b) V-g-f diagram for P_2.

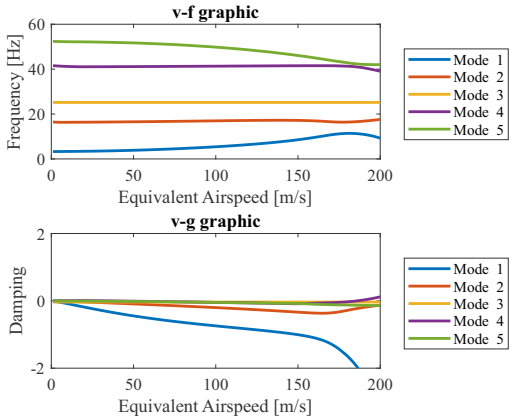

(c) V-g-f diagram for P_3.

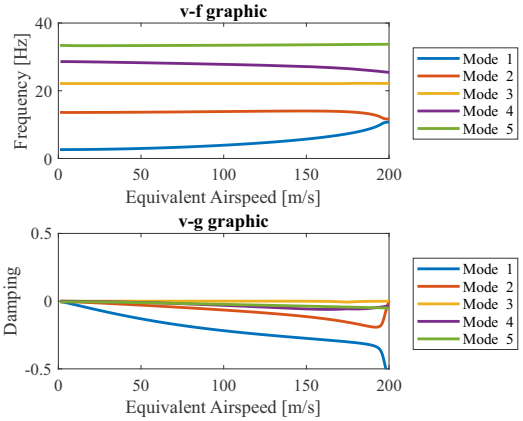

(d) V-g-f diagram for P_4.

Source: Elaborated by the author.

At this point, it is possible to imagine and intuitive to say that considering all the modular structures in the mesh/tessellation created by the Delaunay method does not represent the most efficient wing in terms of weight; after all, the more control points and/or number of cross sections, more structures are inserted into the model, but many of these structures are unnecessary, that is, their removal would not affect the aeroelastic response, but would reduce the weight of the structure. Furthermore, the truss-based elements do not have to be solid bars, but tubular structures, which represents a considerable weight reduction. So, individually evaluating the inclusion or not of each element is a condition for a new optimization, which is presented in the next section.

6.5 Optimization #2

In last section, i.e., in Optimization #1, the wing design was performed considering an optimization in terms of $n_{\text{control points}}$, $n_{\text{cross sections}}$, and D_{bar}. However, it is not very efficient to considered all the modular structures as solid bars. Therefore, at this point, the objective is to optimize all the modular elements individually; in other words, the optimization will try to eliminate some elements and will check how the resultant weight and aeroelastic behavior are.

At first sight, it is important to consider another constraint. The optimizer can not eliminate any element randomly. It is important to ensure at least the elements that form the airfoil shape and the wing planform; otherwise, the optimizer would try to eliminate any structural element that does not encounter any load path, and it could result in inconsistent and unfeasible structural wing model. Therefore, such constraint is required to establish the minimum wing profile is ensured.

The optimizer will design the wing eliminating or not the lattice elements. In addition, the outer diameter and tubular thickness of each individual element will be optimized. As one can imagine, to do so, it is necessary to know the number of lattice elements in the structure in order to optimize them, and, to know this number, it is necessary to previously define the number of control points (nodes) in each cross section and the number of cross sections along the wingspan. Only then is it possible to obtain the number of optimization variables. For example, $n_{\text{control points}} = 8$ and $n_{\text{cross sections}} = 10$, the lattice created by Delaunay approach results in 690 truss elements. If only the $n_{\text{cross sections}}$ were increased to 11, the lattice results in 766 truss elements. Therefore, if the optimizer were also to optimize the both parameters, i.e., $n_{\text{control points}}$ and $n_{\text{cross sections}}$, it would result in an optimizer inside of another optimizer, which would result in an unreasonable computing cost.

Having that said, it is important to first define the values of $n_{\text{control points}}$ and $n_{\text{cross sections}}$. Since both parameters can vary in a range of possibilities, the approach here is to select some pairs of those values in order to investigate how the optimization evolves with changing parameters. Thus, the multi-objective optimization problem #2 is summarized as follows:

$$\textit{Multi-objective optimization problem \#2} : \begin{cases} \text{Define: } n_{\text{control points}}, n_{\text{cross sections}} \\ \min\left(W_{wing}\right) \quad \text{and} \quad \max\left(V_{flutter}\right) \\ \mathbf{x} : [D_{i_{\text{ext,tube}}}, t_{i_{\text{tube}}}] \quad \text{for } i = 1, 2, \ldots, N_{\text{truss elements}} \\ D_{i_{\text{ext,tube}}} = 10, 15 \text{ or } 20 \quad [\text{mm}] \\ t_{i_{\text{tube}}} = 2, 4 \text{ or } 6 \quad [\text{mm}] \end{cases}$$

For this work, three pairs of values of $n_{\text{control points}}$ and $n_{\text{cross sections}}$ were chosen. First, the optimization will run assuming a $n_{\text{control points}}$ equals to 8 and $n_{\text{cross sections}}$ equals to 10. These values were chosen to ensure at least the minimum shape of the wing. Next, in the second optimization, the $n_{\text{control points}}$ is increased from 8 to 14, and $n_{\text{cross sections}}$ is kept as 10. Then, in the third optimization, the $n_{\text{control points}}$ is kept as 14, and $n_{\text{cross sections}}$ is increased from 10 to 20. All three pairs of configurations generate different numbers of elements and design variables, which are summarized in the Tab. 12.

Table 12 – Values for $n_{\text{control points}}$ and $n_{\text{cross sections}}$ and the corresponding number of elements.

	$n_{\text{control points}} = 8$ $n_{\text{cross sections}} = 10$	$n_{\text{control points}} = 14$ $n_{\text{cross sections}} = 10$	$n_{\text{control points}} = 14$ $n_{\text{cross sections}} = 20$
Number of truss elements	345	630	1309
Number of design variables	690	1260	2618

Once again, the NSGA-II algorithm was chosen for the optimization, which was executed with a number of population of 100 and generations equal to 1000. The crossover index (η_c) and the mutation index (η_m) were defined as 3.0 and 3.0, respectively.

Similarly to what was done in Optimization #1, the aeroelastic constraint is accounting for the flutter speed and divergence speed. In contrast, the P-K method here is also evaluated from 0 to 200 m/s, but with a increment in speed (ΔV) of 1 m/s. The increment was increased from 0.1 to 1 m/s, when compared to Optimization #1, due to the computational cost to get the optimization done. The skin applied to the structure has a thickness (t_{skin}) of 1 mm. Regarding the structural constraints, it is evaluated for the truss bars the Yield strength and Euler's critical load with a safety factor (FS) of 1.5. It is worth mentioning that the skin buckling is not evaluated in this work. Moreover, both the element types, i.e., truss bars and skin are assumed as made of

Aluminum 7075 Heat Treated (T6), whose main properties include a modulus of elasticity (E) of 71.7 GPa, Poisson ratio of 0.33, and density of 2795.7 kg/m^3.

The optimization algorithm was run using Spyder, an IDE for Python, and on a computer with a processor 11th Gen Intel Core i7-1165G7 @ 2.80GHz, 16 GB of RAM, 512 GB of SSD, and each solution took around 84 hours to complete. Thus, the solutions for the optimization problem #2 is given by three Pareto-optimal fronts depicted in Fig. 52.

Figure 52 – Pareto fronts for Optimization #2.

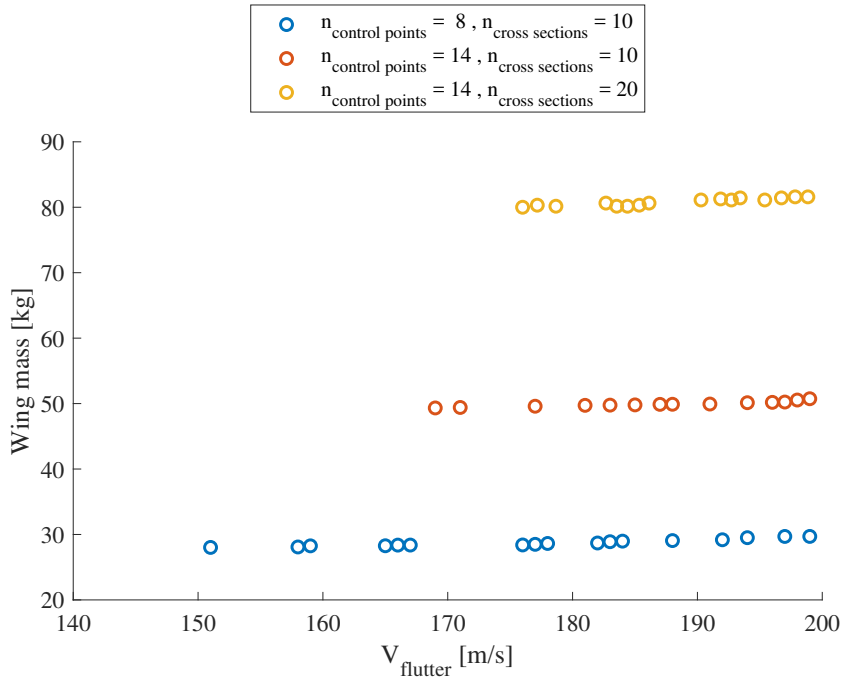

Source: Elaborated by the author.

From Fig. 52, the three Paretos show different wing designs for the problem previously defined. It is worth mentioning that there are few points in the Paretos. This happens because the flutter solution (p-k method) used in the optimization considered a speed increase of 1 m/s. So, the flutter speeds were always approximated by integer values, which made the Pareto ranking criterion eliminate the individuals that had the highest wing mass for each speed. Therefore, if a speed increment of 0.1 m/s were used, for example, there would probably be more points along each Pareto, but the computational cost would increase exponentially. Anyway, such solutions are sufficient for the purpose of this work, which is to verify the structural and aeroelastic design of the wing through optimization.

Furthermore, in Fig. 52 it is possible to see that the range of flutter velocities decreases as the discretization increases, i.e., the number of elements on the wing. This happens because the greater number of elements stiffens the wing and increases its weight, thus increasing the flutter speed. Speaking of weight, as the amount of elements increases, the weight increases considerably. It is worth remembering that the optimizer tried in its 1000 generations to eliminate as many unnecessary elements as possible, but even so the increase in weight is quite considerable, since for the same flutter speeds, a lighter wing is achieved (Pareto in blue). What influences in this case is how the optimizer defined the internal arrangement of each structure.

In this sense, selecting only the Pareto in blue from Fig. 52, since it brings the greatest cost-benefit in terms of structural weight and aeroelastic behavior, the vertically expanded Pareto is obtained in Fig. 53.

Figure 53 – Pareto front for $n_{\text{control points}} = 8$ and $n_{\text{cross sections}} = 10$ from Fig. 52.

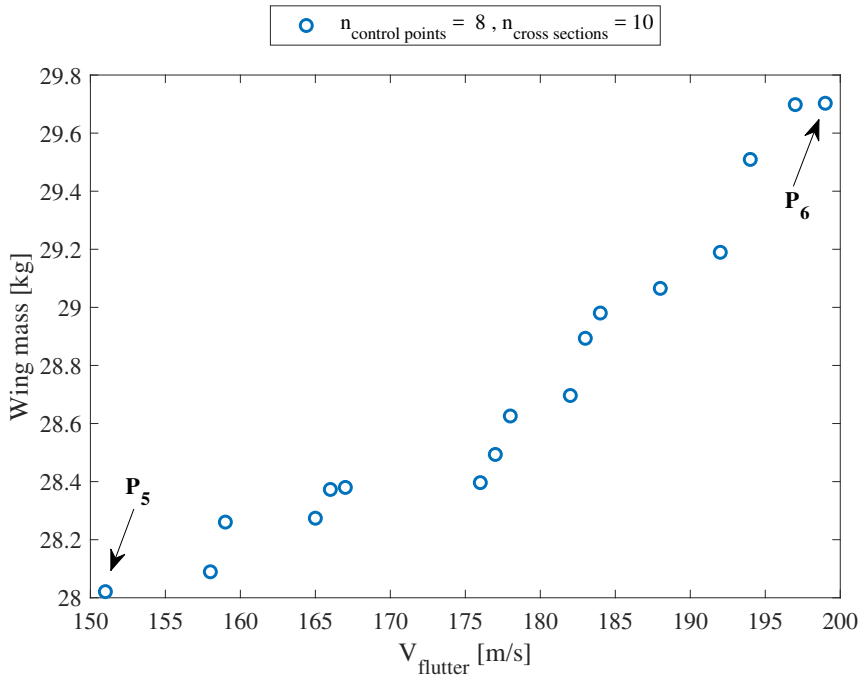

Source: Elaborated by the author.

From Fig. 53, it is possible to verify only a small change in weight along the y-axis, while there is a considerable gain in flutter speed along the x-axis. Each point of that Pareto represents a different combination of design variables, which in this case it means different combination of outer diameter and tubular thickness. Also, even if the number of nodes in the

wing structure is the same for all Pareto points, since the number of nodes is defined by the value of $n_{\text{control points}} = 8$ and $n_{\text{cross sections}} = 10$, each resulting wing at each point will have different numbers of elements, as the optimizer seeks to eliminate structural elements that it identifies as not necessary, that is, their absence does not violate any structural or aeroelastic condition.

Moreover, in Fig. 53, two points are chosen to exemplify in this analysis: P_5 and P_6. Comparing the cost-benefit in terms of structure mass and flutter velocity, one may notice that point P_6 offers a more interesting trade-off; in other words, it can be said that the most convenient design point in this case is the point P_6. After all, compared to the lower left point (P_5), the flutter speed has increased by almost 50 m/s ($\approx +33\%$), while the weight has increased by only almost 2 kg ($\approx +6\%$).

Since for this case the number of design variables is too large, i.e., a number of 690 (see Tab. 12), a table with the resulting optimized design variables at point P will be dismissed. However, the structural mesh obtained and the corresponding distribution of diameters and thicknesses are shown below.

First, the original meshes created by Delaunay tesselation for boths points P_5 and P_6 are depicted in Fig. 54a and Fig. 55a, respectively. Then, the optimizer defines for each individual element values for the outer diameter and the tubular thickness. The possible values (search range) for these parameters were defined in the optimization problem. Furthermore, the optimizer tries to delete elements that are not needed, but ensuring the wing profile and shape. The elements excluded for this wing at point P_5 and P_6 are shown in red in Figs 54b and 55b, respectively. Consequently, the remaining resulting structural mesh for both points are arranged in Figs. 54c and 55c.

As one may notice, the number of original mesh elements on both wings (points P_5 and P_6) were equal; however, during the optimization, the algorithm defined different thicknesses and diameters for the elements, in addition to eliminating different elements that were identified as unnecessary. Thus, Tab. 13 lists the number of elements in the original and resulting mesh for the wing models at points P_5 and P_6.

Furthermore, it is possible to illustrate the distribution of outer diameter and thickness

Figure 54 – Original and remaining meshes for point P_5 from Fig. 53.

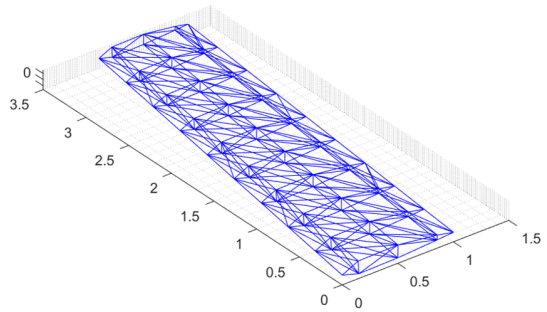

(a) Original mesh.

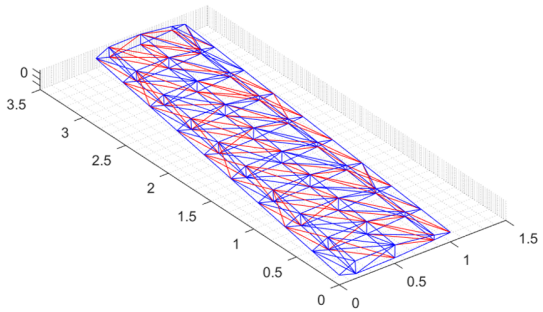

(b) Elements to be deletes in red.

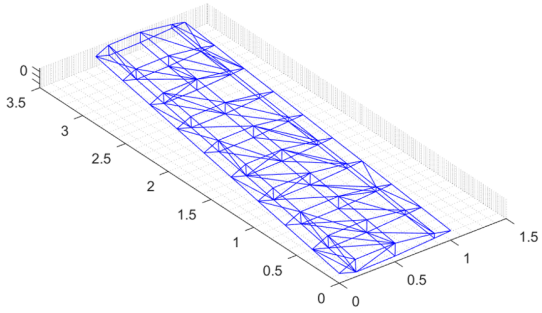

(c) Remaining mesh.

Source: Elaborated by the author.

Figure 55 – Original and remaining meshes for point P_6 from Fig. 53.

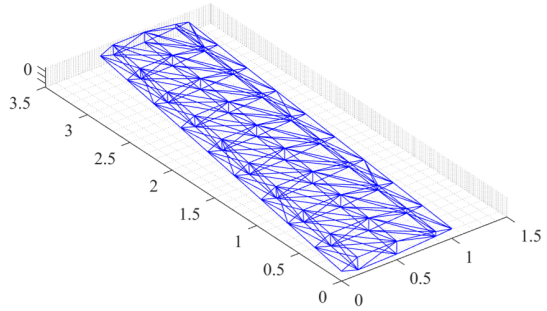

(a) Original mesh.

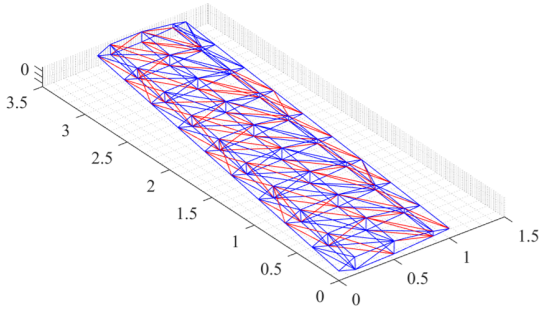

(b) Elements to be deletes in red.

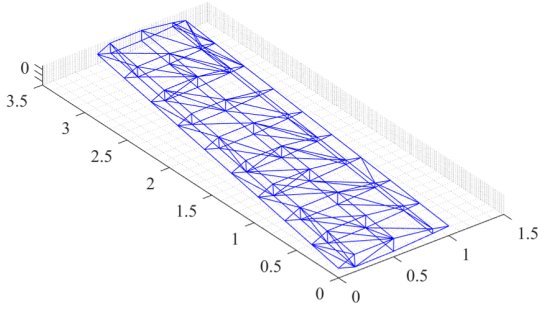

(c) Remaining mesh.

Source: Elaborated by the author.

Table 13 – Number of elements remaining in the meshes for points P_5 and P_6.

	Point P_5	Point P_6
Number of elements in original mesh	345	345
Number of elements deleted in optimization	97	102
Number of elements in remaining mesh	243	248

per element for both points P_5 and P_6. Fig. 56 shows the distribution of outside diameters, where the elements in blue, red, and orange correspond to diameters of 10, 15, and 20 mm, respectively. Also, Fig. 57 shows the distribution of thicknesses, where the elements in blue, red, and orange correspond to thicknesses of 2, 4, and 6 mm, respectively.

Figure 56 – Distribution of outer diameter each element for points P_5 and P_6 from Fig. 53.

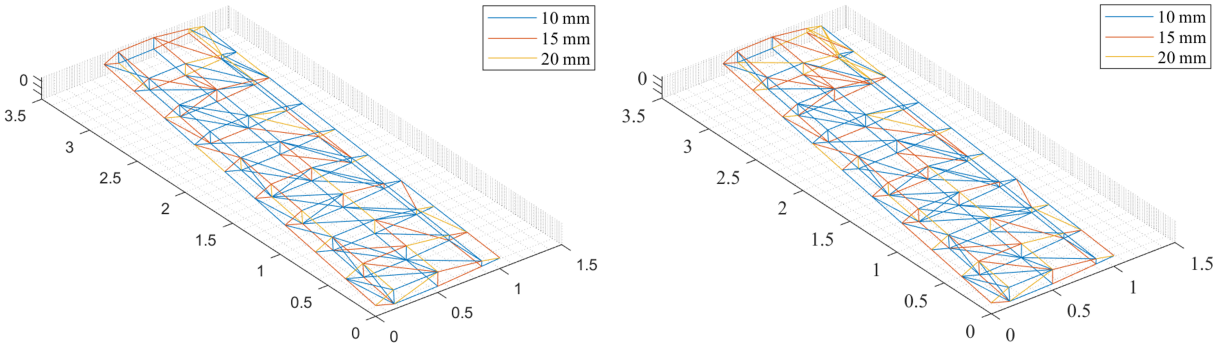

(a) Distribution for P_5. (b) Distribution for P_6.

Source: Elaborated by the author.

Figure 57 – Distribution of thickness of each element for points P_5 and P_6 from Fig. 53.

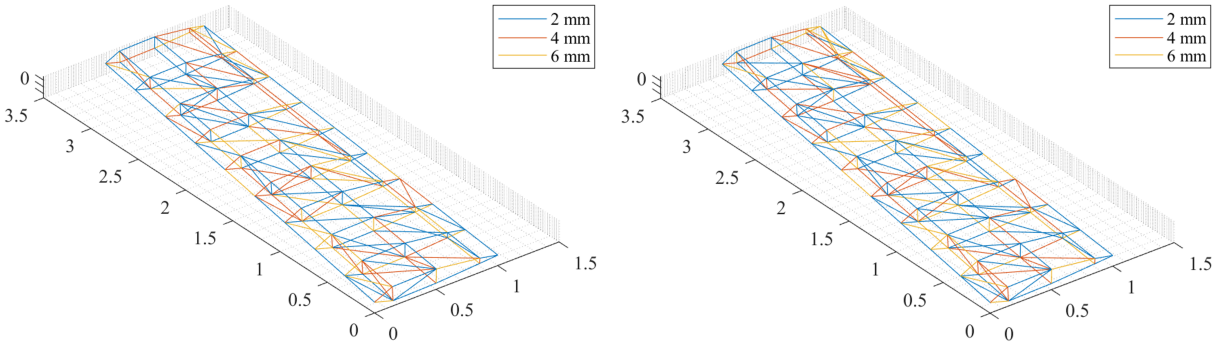

(a) Distribution for P_5. (b) Distribution for P_6.

Source: Elaborated by the author.

The choice of diameter and thickness for each element follows the heuristic optimization defined by the NSGA-II. Therefore, the resultant distributions may not represent an intuitive con-

figuration; however, at least it meets the structural and aeroelastic requirements and constraints.

Comparing the diameter and thickness distributions in Figs. 56 and 57, respectively, it is possible to notice that the wings obtained from points P_5 and P_6 change very little among themselves, so that the wing at P_6 has only 5 elements more than the wing at P_5, and the weights are very close (see Fig. 53). In addition, the distributions of diameters and thicknesses between both wings are very close, which shows that the flutter speed gain on the P_6 wing is due to specific dimension choices in some elements.

Regarding the aeroelastic solution, Fig. 58 shows the v-g-f diagrams for both points P_5 and P_6. For both points, the flutter onset happens for mode 4 due to its coupling with mode 3. Also, it can be seen that the small increase in the number of elements and the small change in the distribution of diameters and thicknesses hardly changed the initial natural frequencies; however, changes in eigenvectors generated different aeroelastic responses, which resulted in different flutter velocities.

Figure 58 – Flutter solutions for points P_5 and P_6.

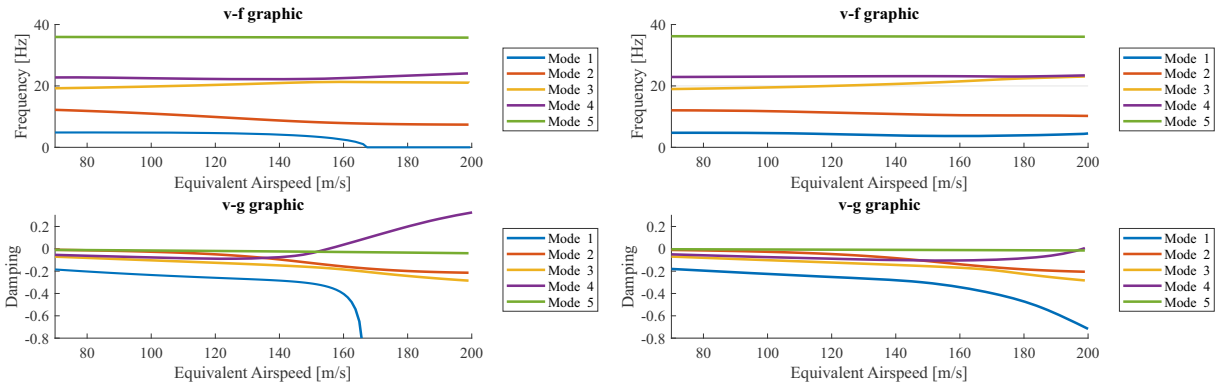

(a) V-g-f diagram for P_5.

(b) V-g-f diagram for P_6.

Source: Elaborated by the author.

Once again, due to the similar meshes and weights of the wings generated in Pareto in Fig. 53, the natural frequencies also change little along the results. Fig. 59 illustrates this small variation of natural frequencies for all Pareto points. Therefore, the aeroelastic response is not only determined by the frequencies, but by the eigenvectors obtained in the modal analysis.

Therefore, the optimizations presented here show different alternatives for the structural design of a wing. Modular structures, somehow, make possible new topological studies of

Figure 59 – Natural frequencies for each point in Pareto from Fig. 59.

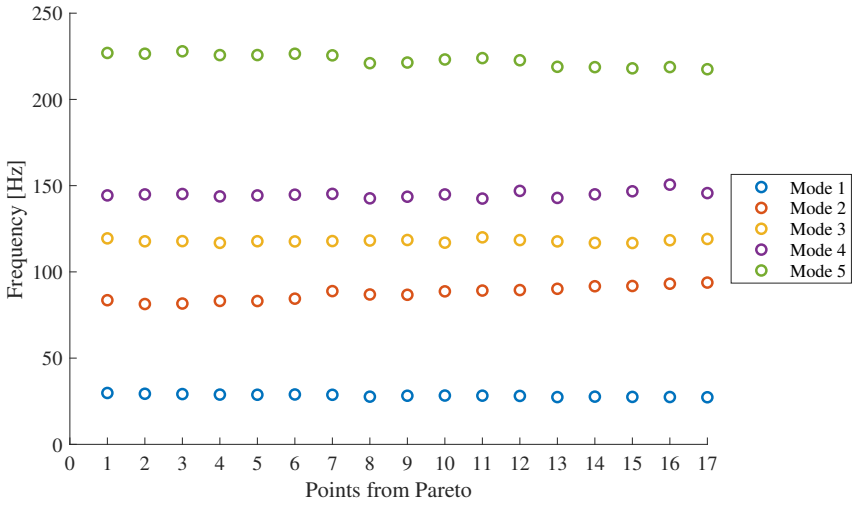

Source: Elaborated by the author.

structural meshes. However, defining the ideal topology and material properties and geometric features is still a challenge. This work, in turn, contributes to the proposed mesh generation using Delaunay and the optimization of structures. However, it is worth mentioning that the optimizations performed in this work took a long time, that is, a high computational cost; thus, better optimization time is a new challenge that will motivate future work.

Moreover, modular structures bring a range of possibilities in the structural design of wings. Among its advantages, it can be highlighted the ease of manufacture. For example, from the definition of some diameters of structures that will be used, it is possible to optimize the arrangement and the structural assembly in order to obtain the lowest weight and the best aeroelastic response. In addition, in small aircraft, such as radio-controlled aircraft or UAVs, it is possible to consider the use of modular structures manufactured in 3D printing. Such a strategy would make it possible to further increase the range of topological definition.

CHAPTER

7

CONCLUSIONS AND PERSPECTIVES

"Aviation is proof that given, the will, we have the capacity to achieve the impossible."
— Eddie Rickenbacker

THIS chapter provides the final conclusions, discussions and general remarks about the presented study. It also gives a perspective of future improvements and research branches which can be derived from the proposed methodology.

7.1 General Remarks

This work presented a new approach in structural design of wings, considering a new philosophy of design and definition of structures, that is, using modular structures in place of the traditional spars and ribs present in current models. In the design, structural and aeroelastic constraints were considered. Furthermore, the way these structures are spatially arranged generates a huge range of possibilities, a challenge that optimization tries to suppress.

Initially, the factors that motivated the choice of this theme and influenced the development of this research were presented. After all, the need to develop lighter and more efficient aircraft has triggered the industry to create disruptive design technologies and methodologies, which also includes wing designs. In addition, due to the new hybrid and electric aircraft that are appearing on the market, the wings have become increasingly elongated, more flexible and with a thinner profile, since there is no longer the need to carry fuel tanks inside. Therefore, new definitions of structures that were previously inconceivable, today become feasible under

current conditions. Modular structures, in turn, bring ease of fabrication, maintenance and weight reduction, as it is possible to design optimal structural and aeroelastic responses with the right mesh.

In this context, a review of the literature and theory was carried out, seeking contributions from studies carried out in recent years, or even in recent decades. In this way, it was possible to identify the niche of performance of this work and its contribution in the literature. After all, many works were developed in relation to topological study and structural optimization, but no work was found related to the optimization of modular structures in wings, which makes this work a pioneer in this line of research.

As this work deals with the design of a wing, it is necessary to identify the aerodynamic loads involved, mainly the unsteady ones. Thus, the Doublet-Lattice Method was used in the aerodynamic modeling, since it is a well-established method in the literature and used in aircraft certification, in addition to being implemented in commercial software. The entire formulation related to the method was presented and implemented using the Python programming language. The code was verified using reference values available in the literature. It is worth mentioning that the implementation of the DLM consumed much of the effort of this work.

Furthermore, the structural modeling of the wing was performed using two types of finite elements: beam and quadrilateral elements. The beam elements were defined from consistent Timoshenk elements and the quadrilaterals were based on Mindlin-Reissner kinematics using bi-linear interpolation and reduced integration to prevent shear locking. All the equations, theory and assumptions related to structural modeling were presented and currently it is also implemented in Python and available in the `pyfe3d` package. The code used was verified with a model in Nastran, mainly with regard to natural frequencies and modes of vibration, which directly influence the aeroelastic responses.

Later on, the aeroelastic modeling was presented. At that moment, the aerodynamic and structural modeling presented above was used. The challenge now was to make the correct coupling of the tools, that is, to generate the unsteady aerodynamic loads and make the aerostructural coupling, in order to obtain an aeroelastic response for the system. The surface spline interpolation procedure is one of the methods used to determine the structural deformations

at aerodynamic points and a linear interpolation was used to estimate the generalized aerodynamic matrices. Finally, the aeroelastic problem was solved using the p-k method, generating the v-g-f graphs, where it is possible to identify the instability and flutter conditions. All code implementation was performed in Python and verified with Nastran.

Finally, having all the tools working, that is, the aerodynamic, structural and aeroelastic modules, it was possible to design the wing proposed in this work. First, the methodology used to generate the structure mesh was presented. From an airfoil, a set of interpolation points is defined, called control points, which will be the connection nodes of the truss elements. Then, Delaunay's triangulation theory is used to generate a spatial mesh arrangement with as many elements as possible, without them intersecting. Furthermore, the choice of joint that connects these elements is essential, as it introduces mass into the system and is responsible for design constraints.

Moreover, for this study, the reference wing geometry from the FLEXOP project is used as a baseline, that is, a wing design study was carried out using the main dimensions of the wing available in FLEXOP. Thus, to improve the definition of the mesh and the dimensions of the lattice elements, two optimizations were proposed, where the objective functions were to minimize the weight of the wing and maximize the flutter speed. In the first optimization, the design variables included the number of control points in each section of the airfoil and the number of sections distributed along the wingspan. In this case, solid bar elements were considered, which resulted in very heavy designs. In the second optimization, in turn, the objective was to use tubular elements and optimize them individually, choosing for each element values of outer diameter and tubular thickness. In addition, the optimizer tried to eliminate elements that were unnecessary, in order to further reduce the weight of the structure. As the number of elements varies according to the number of nodes in each section and the section number, this work selected three pairs of parameters to generate the Paretos. It was noticed that a lower value of nodes and cross sections is able to generate a better cost-benefit in terms of weight and aeroelastic response to the structure, as long as the diameters and thicknesses are optimally combined.

Finally, this work showed how modular structures can become a great strategy in the

design of aeronautical structures, specifically wings. The new wing models that are currently being presented in the literature, mainly on electric aircraft, have increasingly thin aerodynamic profiles, since there is no longer the need to house fuel tanks. In this sense, modular structures would be interesting to lighten the structural weight of the wing and at the same time meet the structural and aeroelastic requirements. Furthermore, modular structures bring ease of fabrication as it is possible to choose some specific tube diameters and just cut the required tube sizes. Furthermore, in smaller aircraft, such as radio-controlled and UAVs, 3D printing can become an interesting alternative in the manufacture of such structures.

7.2 Future Perspectives

This work opens a range of opportunities for future work, since the use of modular structures in wing designs is a new strand in the literature and there is still much to be explored. Therefore, the following suggestions are proposed as future work:

- Improve the optimization method and make it faster and more efficient, since much of the time spent is still in the optimization;
- Better study the definitions of parameters and optimization variables, that is, number of control points, numbers of sections, diameters, thicknesses, and materials;
- Study in more detail the dimensioning and sizing of the joint and how it would generate constraints for the structural design and for the optimization;
- Make an experimental model, either in metallic structures or in 3D printing, in order to validate the study;
- Integrate this wing design methodology into other applications and into complete aircraft designs, as in an MDO (multidisciplinary design optimization), where the structural design of the wing would be directly related to aerodynamic, stability and cost requirements.
- Further explore the idea of modularity and its benefits in terms of manufacturing and maintenance.

BIBLIOGRAPHY

AAGE, N.; ANDREASSEN, E.; LAZAROV, B. S.; SIGMUND, O. Giga-voxel computational morphogenesis for structural design. **Nature**, Nature Publishing Group, v. 550, n. 7674, p. 84–86, 2017. DOI: <https://doi.org/10.1038/nature23911>. Citation on page 46.

ACARE, Advisory Council for Aviation Research Innovation in Europe. Realising europe's vision for aviation: Strategic research & innovation agenda, vol. 1. 2012. Citation on page 29.

ADAM, F. M.; MOHAMED, A. E.; HASSABALLA, A. E. Degenerated Four Nodes Shell Element with Drilling Degree of Freedom. **IOSR Journal of Engineering**, v. 3, n. 8, p. 10–20, 2013. DOI: <http://dx.doi.org/10.9790/3021-03831020>. Available: <http://www.iosrjen.org>. Citation on page 101.

AFONSO, F.; VALE, J.; OLIVEIRA, É.; LAU, F.; SULEMAN, A. A review on non-linear aeroelasticity of high aspect-ratio wings. **Progress in Aerospace Sciences**, Elsevier, v. 89, p. 40–57, 2017. DOI: <https://doi.org/10.1016/j.paerosci.2016.12.004>. Citation on page 30.

AIRBUS reveals new zero-emission concept aircraft. **Airbus**, Airbus, Sep 2020. Available: <https://www.airbus.com/newsroom/press-releases/en/2020/09/airbus-reveals-new-zeroemission-concept-aircraft.html>. Citation on page 30.

ALBANO, E.; RODDEN, W. P. A doublet-lattice method for calculating lift distributions on oscillating surfaces in subsonic flows. **AIAA journal**, v. 7, n. 2, p. 279–285, 1969. DOI: <https://doi.org/10.2514/3.5086>. Citations on pages 64, 65, 66, and 67.

ANDERSON, J. **Fundamentals of Aerodynamics (SI units)**. [S.l.]: McGraw hill, 2011. Citations on pages 52, 53, and 54.

ARNHEITER, E. D.; HARREN, H. A typology to unleash the potential of modularity. **Journal of Manufacturing Technology Management**, Emerald Group Publishing Limited, 2005. DOI: <https://doi.org/10.1108/17410380510619923>. Citation on page 47.

ASAN, U.; POLAT, S.; SERDAR, S. An integrated method for designing modular products. **Journal of Manufacturing Technology Management**, Emerald Group Publishing Limited, 2004. DOI: <https://doi.org/10.1108/09576060410512257>. Citation on page 47.

AYDINCILAR, Y. **Optimum design of double-layer grid systems: comparison with current design practice using real-life industrial applications**. Master's Thesis (Master's Thesis) — Middle East Technical University, 2010. URI: <https://hdl.handle.net/11511/19802>. Citation on page 143.

BABUSKA, I.; D'HARCOURT, J.; SCHWAB, C. **Optimal Shear Correction Factors in Hierarchical Plte Modelling**. [S.l.], 1991. Citation on page 94.

BALABANOV, V. O.; HAFTKA, R. T. Topology optimization of transport wing internal structure. **Journal of aircraft**, v. 33, n. 1, p. 232–233, 1996. DOI: <https://doi.org/10.2514/3.46926>. Citation on page 42.

BALDWIN, C.; CLARK, K. Managing in an age of modularity. **Harvard Business Review**, v. 75, n. 5, p. 84–93, 1997. Citation on page 47.

BALDWIN, C. Y.; CLARK, K. B.; CLARK, K. B. *et al.* **Design rules: The power of modularity**. [S.l.]: MIT press, 2000. DOI: <https://doi.org/10.7551/mitpress/2366.001.0001>. Citation on page 47.

BARTELS, R. E.; SCOTT, R. C.; ALLEN, T.; SEXTON, B. Aeroelastic analysis of sugar truss-braced wing wind-tunnel model using fun3d and a nonlinear structural model. In: **56th AIAA/ASCE/AHS/ASC Structures, Structural Dynamics, and Materials Conference**. [S.l.: s.n.], 2015. p. 1174. DOI: <https://doi.org/10.2514/6.2015-1174>. Citation on page 29.

BECKEN, S.; MACKEY, B. What role for offsetting aviation greenhouse gas emissions in a deep-cut carbon world? **Journal of Air Transport Management**, Elsevier, v. 63, p. 71–83, 2017. DOI: <https://doi.org/10.1016/j.jairtraman.2017.05.009>. Citation on page 29.

BECKER, E. **KARAMCHETI, K-PRINCIPLES OF IDEAL-FLUID AERODYNAMICS**. 1967. Citations on pages 57 and 58.

BENDSØE, M. P.; KIKUCHI, N. Generating optimal topologies in structural design using a homogenization method. **Computer methods in applied mechanics and engineering**, Elsevier, v. 71, n. 2, p. 197–224, 1988. DOI: <https://doi.org/10.1016/0045-7825(88)90086-2>. Citation on page 42.

BENDSØE, M. P.; SIGMUND, O. Material interpolation schemes in topology optimization. **Archive of applied mechanics**, Springer, v. 69, n. 9, p. 635–654, 1999. DOI: <https://doi.org/10.1007/s004190050248>. Citation on page 43.

BISPLINGHOFF, R. L.; ASHLEY, H.; HALFMAN, R. L. **Aeroelasticity**. [S.l.]: Courier Corporation, 1996. Citation on page 55.

BLAIR, M. **A compilation of the mathematics leading to the doublet lattice method**. [S.l.], 1994. Citations on pages 19, 52, 54, 55, 56, 58, 72, 74, 75, and 76.

BONET, J. T.; SCHELLENGER, H. G.; RAWDON, B. K.; ELMER, K. R.; WAKAYAMA, S. R.; BROWN, D. L.; GUO, Y. Environmentally responsible aviation (era) project-n+ 2 advanced vehicle concepts study and conceptual design of subscale test vehicle (stv) final report. 2011. Citation on page 29.

BORER, N. K.; PATTERSON, M. D.; VIKEN, J. K.; MOORE, M. D.; BEVIRT, J.; STOLL, A. M.; GIBSON, A. R. Design and performance of the nasa sceptor distributed electric propulsion flight demonstrator. In: **16th AIAA Aviation Technology, Integration, and Operations Conference**. [S.l.: s.n.], 2016. p. 3920. DOI: <https://doi.org/10.2514/6.2016-3920>. Citation on page 29.

BOWMAN, J.; SANDERS, B.; CANNON, B.; KUDVA, J.; JOSHI, S.; WEISSHAAR, T. Development of next generation morphing aircraft structures. In: **48th AIAA/ASME/ASCE/AHS/ASC Structures, Structural Dynamics, and Materials Conference**. [S.l.: s.n.], 2007. p. 1730. DOI: <https://doi.org/10.2514/6.2007-1730>. Citation on page 29.

BRADLEY, M. K.; DRONEY, C. K. Subsonic ultra green aircraft research. 2011. Citation on page 30.

BRELJE, B. J.; MARTINS, J. R. Electric, hybrid, and turboelectric fixed-wing aircraft: A review of concepts, models, and design approaches. **Progress in Aerospace Sciences**, Elsevier, v. 104, p. 1–19, 2019. DOI: <https://doi.org/10.1016/j.paerosci.2018.06.004>. Citations on pages 29 and 36.

BROCKMAN, R. A. Dynamics of the bilinear Mindlin plate element. **International Journal for Numerical Methods in Engineering**, v. 24, n. 12, p. 2343–2356, 1987. ISSN 10970207. DOI: <https://doi.org/10.1002/nme.1620241208>. Available: <http://doi.wiley.com/10.1002/nme.1620241208>. Citations on pages 100 and 102.

BROOKS, T. R.; MARTINS, J. R. On manufacturing constraints for tow-steered composite design optimization. **Composite structures**, Elsevier, v. 204, p. 548–559, 2018. DOI: <https://doi.org/10.1016/j.compstruct.2018.07.100>. Citation on page 41.

CAGLAYAN, O.; YUKSEL, E. Experimental and finite element investigations on the collapse of a mero space truss roof structure–a case study. **Engineering Failure Analysis**, Elsevier, v. 15, n. 5, p. 458–470, 2008. DOI: <https://doi.org/10.1016/j.engfailanal.2007.05.005>. Citation on page 143.

CASTRO, S. G. P. **General-purpose finite element solver based on Python and Cython**. [S.l.]: Zenodo, 2022. DOI: <https://doi.org/10.5281/zenodo.6573490>. Citations on pages 77, 107, and 125.

____. **Lecture notes in AE4ASM511 Stability and Analysis of Structures II**. [S.l.]: Delft University of Technology, Aerospace Structures and Materials, 2022. Citations on pages 77, 78, 86, 90, 92, and 96.

CHEDRIK, V.; TUKTAROV, S. Structural design of aircraft wing based on topology and global-local optimization. In: **11th World Congress on Structural and Multidisciplinary Optimisation**. [S.l.: s.n.], 2015. DOI: <http://dx.doi.org/10.1615/TsAGISciJ.2017020620>. Citation on page 45.

CHEN, W.-F.; LUI, E. **Structural engineering handbook**. [S.l.]: Boca Raton: CRC Press LLC, 1999. Citations on pages 142 and 143.

CHOI, J.-S.; ZHAO, L.; PARK, G.-J.; AGRAWAL, S. K.; KOLONAY, R. M. Enhancement of a flapping wing using path and dynamic topology optimization. **AIAA journal**, v. 49, n. 12, p. 2616–2626, 2011. DOI: <https://doi.org/10.2514/1.J050834>. Citation on page 43.

CLOUGH, R.; PENZIEN, J. **Dynamics of Structures**. [S.l.]: McGraw-Hill, 1975. Citations on pages 110, 112, and 113.

COLLAR, A. R. The expanding domain of aeroelasticity. **The Aeronautical Journal**, Cambridge University Press, v. 50, n. 428, p. 613–636, 1946. DOI: <10.1017/S0368393100120358>. Citation on page 109.

DAVIES, R. M. Space structures: A study of methods and developments in three-dimensional construction resulting from the international conference on space structures. Blackwell scientific publications, 1967. Citation on page 142.

DEB, K.; PRATAP, A.; AGARWAL, S.; MEYARIVAN, T. A fast and elitist multiobjective genetic algorithm: Nsga-ii. **IEEE transactions on evolutionary computation**, IEEE, v. 6, n. 2, p. 182–197, 2002. Citations on pages 147 and 148.

DIJK, N. P. V.; MAUTE, K.; LANGELAAR, M.; KEULEN, F. V. Level-set methods for structural topology optimization: a review. **Structural and Multidisciplinary Optimization**, Springer, v. 48, n. 3, p. 437–472, 2013. DOI: <https://doi.org/10.1007/s00158-013-0912-y>. Citation on page 45.

DORAN, D. Supply chain implications of modularization. **International Journal of Operations & Production Management**, MCB UP Ltd, 2003. DOI: <https://doi.org/10.1108/01443570310462785>. Citation on page 47.

____. Rethinking the supply chain: an automotive perspective. **Supply Chain Management: An International Journal**, Emerald Group Publishing Limited, 2004. DOI: <http://dx.doi.org/10.1108/13598540410517610>. Citation on page 47.

____. Supplying on a modular basis: an examination of strategic issues. **International Journal of Physical Distribution & Logistics Management**, Emerald Group Publishing Limited, 2005. DOI: <https://doi.org/10.1108/09600030510632023>. Citation on page 47.

DRELA, M. Development of the d8 transport configuration. In: **29th AIAA Applied Aerodynamics Conference**. [S.l.: s.n.], 2011. p. 3970. DOI: <https://doi.org/10.2514/6.2011-3970>. Citation on page 30.

DUNNING, P. D.; STANFORD, B.; KIM, H. A.; JUTTE, C. V. Aeroelastic tailoring of a plate wing with functionally graded materials. **Journal of Fluids and Structures**, v. 51, p. 292–312, 2014. DOI: <https://doi.org/10.1016/j.jfluidstructs.2014.09.008>. Citation on page 42.

DUNNING, P. D.; STANFORD, B. K.; KIM, H. A. Coupled aerostructural topology optimization using a level set method for 3d aircraft wings. **Structural and Multidisciplinary Optimization**, Springer, v. 51, n. 5, p. 1113–1132, 2015. DOI: <https://doi.org/10.1007/s00158-014-1200-1>. Citation on page 45.

DUNNING, P. D.; STANFORD, B. K.; KIM, H. A.; JUTTE, C. V. Aeroelastic tailoring of a plate wing with functionally graded materials. **Journal of Fluids and Structures**, Elsevier, v. 51, p. 292–312, 2014. DOI: <https://doi.org/10.1016/j.jfluidstructs.2014.09.008>. Citation on page 41.

EBADI, M.; DAVOODI, M. Evaluate axial stiffness of the mero connection, under the effect of hardening the screw. **Int. J. Sci. Emerg. Technol**, v. 4, n. 1, p. 116–122, 2012. Citation on page 143.

ELIJAH, T.; JAMISOLA, R. S.; TJIPARURO, Z.; NAMOSHE, M. A review on control and maneuvering of cooperative fixed-wing drones. **International Journal of Dynamics and Control**, Springer, v. 9, n. 3, p. 1332–1349, 2021. DOI: <https://doi.org/10.1007/s40435-020-00710-2>. Citation on page 37.

ERNST, D. Limits to modularity: reflections on recent developments in chip design. **Industry and Innovation**, Taylor & Francis, v. 12, n. 3, p. 303–335, 2005. DOI: <https://doi.org/10.1080/13662710500195918>. Citation on page 47.

ESCHENAUER, H.; OLHOFF, N. Topology optimization of continuum structures: A review'applied mechanics review. 2001. DOI: <http://dx.doi.org/10.1115/1.1388075>. Citation on page 43.

FILHO, L. S. Analise tridimensional de edificios por elementos finitos utilizando programação orientada a objetos. Universidade Estadual de Campinas, 1997. Citation on page 90.

FINISTAURI, A. D.; XI, F.; WALSH, P. Discretization method for the development of a modular morphing wing. **Journal of Aircraft**, v. 49, n. 1, p. 116–125, 2012. DOI: <https://doi.org/10.2514/1.C031382>. Citation on page 48.

Flight Literacy. **Effect of Wing Planform**. 2022. <https://www.flightliteracy.com/effect-of-wing-planform/>, Last accessed on 2022-04-23. Citation on page 39.

FREDRIKSSON, P. Operations and logistics issues in modular assembly processes: cases from the automotive sector. **Journal of Manufacturing Technology Management**, Emerald Group Publishing Limited, 2006. DOI: <https://doi.org/10.1108/17410380610642250>. Citation on page 47.

FRIEDMANN, P. P. Renaissance of aeroelasticity and its future. **Journal of aircraft**, v. 36, n. 1, p. 105–121, 1999. DOI: <https://doi.org/10.2514/2.2418>. Citation on page 110.

GAO, Y.-Q.; TANG, T.-Q.; ZHANG, J.; YOU, F. Which aircraft has a better fuel efficiency?–a case study in china. **Transportmetrica B: Transport Dynamics**, Taylor & Francis, v. 10, n. 1, p. 1032–1045, 2022. DOI: <https://doi.org/10.1080/21680566.2021.1997674>. Citation on page 36.

GEORGE, P.; HERMELINE, F. Delaunay's mesh of a convex polyhedron in dimension d. application to arbitrary polyhedra. **International Journal for Numerical Methods in Engineering**, Wiley Online Library, v. 33, n. 5, p. 975–995, 1992. DOI: <https://doi.org/10.1002/nme.1620330507>. Citation on page 135.

GHADGE, A.; KARANTONI, G.; CHAUDHURI, A.; SRINIVASAN, A. Impact of additive manufacturing on aircraft supply chain performance. **Journal of Manufacturing Technology Management**, Emerald Publishing Limited, 2018. DOI: <http://dx.doi.org/10.1108/JMTM-07-2017-0143>. Citation on page 29.

GIESING, J. Basic principles and doublet lattice applications in potential aerodynamics. **McDonnell Douglas Corporation, Long Beach, Ca., no further reference available**, 1985. Citation on page 60.

GOLDBERG, D. E. Genetic algorithms in search, optimization, and machine learning. Addison-Wesley Longman Publishing Co. Inc., USA, 1989. Citation on page 147.

GREENWELL, D. A review of unsteady aerodynamic modelling for flight dynamics of manoeuvrable aircraft. In: **AIAA atmospheric flight mechanics conference and exhibit**. [S.l.: s.n.], 2004. p. 5276. DOI: <https://doi.org/10.2514/6.2004-5276>. Citation on page 52.

GRÖNSTEDT, T.; XISTO, C.; SETHI, V.; ROLT, A.; ROSA, N. G.; SEITZ, A.; YAKINTHOS, K.; DONNERHACK, S.; NEWTON, P.; TANTOT, N. *et al.* Ultra low emission technology innovations for mid-century aircraft turbine engines. In: AMERICAN SOCIETY OF MECHANICAL ENGINEERS. **Turbo Expo: Power for Land, Sea, and Air**. [S.l.], 2016. v. 49743, p. V003T06A001. DOI: <https://doi.org/10.1115/GT2016-56123>. Citation on page 29.

GUIMARÃES, T. A. M. *et al.* Contribuição ao estudo do comportamento dinâmico e aeroelástico de laminados compósitos de rigidez variável. Universidade Federal de Uberlândia, 2016. DOI: <http://doi.org/10.14393/ufu.te.2016.163>. Citation on page 41.

GÜLÇAT, Ü. **Fundamentals of modern unsteady aerodynamics**. [S.l.]: Springer, 2010. DOI: <https://doi.org/10.1007/978-981-10-0018-8>. Citations on pages 51 and 52.

GUO, Q. **Developing optimal mass matrices for membrane triangles with corner drilling freedoms**. Phd Thesis (PhD Thesis) — University of Colorado at Boulder, 2012. Citation on page 102.

HARDER, R. L.; DESMARAIS, R. N. Interpolation using surface splines. **Journal of aircraft**, v. 9, n. 2, p. 189–191, 1972. DOI: <https://doi.org/10.2514/3.44330>. Citation on page 115.

HASAN, M. A.; MAMUN, A. A.; RAHMAN, S. M.; MALIK, K.; AMRAN, M. A.; UDDIN, I.; KHONDAKER, A. N.; RESHI, O.; TIWARI, S. P.; ALISMAIL, F. S. Climate change mitigation pathways for the aviation sector. **Sustainability**, Multidisciplinary Digital Publishing Institute, v. 13, n. 7, p. 3656, 2021. DOI: <https://doi.org/10.3390/su13073656>. Citation on page 36.

HEDMAN, S. G. **Vortex lattice method for calculation of quasi steady state loadings on thin elastic wings in subsonic flow**. [S.l.], 1966. Citation on page 66.

Hephaist. **SR Joint - Precision and Rigidity**. 2022. <http://www.myostat.ca/imagequalitylabs>, Last accessed on 2022-05-23. Citation on page 143.

HOLLAND, J. H. **Adaptation in natural and artificial systems: an introductory analysis with applications to biology, control, and artificial intelligence**. [S.l.]: MIT press, 1992. Citation on page 147.

JACOBS, M.; VICKERY, S. K.; DROGE, C. The effects of product modularity on competitive performance: do integration strategies mediate the relationship? **International Journal of Operations & Production Management**, Emerald Group Publishing Limited, 2007. DOI: <http://dx.doi.org/10.1108/01443570710820620>. Citation on page 47.

JAMES, K. A.; KENNEDY, G. J.; MARTINS, J. R. Concurrent aerostructural topology optimization of a wing box. **Computers & Structures**, Elsevier, v. 134, p. 1–17, 2014. DOI: <https://doi.org/10.1016/j.compstruc.2013.12.007>. Citation on page 44.

JANSEN, P.; PEREZ, R. Effect of size and mission requirements on the design optimization of non-planar aircraft configurations. In: **13th AIAA/ISSMO Multidisciplinary Analysis Optimization Conference**. [S.l.: s.n.], 2010. p. 9188. DOI: <https://doi.org/10.2514/6.2010-9188>. Citation on page 37.

JIAO, J.; TSENG, M. M. Fundamentals of product family architecture. **Integrated Manufacturing Systems**, MCB UP Ltd, 2000. DOI: <http://dx.doi.org/10.1108/09576060010349776>. Citation on page 47.

JOSE, A.; TOLLENAERE, M. Modular and platform methods for product family design: literature analysis. **Journal of Intelligent manufacturing**, Springer, v. 16, n. 3, p. 371–390, 2005. DOI: <https://doi.org/10.1007/s10845-005-7030-7>. Citations on pages 47 and 48.

JUVE, L.; FOSSE, J.; JOUBERT, E.; FOUQUET, N. Airbus group electrical aircraft program, the e-fan project. In: **52nd AIAA/SAE/ASEE Joint Propulsion Conference**. [S.l.: s.n.], 2016. p. 4613. URL: <https://commons.erau.edu/edt/110/>. Citation on page 29.

KAMBAMPATI, S.; TOWNSEND, S.; KIM, H. A. Coupled aerostructural level set topology optimization of aircraft wing boxes. **AIAA Journal**, American Institute of Aeronautics and Astronautics, v. 58, n. 8, p. 3614–3624, 2020. DOI: <https://doi.org/10.2514/1.J059157>. Citation on page 46.

KANG, M.-C.; YE, D.-H.; GO, G.-H. International development trend and technical issues of metal additive manufacturing. **Journal of Welding and Joining**, The Korean Welding and Joining Society, v. 34, n. 4, p. 9–16, 2016. DOI: <https://doi.org/10.5781/JWJ.2016.34.4.9>. Citation on page 29.

KENNEDY, G.; MARTINS, J. R. A comparison of metallic and composite aircraft wings using aerostructural design optimization. In: **12th AIAA Aviation Technology, Integration, and Operations (ATIO) Conference and 14th AIAA/ISSMO Multidisciplinary Analysis and Optimization Conference**. [S.l.: s.n.], 2012. p. 5475. DOI: <https://doi.org/10.2514/6.2012-5475>. Citation on page 40.

KENWAY, G.; KENNEDY, G.; MARTINS, J. R. Aerostructural optimization of the common research model configuration. In: **15th AIAA/ISSMO multidisciplinary analysis and optimization conference**. [S.l.: s.n.], 2014. p. 3274. DOI: <https://doi.org/10.2514/6.2014-3274>. Citation on page 44.

KOLONAY, R. M.; KOBAYASHI, M. H. Optimization of aircraft lifting surfaces using a cellular division method. **Journal of Aircraft**, American Institute of Aeronautics and Astronautics, v. 52, n. 6, p. 2051–2063, 2015. DOI: <https://doi.org/10.2514/1.C033138>. Citation on page 44.

KROG, L.; TUCKER, A.; KEMP, M.; BOYD, R. Topology optimisation of aircraft wing box ribs. In: **10th AIAA/ISSMO multidisciplinary analysis and optimization conference**. [S.l.: s.n.], 2004. p. 4481. DOI: <https://doi.org/10.2514/6.2004-4481>. Citation on page 43.

LAN, T. T. Space frame structures. **Structural engineering handbook**, CRC Press LLC Boca Raton, v. 13, n. 4, 1999. Citations on pages 142 and 143.

LANDAHL, M. Kernel function for nonplanar oscillating surfaces in a subsonic flow. **AIAA Journal**, v. 5, n. 5, p. 1045–1046, 1967. DOI: <https://doi.org/10.2514/3.55319>. Citation on page 62.

LAPEÑA-REY, N.; MOSQUERA, J.; BATALLER, E.; ORTÍ, F. First fuel-cell manned aircraft. **Journal of aircraft**, v. 47, n. 6, p. 1825–1835, 2010. DOI: <https://doi.org/10.2514/1.42234>. Citation on page 29.

LASCHKA, B. Das potential und das geschwindigkeitsfeld der harmonisch schwingenden tragenden fläche bei unterschallströmung. **ZAMM-Journal of Applied Mathematics and Mechanics/Zeitschrift für Angewandte Mathematik und Mechanik**, Wiley Online Library, v. 43, n. 7-8, p. 325–333, 1963. Citations on pages 63 and 64.

LAU, A. K.; YAM, R. C.; TANG, E. P. Supply chain product co-development, product modularity and product performance: empirical evidence from hong kong manufacturers. **Industrial Management & Data Systems**, Emerald Group Publishing Limited, 2007. DOI: <https://doi.org/10.1108/02635570710816739>. Citation on page 47.

LAWSON, C. L. Software for c1 surface interpolation. In: **Mathematical software**. [S.l.]: Elsevier, 1977. p. 161–194. DOI: <https://doi.org/10.1016/B978-0-12-587260-7.50011-X>. Citation on page 137.

LEBENSZTAJN, L.; FALCONE, A. G. Desenvolvimento de pré e pós processadores para o método dos elementos finitos aplicados a conversão eletromecânica de energia. 1989. Citation on page 136.

LOBATO, F. **Otimização multi-objetivo para o projeto de sistemas de engenharia, 2008**. Phd Thesis (PhD Thesis) — Tese de Doutorado - Programa de Pós-Graduação em Engenharia Mecânica, 2008. URI: <https://repositorio.ufu.br/handle/123456789/14677>. Citation on page 148.

LOCATELLI, D.; MULANI, S. B.; KAPANIA, R. K. Wing-box weight optimization using curvilinear spars and ribs (sparibs). **Journal of Aircraft**, v. 48, n. 5, p. 1671–1684, 2011. DOI: <https://doi.org/10.2514/1.C031336>. Citation on page 44.

LUO, Y. An Efficient 3D Timoshenko Beam Element with Consistent Shape Functions. **Adv. Theor. Appl. Mech.**, v. 1, n. 3, p. 95–106, 2008. DOI: <>. Citations on pages 77 and 78.

MACHADO, J. M.; CARDOSO, J. R. Lmag-3d: Um software cad/cae para eletromagnetismo baseado no método dos elementos finitos em 3d. 1993. Citation on page 138.

MAKOWSKI, Z. **Analysis, Design and Construction of Steel Space Frames**. [S.l.]: SAGE Publications Sage UK: London, England, 2002. DOI: <https://doi.org/10.1260/026635102320321905>. Citation on page 142.

MARRETTO, C. O algaritmo de delaunay em três dimensões: Uma implementação computacional para o ambiente mathematica for windows. Universidade Estadual Paulista (Unesp), 1999. Citations on pages 135 and 136.

MARSH, G. Airbus takes on boeing with reinforced plastic a350 xwb. **Reinforced plastics**, Elsevier, v. 51, n. 11, p. 26–29, 2007. DOI: <https://doi.org/10.1016/S0034-3617(07)70383-1>. Citation on page 40.

MARTINS, J.; KENNEDY, G.; KENWAY, G. K. High aspect ratio wing design: Optimal aerostructural tradeoffs for the next generation of materials. In: **52nd Aerospace Sciences Meeting**. [S.l.: s.n.], 2014. p. 0596. DOI: <https://doi.org/10.2514/6.2014-0596>. Citation on page 30.

MAUTE, K.; ALLEN, M. Conceptual design of aeroelastic structures by topology optimization. **Structural and Multidisciplinary Optimization**, Springer, v. 27, n. 1, p. 27–42, 2004. DOI: <https://doi.org/10.1007/s00158-003-0362-z>. Citation on page 43.

MEDDAIKAR, M. Y.; DILLINGER, J.; SODJA, J.; BREUKER, R. D. Flexop – application of aeroelastic tailoring to a flying demonstrator wing. In: **Deutscher Luft- und Raumfahrtkongress 2018**. [S.l.: s.n.], 2018. DLRK 2018 : Deutscher Luft- und Raumfahrtkongress, DLRK 2018 ; Conference date: 04-09-2018 Through 06-09-2018. Citation on page 144.

MEIROVITCH, L. **Elements of vibration analysis((Book))**. [S.l.: s.n.], 1986. Citations on pages 110, 111, and 112.

MIDTBO, T. Incremental delaunay tetrahedrization for adaptive data modelling. In: **Proceedings of the Fourth European Conference and Exhibition on Geographical Information Systems, EGIS**. [S.l.: s.n.], 1993. v. 93, p. 227–236. Citation on page 138.

MONTEMURRO, M.; VINCENTI, A.; VANNUCCI, P. A two-level procedure for the global optimum design of composite modular structures—application to the design of an aircraft wing. **Journal of Optimization Theory and Applications**, Springer, v. 155, n. 1, p. 24–53, 2012. DOI: <https://doi.org/10.1007/s10957-012-0067-9>. Citations on pages 31 and 48.

MOORE, M. Aviation frontiers-on demand aircraft. In: **10th AIAA Aviation Technology, Integration, and Operations (ATIO) Conference**. [S.l.: s.n.], 2010. p. 9343. DOI: <http://dx.doi.org/10.2514/6.2010-9343>. Citation on page 29.

MOSES, E.; FUCHS, M.; RYVKIN, M. Topological design of modular structures under arbitrary loading. **Structural and Multidisciplinary Optimization**, Springer, v. 24, n. 6, p. 407–417, 2002. DOI: <https://doi.org/10.1007/s00158-002-0254-7>. Citation on page 31.

MRAZOVA, M. Advanced composite materials of the future in aerospace industry. **Incas bulletin**, INCAS-National Institute for Aerospace Research" Elie Carafoli", v. 5, n. 3, p. 139, 2013. DOI: <http://dx.doi.org/10.13111/2066-8201.2013.5.3.14>. Citation on page 40.

NAAYAGI, R. A review of more electric aircraft technology. In: IEEE. **2013 international conference on energy efficient technologies for sustainability**. [S.l.], 2013. p. 750–753. DOI: <https://doi.org/10.1109/ICEETS.2013.6533478>. Citation on page 29.

NANDA, A. The propulsive design aspects on the world's first direct drive hybrid airplane. 2011. DOI: <>. Citation on page 29.

NASTRAN, M. Aeroelastic analysis user's guide. **MSC Software Corporation**, 2021. Citation on page 117.

NOGUEIRA, J. R.; OLIVEIRA, S. Gonzaga de. Introduction to triangular mesh generation and the delaunay triangulation. In: **Proceedings of the XXXII Iberian Latin-American Congress on Computational Methods in Engineering-XXXII CILAMCE (Mini-symposia Research Beginners on Computational Methods in Engineering). Ouro Preto: ABMEC**. [S.l.: s.n.], 2011. Citation on page 137.

NOUR-OMID, B.; RANKIN, C. Finite rotation analysis and consistent linearization using projectors. **Computer Methods in Applied Mechanics and Engineering**, Elsevier, v. 93, n. 3, p. 353–384, 1991. DOI: <https://doi.org/10.1016/0045-7825(91)90248-5>. Citation on page 78.

OKTAY, E.; AKAY, H.; MERTTOPCUOGLU, O. Parallelized structural topology optimization and cfd coupling for design of aircraft wing structures. **Computers & Fluids**, Elsevier, v. 49, n. 1, p. 141–145, 2011. DOI: <https://doi.org/10.1016/j.compfluid.2011.05.005>. Citation on page 45.

OÑATE, E. **Structural analysis with the finite element method. Linear statics: volume 2: beams, plates and shells**. [S.l.]: Springer Science & Business Media, 2013. DOI: <https://doi.org/10.1007/978-1-4020-8743-1>. Citation on page 90.

OPGENOORD, M. M.; WILLCOX, K. E. Design methodology for aeroelastic tailoring of additively manufactured lattice structures using low-order methods. **AIAA Journal**, American Institute of Aeronautics and Astronautics, v. 57, n. 11, p. 4903–4914, 2019. DOI: <https://doi.org/10.2514/1.J058169>. Citations on pages 46 and 133.

ÖSTERHELD, C.; HEINZE, W.; HORST, P. Influence of aeroelastic effects on preliminary aircraft design. In: **Proceedings of the ICAS-Congress, Harrogate**. [S.l.: s.n.], 2000. Citation on page 30.

PACOSTE, C.; ERIKSSON, A. Beam elements in instability problems. **Computer methods in applied mechanics and engineering**, Elsevier, v. 144, n. 1-2, p. 163–197, 1997. DOI: <https://doi.org/10.1016/S0045-7825(96)01165-6>. Citation on page 78.

PEKKARINEN, S.; ULKUNIEMI, P. Modularity in developing business services by platform approach. **The International Journal of Logistics Management**, Emerald Group Publishing Limited, 2008. DOI: <http://dx.doi.org/10.1108/09574090810872613>. Citation on page 48.

PIROGLU, F.; OZAKGUL, K. Partial collapses experienced for a steel space truss roof structure induced by ice ponds. **Engineering Failure Analysis**, Elsevier, v. 60, p. 155–165, 2016. DOI: <https://doi.org/10.1016/j.engfailanal.2015.11.039>. Citation on page 143.

RINKU, A.; ANANTHASURESH, G. Topology and size optimization of modular ribs in aircraft wings. **11th World Congr. Struct. Multidiscip. Optim**, p. 1–6, 2015. Citation on page 45.

RODDEN, W.; GIESING, J.; KALMAN, T. Refinement of the nonplanar aspects of the subsonic doublet-lattice lifting surface method. **Journal of Aircraft**, v. 9, n. 1, p. 69–73, 1972. DOI: <https://doi.org/10.2514/3.44322>. Citation on page 67.

RODDEN, W.; TAYLOR, P.; MCINTOSH, S. Further refinement of the nonplanar aspects of the subsonic doublet-lattice lifting surface method. In: **ICAS PROCEEDINGS**. [S.l.: s.n.], 1996. v. 20, p. 1786–1799. DOI: <https://doi.org/10.2514/3.44322>. Citations on pages 17, 72, and 73.

RODDEN, W. P.; JOHNSON, E. H. **MSC/NASTRAN aeroelastic analysis: user's guide; Version 68**. [S.l.]: MacNeal-Schwendler Corporation, 1994. Citation on page 121.

RODDEN, W. P.; TAYLOR, P. F.; JR, S. C. M. Further refinement of the subsonic doublet-lattice method. **Journal of aircraft**, v. 35, n. 5, p. 720–727, 1998. DOI: <https://doi.org/10.2514/2.2382>. Citations on pages 64, 66, 67, and 69.

RODDEN, W. P.; TAYLOR, P. F.; JR, S. C. M.; BAKER, M. L. Further convergence studies of the enhanced doublet-lattice method. **Journal of aircraft**, v. 36, n. 4, p. 682–688, 1999. DOI: <https://doi.org/10.2514/2.2511>. Citation on page 69.

ROESSLER, C.; BARTASEVICIUS, J.; KOEBERLE, S. J.; TEUBL, D.; HORNUNG, M.; MEDDAIKAR, Y. M.; DILLINGER, J. K.; WUSTENHAGEN, M.; KIER, T. M.; LOOYE, G. *et al.* Results of an aeroelastically tailored wing on the flexop demonstrator aircraft. In: **AIAA Scitech 2020 Forum**. [S.l.: s.n.], 2020. p. 1969. DOI: <https://doi.org/10.2514/6.2020-1969>. Citation on page 144.

ROESSLER, C.; STAHL, P.; SENDNER, F.; HERMANUTZ, A.; KOEBERLE, S.; BARTASEVICIUS, J.; ROZOV, V.; BREITSAMTER, C.; HORNUNG, M.; MEDDAIKAR, Y. M. *et al.* Aircraft design and testing of flexop unmanned flying demonstrator to test load alleviation and flutter suppression of high aspect ratio flexible wings. In: **AIAA scitech 2019 forum**. [S.l.: s.n.], 2019. p. 1813. DOI: <https://doi.org/10.2514/6.2019-1813>. Citation on page 144.

RÖSSLE, A. On the derivation of an asymptotically correct shear correction factor for the reissner-mindlin plate model. **Comptes Rendus de l'Académie des Sciences-Series I-Mathematics**, Elsevier, v. 328, n. 3, p. 269–274, 1999. DOI: <https://doi.org/10.1016/S0764-4442(99)80133-5>. Citation on page 94.

RYLEY, T.; BAUMEISTER, S.; COULTER, L. Climate change influences on aviation: A literature review. **Transport Policy**, Elsevier, v. 92, p. 55–64, 2020. DOI: <https://doi.org/10.1016/j.tranpol.2020.04.010>. Citation on page 36.

SAKAMOTO, M. M. Implementação de um gerador tridimensional de malhas de elementos finitos, com aplicações à simulação computacional em odontologia. Universidade Estadual Paulista (Unesp), 2001. Citation on page 135.

SALEEM, W.; YUQING, F.; YUNQIAO, W. Application of topology optimization and manufacturing simulations-a new trend in design of aircraft components. In: CITESEER. **Proceedings of the International MultiConference of Engineers and Computer Scientists**. [S.l.], 2008. v. 2. Citation on page 30.

SCHILLING, M. A.; STEENSMA, H. K. The use of modular organizational forms: An industry-level analysis. **Academy of management journal**, Academy of Management Briarcliff Manor, NY 10510, v. 44, n. 6, p. 1149–1168, 2001. DOI: <https://doi.org/10.2307/3069394>. Citation on page 47.

SHEWCHUK, J. R. **Delaunay refinement mesh generation**. [S.l.]: Carnegie Mellon University, 1997. Citation on page 137.

SIEMENS, A. aerobatic airplane "extra 330le". **With world-record electric motor from Siemens. Press release**, 2016. Citation on page 29.

SILVA, H. L.; GUIMARÃES, T. A. Conceptual design of a thin-haul aircraft by energy sizing optimization including aero-propulsive interactions. In: **AIAA Scitech 2020 Forum**. [S.l.: s.n.], 2020. p. 1503. DOI: <https://doi.org/10.2514/6.2020-1503>. Citation on page 30.

SILVA, H. L.; RESENDE, G. J.; NETO, R.; CARVALHO, A. R.; GIL, A. A.; CRUZ, M. A.; GUIMARÃES, T. A. A multidisciplinary design optimization for conceptual design of hybrid-electric aircraft. **Structural and Multidisciplinary Optimization**, Springer, p. 1–22, 2021. DOI: <https://doi.org/10.1007/s00158-021-03033-8>. Citation on page 30.

SILVA, R. G. A. da. **Análise aeroelástica no espaço de estados aplicada a aeronaves de asa fixa**. 196 p. Master's Thesis (Master's Thesis) — Universidade de São Paulo, São Carlos, 1994. Citation on page 117.

SILVA, W. V.; SILVA, R.; BEZERRA, L. M.; FREITAS, C. A.; BONILLA, J. Experimental analysis of space trusses using spacers of concrete with steel fiber and sisal fiber. **Materials**, Multidisciplinary Digital Publishing Institute, v. 13, n. 10, p. 2305, 2020. DOI: <10.3390/ma13102305>. Citation on page 141.

SLEESONGSOM, S.; BUREERAT, S.; TAI, K. Aircraft morphing wing design by using partial topology optimization. **Structural and Multidisciplinary Optimization**, Springer, v. 48, n. 6, p. 1109–1128, 2013. DOI: <https://doi.org/10.1007/s00158-013-0944-3>. Citation on page 30.

SODJA, J.; WERTER, N.; De Breuker, R. Design of a flying demonstrator wing for manoeuvre load alleviation with cruise shape constraint. In: **2018 AIAA/ASCE/AHS/ASC Structures, Structural Dynamics, and Materials Conference**. Reston, Virginia: American Institute of Aeronautics and Astronautics, 2018. ISBN 978-1-62410-532-6. DOI: <https://doi.org/10.2514/6.2018-2153>. Available: <https://arc.aiaa.org/doi/10.2514/6.2018-2153>. Citations on pages 144, 145, and 146.

SOUZA, A. S. C. d. **Análise teórica e experimental de treliças espaciais**. Phd Thesis (PhD Thesis) — Universidade de São Paulo, 2003. DOI: <10.11606/T.18.2003.tde-11102003-164954>. Citation on page 143.

STANFORD, B.; BERAN, P. Optimal structural topology of a platelike wing for subsonic aeroelastic stability. **Journal of Aircraft**, v. 48, n. 4, p. 1193–1203, 2011. DOI: <https://doi.org/10.2514/1.C031185>. Citation on page 43.

STANFORD, B.; IFJU, P. Aeroelastic topology optimization of membrane structures for micro air vehicles. **Structural and Multidisciplinary Optimization**, Springer, v. 38, n. 3, p. 301–316, 2009. DOI: <https://doi.org/10.1007/s00158-008-0292-x>. Citation on page 43.

STANFORD, B. K.; DUNNING, P. D. Optimal topology of aircraft rib and spar structures under aeroelastic loads. **Journal of Aircraft**, American Institute of Aeronautics and Astronautics, v. 52, n. 4, p. 1298–1311, 2015. DOI: <https://doi.org/10.2514/1.C032913>. Citation on page 44.

SÜELÖZGEN, Ö.; WÜSTENHAGEN, M. Operational Modal Analysis for Simulated Flight Flutter Test of an Unconventional Aircraft. In: **International Forum on Aeroelasticity and Structural Dynamics**. [S.l.: s.n.], 2019. Citations on pages 144 and 145.

SVIK, P. **Civil aviation and the globalization of the cold war**. [S.l.]: Springer, 2020. DOI: <https://doi.org/10.1007/978-3-030-51603-1>. Citation on page 35.

TAKARICS, B.; PATARTICS, B.; LUSPAY, T.; VANEK, B.; ROESSLER, C.; BARTASEVICIUS, J.; KOEBERLE, S. J.; HORNUNG, M.; TEUBL, D.; PUSCH, M. *et al.* Active flutter mitigation testing on the flexop demonstrator aircraft. In: **AIAA Scitech 2020 Forum**. [S.l.: s.n.], 2020. p. 1970. DOI: <https://doi.org/10.2514/6.2020-1970>. Citation on page 144.

TARIQ, M.; MASWOOD, A. I.; GAJANAYAKE, C. J.; GUPTA, A. K. Aircraft batteries: current trend towards more electric aircraft. **IET Electrical Systems in Transportation**, IET, v. 7, n. 2, p. 93–103, 2016. DOI: <https://doi.org/10.1049/iet-est.2016.0019>. Citation on page 30.

TEMAM, R. **Navier-Stokes equations: theory and numerical analysis**. [S.l.]: American Mathematical Soc., 2001. DOI: <https://doi.org/10.1090/chel/343>. Citation on page 52.

TRAINELLI, L.; COMINCINI, D.; SALUCCI, F.; ROLANDO, A.; RIBOLDI, C. Sizing and performance of hydrogen-driven airplanes. In: **Proc. XXV AIDAA Congress, Roma, Italy**. [S.l.: s.n.], 2019. Citation on page 30.

ULRICH, K. Fundamentals of product modularity. In: **Management of Design**. [S.l.]: Springer, 1994. p. 219–231. Citation on page 47.

VALENTE, C.; WALES, C.; JONES, D.; GAITONDE, A.; COOPER, J.; LEMMENS, Y. An optimized doublet-lattice method correction approach for a large civil aircraft. In: **17th International Forum on Aeroelasticity and Structural Dynamics**. [S.l.: s.n.], 2017. Citation on page 71.

VAN, D. W. L.; HAGDORN, L.; HOOGEWEEGEN, M. R.; VERVEST, P. H. Embedded coordination in a business network. **Journal of Information Technology**, SAGE Publications Sage UK: London, England, v. 19, n. 4, p. 261–269, 2004. DOI: <https://doi.org/10.1007/3-540-26694-1_18>. Citation on page 48.

VASSBERG, J.; DEHAAN, M.; RIVERS, M.; WAHLS, R. Development of a common research model for applied cfd validation studies. In: **26th AIAA applied aerodynamics conference**. [S.l.: s.n.], 2008. p. 6919. DOI: <https://doi.org/10.2514/6.2008-6919>. Citation on page 44.

VELICKI, A.; JEGLEY, D. Prseus development for the hybrid wing body aircraft. In: **AIAA Centennial of Naval Aviation Forum" 100 Years of Achievement and Progress"**. [S.l.: s.n.], 2011. p. 7025. DOI: <https://doi.org/10.2514/6.2011-7025>. Citation on page 29.

VIVIAN, H.; ANDREW, L. **Unsteady aerodynamics for advanced configurations. part i. application of the subsonic kernel function to nonplanar lifting surfaces**. [S.l.], 1965. Citations on pages 61, 62, and 66.

WANG, Q.; LU, Z.; ZHOU, C. New topology optimization method for wing leading-edge ribs. **Journal of aircraft**, v. 48, n. 5, p. 1741–1748, 2011. DOI: <https://doi.org/10.2514/1.C031362>. Citation on page 43.

WHEELER, P.; BOZHKO, S. The more electric aircraft: Technology and challenges. **IEEE Electrification Magazine**, v. 2, n. 4, p. 6–12, 2014. DOI: <http://dx.doi.org/10.1109/MELE.2014.2360720>. Citation on page 29.

WORKU, E. Analysis and design of struts to node connection of space truss in buildings. 2007. URI: <http://etd.aau.edu.et/handle/123456789/988>. Citation on page 140.

WRIGHT, J. R.; COOPER, J. E. **Introduction to aircraft aeroelasticity and loads**. [S.l.]: John Wiley & Sons, 2014. URI: <10.1002/9781118700440>. Citations on pages 119 and 120.

ZHANG, J.-k.; LI, Z.-n.; KOU, C.-h. Structural design of high aspect ratio composite material wing (p). **ACTA AERONAUTICA ET ASTRONAUTICA SINICA-SERIES A AND B-**, ACTA AERONAUTICA ET ASTRONAUTICA SINICA, v. 26, n. 4, p. 450, 2005. URL: <https://hkxb.buaa.edu.cn/EN/Y2005/V26/I4/450>. Citation on page 30.